INFORMATION TO USERS

This manuscript has been reproduced from the microfilm master. UMI films the text directly from the original or copy submitted. Thus, some thesis and dissertation copies are in typewriter face, while others may be from any type of computer printer.

The quality of this reproduction is dependent upon the quality of the copy submitted. Broken or indistinct print, colored or poor quality illustrations and photographs, print bleedthrough, substandard margins, and improper alignment can adversely affect reproduction.

In the unlikely event that the author did not send UMI a complete manuscript and there are missing pages, these will be noted. Also, if unauthorized copyright material had to be removed, a note will indicate the deletion.

Oversize materials (e.g., maps, drawings, charts) are reproduced by sectioning the original, beginning at the upper left-hand corner and continuing from left to right in equal sections with small overlaps. Each original is also photographed in one exposure and is included in reduced form at the back of the book.

Photographs included in the original manuscript have been reproduced xerographically in this copy. Higher quality 6" x 9" black and white photographic prints are available for any photographs or illustrations appearing in this copy for an additional charge. Contact UMI directly to order.

UMI®

Bell & Howell Information and Learning
300 North Zeeb Road, Ann Arbor, MI 48106-1346 USA
800-521-0600

The Effects of Dynamic Optical Properties During Interstitial Laser Photocoagulation

by

Megumi N. Iizuka

A thesis submitted in conformity with the requirements
for the degree of Master of Science
Graduate department of Medical Biophysics
The University of Toronto

Acknowledgments

I am very grateful for the tremendous guidance and support of my supervisors, Mike Sherar and Alex Vitkin. I cannot express fully my deep gratitude for their patience and encouragement throughout my degree. I also would like to thank Michael Kolios, for being my "student supervisor" and scientific mentor. His enthusiasm for physics and life, in general, is contagious and will be missed greatly in my daily life.

I would like to thank my committee member, Brian Wilson, and honourary member, Lothar Lilge for their kind and thorough scientific discussions and for suggesting many solutions to the technical problems I have faced over the years. I would also like to acknowledge Martin Shim, Ralph Dacosta, and Kai Zhang for giving me helpful assistance in the area of tissue optics on numerous occasions.

A big thank you also goes out to the members of the hyperthermia group, Carl Kumaradas, Mark Gertner, Wu Xia, Arthur Worthington, John Hunt, and Aviv Gladman who pretty much solved all the other technical and life problems that I ever ran into. I am especially grateful to Carl who has had to tolerate my ceaseless computer questions and terrible volleyball setting skills. I also can't forget the fun filled times with the students that I have had the pleasure to work with like Sarah Hammond and Matthew Skinner.

An emotional expression of gratitude goes out to my family members, Nana, Brian, Izu, Tom, Ayu, Matthew, Kuro, Mum and Dad for their unconditional support, strong encouragement, yummy meals and lively distractions throughout my entire academic career. Also, thanks to all my irreplaceable friends for life who have given me much inspiration: Rhona, Steve, Greg, Deepa, Paul, Rina, Natalie, Julien, Vern, the Jones, the Arvanitis as well as the regular Don Mills clan. A special thanks goes to soul mate, Maria Fathallah, my true and dear friend, for taking such good care of me during the production of this thesis and, in general, making this busy year so much more enjoyable and meaningful. Finally, I would like to deeply thank James Chin, for his invaluable input and direct effort in completing this thesis and for his unwaivering and loving support along the way.

The Effects of Dynamic Optical Properties During Interstitial Laser Photocoagulation

Megumi N. Iizuka. B.A.Sc.
Department of Medical Biophysics
The University of Toronto. 1998

Lasers can be used to heat and destroy cancer cells by delivering light via fiber directly into a tumour. in a novel and promising procedure called Interstitial Laser Photocoagulation (ILP). Thermal lesion formation during ILP is a dynamic process involving many heat induced alterations of tissue such as changes in optical properties and blood perfusion. However. the effects of these changes on the outcome of lesion formation are not well understood. Therefore. thermal models are being developed to investigate the importance of the effects on predicting treatment outcomes. These models are essential for the successful planning of thermal therapy treatments of ILP to achieve complete tumour destruction while sparing normal tissue and avoiding the deleterious effects of vapourization and charring.

The aim of our work is to propose and validate a model which incorporates heat induced changes of optical properties due to coagulation by solving the nonlinear bioheat equation. The dynamic effects are modeled based on the Arrhenius damage formulation which describes thermal damage as an irreversible rate process. The validity of the model assumptions was investigated experimentally by developing novel opto-thermal phantoms with properties similar to those of tissue. An albumen based phantom was used to represent the case when optical properties change with heat. Polyacrylamide phantoms. designed with static optical properties. were used to illustrate the difference in temperature rise when dynamic optical properties are not taken into account. The influence of these changing optical properties on fluence. temperature and damage predictions were then examined theoretically for the case of ILP of the liver.

Temperatures measured during ILP in the two phantoms agreed well with theoretical predictions. The experimental results confirmed both the conventional static model and the Arrhenius damage formulation used to describe the dynamic coagulation process. The

model demonstrated that changes in optical properties, namely an increase in scattering due to heat, causes a sharper temperature gradient and increases the peak temperature close to the optical source. Consequently, a sudden increase in the rate of temperature rise occurs, at the onset of coagulation which was confirmed experimentally in the albumen phantom. Hence, vapourization begins earlier in time than predicted by conventional static models which is an important consideration in order to avoid charring of the fiber tip.

The thermal lesion is both smaller and requires less optical power to produce than that predicted assuming native optical properties when the peak temperature is limited at the end of the therapy for the two cases. However, the size of the lesion is approximately the same as that predicted by the static case with coagulated optical properties. This suggests that the simpler static model with coagulated optical properties, can be used instead of the nonlinear model to predict final damage outcome. However, the laser power requirements, as well as the thermal histories, are considerably different between the static and nonlinear models.

In general, the temperature, fluence and damage profiles are highly dynamic during lesion formation due to the coagulation process. This establishes the need for theoretical models to account for changing optical properties during ILP. Furthermore, the Arrhenius damage formulation can be used to quantify accurately the effects of dynamic changes in optical properties in these models.

Contents

List of Figures

Nomenclature

A Frequency factor $[s^{-1}]$

c Heat capacity of tissue $[J \cdot g^{-1} \cdot {}^{\circ}C^{-1}]$

c_b Volumetric heat capacity of blood $[J \cdot g^{-1} \cdot {}^{\circ}C^{-1}]$

D Optical diffusion coefficient $[cm]$

E Activation energy $[J \cdot mol^{-1}]$

E_1 Exponential integral of the first order

F_o Fourier number

g Anisotropy factor

i Discretized spatial index

j Discretized temporal index

k Thermal conductivity of tissue $[W \cdot cm^{-1} \cdot {}^{\circ}C^{-1}]$

L Energy radiance $[J \cdot sr^{-1} \cdot s^{-1} \cdot cm^{-2}]$

L_{opt} Optical diffusion length $[cm]$

OD Optical density

P Deposited Power $[W \cdot cm^{-3}]$

P_o Optical power $[W]$

r Radial distance $[cm]$

r_o Radial distance of coagulation front $[cm]$

R Universal gas constant $[J \cdot mole^{-1} \cdot K^{-1}]$

s Light source term $[W \cdot cm^3]$

t Time $[s]$

T Temperature [°C]

T_{art} Temperature of arterial blood [°C]

T_r Transmittance of tissue

α, β Exponential integral parameters $[cm^{-1}]$

μ_a Absorption coefficient $[cm^{-1}]$

μ_e Effective attenuation coefficient $[cm^{-1}]$

μ_s Scattering coefficient $[cm^{-1}]$

μ_s' Reduced scattering coefficient $[cm^{-1}]$

μ_{tr} Total transport coefficient $[cm^{-1}]$

$\vec{\Omega}$ Solid angle $[sr]$

Ω Arrhenius Damage index for cell death

Ω_{opt} Arrhenius Damage index for changing optical properties

ϕ Fluence rate $[W \cdot cm^{-2}]$

ϕ_c Collimated fluence rate $[W \cdot cm^{-2}]$

ϕ_d Diffuse fluence rate $[W \cdot cm^{-2}]$

ρ Density of tissue $[g \cdot cm^{-3}]$

Chapter 1

Introduction

1.1 Interstitial Laser Photocoagulation

Heat, as a therapeutic agent for the treatment of cancer, has a long and varied history ranging in both method of heating and intensity [31]. In 400 B.C. Hippocrates introduced red-hot irons to treat small non-ulcerating cancers. In more modern times, W.C. Coley used milder temperatures by administering bacterial toxins to induce fevers in cancer patients in the late 1800s. Shortly thereafter, in 1909, W.E. Schmidt was the first researcher to investigate the use of heat as an adjuvent to radiation therapy. Since then, heat largely continues to be used in combination with other cytotoxic modalities such as radiation, and chemotherapeutic agents, giving rise to what will be referred to as *traditional hyperthermia*.

The heating regimes of traditional hyperthermia consist of relatively mild temperatures (41°C to 45°C) for long times (minutes to hours) [31]. More recently, the use of high temperatures for short exposures has been proposed [10]. This approach, also known as *high temperature thermal therapy*, aims to achieve rapid cell death by coagulating target tissues at temperatures above 50°C and is used as a stand-alone procedure. There are many sources of heat delivery in tissue, such as microwave antennas, ultrasound transducers and lasers. Investigations into the use of light as a therapeutic thermal agent began soon after the first ruby laser was invented in 1960. Since then, laser light has been used widely as a strong light source that can produce intense local heating [23].

The use of an optic fiber to deliver high intensity light percutaneously into tissue was first demonstrated in the early 1980s [13] in a procedure which is now commonly called interstitial laser photocoagulation (ILP). This is a minimally invasive technique which heats tumours directly by the delivery of optical power via thin flexible optical

fibers. The fibers are positioned through hollow needles which are inserted percutaneously under image guidance into the tumour. This method has the potential to treat deep-seated tumours without damaging overlying healthy tissue. Near infrared (NIR) wavelengths of laser light are used as a light source. The biophysical effects of light energy absorption are wavelength dependent. NIR wavelengths induce photothermal effects and permit deepest penetration into tissue relative to other wavelength ranges. The conventional wavelength is 1064 nm produced by the Nd:YAG laser. However, recently, high powered compact laser diodes (LD) at ~805 nm and ~980 nm wavelengths are being investigated. Typical thermal therapies of ILP last from 5 to 45 minutes using 2 to 10 watts of laser power. This produces a thermal lesion with various zones of destruction. These zones, listed from the hot centre to the cooler periphery, may include: a) an ablative crater, b) a layer of charred tissue, c) a coagulated zone, d) a band of hemostasis, hemorrhage and hyperemia and e) an outer boundary of grossly normal appearing tissue [76,108]. Several weeks after treatment the dead tissue is re-absorbed by normal healing mechanisms [14]. The healing mechanisms include the formation of scar tissue and the proliferation of new blood vessels and fibroblasts [105]. In addition to *in-vitro* and *in-vivo* animal studies, much of the knowledge of ILP has emerged from clinical trials. The clinical work has been essential in determining the efficacy of ILP for the actual treatment of cancer. Furthermore, the clinical experiences have played a role in the development of the methods and techniques of ILP to make it a viable treatment option. Thus, the next section describes the current status of the clinical experiences as well as future prospects and developments of ILP.

1.1.1 Clinical Experience

In addition to cancer, ILP has been studied in the treatment of other pathologies, such as benign prostate hyperplasia [54], congenital vascular disorders [78] and benign brain tumours [6]. For the treatment of cancer, ILP has been used most frequently in the brain [65,86] and liver [15,85]. It has also been used to treat tumours of the breast [39,41], head and neck [30,50,111], and prostate [2,70]. The potential niche of ILP differs for each tumour site and depends upon the tumour characteristics (metastasis versus primary, size, number and accessibility), prognosis (treatability with conventional methods), and desired treatment outcome (curative versus palliative). Thus far, however, ILP has been generally used to treat patients whose tumours are unresectable or who have failed conventional approaches such as radiation or chemotherapy. Most often, the cases present as metastatic disease, making ILP a palliative option only [15,30,86,112]. ILP may also be a potential

modality for the treatment of primary disease such as breast tumours [14,39]. Therefore, the need to ensure complete tumour destruction with ILP becomes paramount.

Complete destruction of tumours can be achieved only if the coagulated volumes are sufficiently large. This is the main limitation of ILP: the lesions are fairly small, ranging from 1 to 3 cm in diameter. The size of the lesion can be increased by using higher laser powers [82]. However, this causes the peak temperature to rise potentially to vapourization temperatures (boiling point) which leads to carbonization (charring) of the tissue and fiber tip [130]. Carbonization is caused by a rapid absorption of the light due to a significant decrease in the optical penetration. This in turn produces higher local temperatures and thus more charring [130].

The issue of carbonization is controversial. Carbonization of the fiber tip causes it to act like a point heat source which allows more predictable and slightly larger damage volumes to be achieved than without charring [41,130]. Furthermore, a plane-cut fiber tip can be used, making ILP with charring a simple and cheap method of interstitial delivery of heat [36,41]. However, after carbonization occurs, light can no longer be deposited into tissue. Therefore, charring prevents the use of laser parameters, such as laser power and wavelength, to control the extent of heating. In general, charring would obviate any advantages of laser irradiation since the mechanism of heating no longer involves the laser light directly. Therefore, there is motivation to maximize the size of coagulation without inducing vapourization or carbonization. Approaches include a) the insertion of multiple fibers [46,107,126] b) the use of diffusing fiber tips [42,90] or c) the design of specialized water or air cooled fiber tip applicators [74,90]. The initial results appear promising and demonstrate that large lesions can be achieved in a controlled manner, without vapourization or charring.

Medical imaging has been critical in assessing the laser-induced extent of damage. Numerous clinical trials have employed imaging modalities such as CT, MRI and ultrasound to monitor the effects of ILP. In general, the treatment volume is seen most clearly on MRI and CT scans. Ultrasound has been used mainly for the placement of interstitial probes [41,109]. CT or MRI scans are usually taken prior to, immediately after, and/or several days to weeks post thermal therapy. Evidence of thermal damage is seen on MRI [39,55] and CT images [3,36] as a central zone of destruction due to a difference in tissue integrity between healthy and treated areas. The effects of ILP are enhanced with the use of contrast agents for both MRI [55,71] and CT [3,36,83]. Currently, there are efforts to correlate the imaging parameters with the actual boundaries of lethal thermal injury [68,93].

Recent advances in MRI imaging have included real-time 3D mapping of temperature profiles and tissue integrity during thermal therapy [53]. These developments allow one to visualize the formation of the thermal lesion as it occurs. Therefore, the treatment parameters may be modified dynamically according to the relevant changing markers (such as temperature or tissue damage) to ensure complete tumour destruction without vaporization while sparing healthy tissues. In this manner, imaging can be used to provide the necessary feedback information for the automated control of the laser power [46, 74].

The initial clinical experiences of ILP are promising. Many benefits of ILP have been demonstrated, including reduced hospitalization, reduced morbidity, faster recovery and ease of procedural technique [14, 15, 36, 65, 86]. Furthermore, imaging techniques allow for the accurate placement of probes and assessment of laser-induced damage during and after ILP. The future prospects of monitoring and dynamically changing the treatment parameters during the procedure are exciting, with the possibility that ILP will become a viable and minimally invasive treatment option for the palliation or cure of cancers in selected sites.

1.1.2 Theoretical Models

The clinical research has demonstrated clearly the ability of ILP in destroying tissue. Alongside this research, investigators have also sought to understand the mechanism of lesion formation from a biophysical point of view. These studies have examined the effects of laser power [82, 129], wavelength [69], heating time [129] and method of fiber delivery [90]. In an effort to understand these cumulative effects, theoretical models have been used to describe the opto-thermal response of tissue [114]. These models provide a theoretical framework which can be used to substantiate, evaluate and interpret experimental results. As well, the models can be used to predict *a priori* the outcome of proposed experiments or treatments. For example, models can be used to quantify the effects of laser parameters and tissue structure on thermal lesion formation. This information will be essential for the successful planning of treatments. In addition, simulations may play a crucial role in feedback systems by providing on-line adjustments to treatment parameters during the procedure [46]. As a result, modeling of thermal therapy with lasers has been investigated widely (for a review see McKenzie [63]). The next section includes a description of the development of the basic components of opto-thermal models. This information will provide the background of the main topic of this thesis which is to develop a theoretical model which examines the effects of dynamic changes in optical properties during ILP.

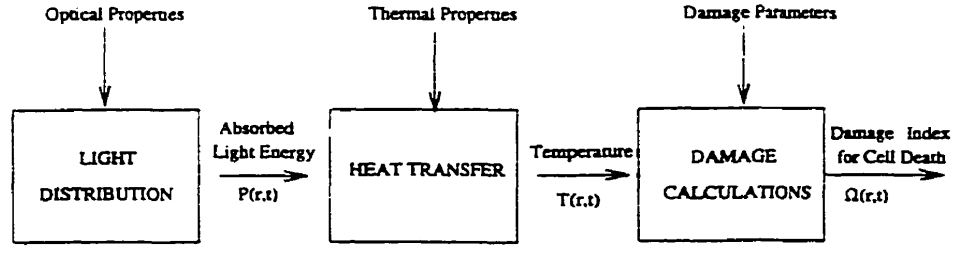

Figure 1.1: Block diagram of basic model to calculate thermal damage due to laser irradiation. The inputs along the top of the diagram indicate the experimentally measured properties.

The basic opto-thermal model consists of three steps: calculation of the 1) light distribution derived from theories of light propagation in tissue. 2) temperature rise based on heat transfer and 3) extent of thermal damage (cell kill) formulated from rate process kinetics. Each stage of modeling requires information from the previous stage and from determined values of tissue properties (Refer to figure 1.1 which was adapted from Welch [114]). The following sections provide the theoretical and experimental basis of each stage in greater detail.

I) Light Distribution Theory

Thermal damage begins with the deposition of light energy into tissue. The distribution of the light energy depends upon the interaction of light with tissue components. In general, light may either be absorbed or scattered in a manner that is wavelength dependent. Most of the light energy that is absorbed is transferred into vibrational energy. The vibrational energy results in an increase in temperature at the site of absorption called the chromophore. There are several natural chromophores in tissue which, when weighted by their respective concentrations, sum up to produce an overall absorption. Some common chromophores include water, melanin, hemoglobin, myoglobin and bilirubin. Elastic scattering of light in tissue describes the energy preserving deviation of light from its straight path course. The directional deviations may be due to microscopic discontinuities of the refractive index at the cellular level. Examples of possible discontinuities occur at the aqueous-lipid membrane interfaces surrounding and within each cell, and the collagen fibrils within the extra-cellular matrix [51].

Theoretical models have been proposed to describe the influence of absorption and scattering events in tissue. Most models are derived from radiative transport theory which describes heuristically the flow of energy in a medium of neutral particles to formulate

what is known as the radiative transport equation or the Boltzmann equation [26]. This equation calculates the steady state net energy balance transported by photons over a certain solid angle, $\vec{\Omega}$, giving rise to the quantity called energy radiance $L(\vec{\Omega})$. The net energy balance accounts for a) the loss of photons due to absorption and scattering events and b) the gain of photons due to scattering from neighbouring events and due to the light source itself at a point in space. Unfortunately, there are a limited number of analytical solutions to the radiative transport equation. As a result, many approximations to the radiative transport equation have been proposed for tissue, some of which are reviewed by Patterson *et al* [75].

One of the most widely used approximations of the radiative transport equation is the *diffusion approximation*. This approximation is based upon the assumption that scattering events dominate over absorption events in tissue. It is derived from the radiative transport equation by expanding the angular dependence of the radiance $L(\vec{\Omega})$, in spherical harmonics and keeping only the first two terms of the expansion [44]. This results in a second order differential equation of the fluence rate or light fluence ϕ which is equal to the energy radiance summed over all angles. The light diffusion approximation is expressed as:

$$-D\nabla^2\phi(r) + \mu_a\phi(r) = s(r) \tag{1.1}$$

which estimates the light distribution in tissue due to the light source, $s(r)$. The optical properties of tissue are embedded in the diffusion coefficient, D, which is equal to $[3(\mu_s' + \mu_a)]^{-1}$ where μ_s' and μ_a quantify the scattering and absorption events respectively. The mathematical rigor of this equation and the meaning of μ_a and μ_s' are discussed more fully in chapters 2 and 3.

The diffusion theory has been successful at predicting light fluence in tissue [72] and tissue equivalent materials [56]. A limitation of diffusion theory is that the accuracy close to the source and tissue boundaries [44, 90] or within highly absorbing regions [35, 44] is poor. Nonetheless, the theory is useful for the calculation of light distribution within bulk media for most tissue types. Thus, it has been used to study a large variety of applications such as photodynamic therapy (PDT) [38, 124], optical imaging [81] and the determination of optical properties [45, 123]. The diffusion approximation has also been implemented often in theoretical modeling of ILP [90, 125]. The calculated light distribution from the diffusion approximation acts as a the heat source for a second set of calculations which predicts the transport of heat in tissue.

Transport of Heat in Tissue

The transport of heat was proposed historically for laser irradiation using the basic heat conduction equation in solids [114]:

$$\rho c \frac{\partial T}{\partial t} = \nabla \cdot (k \nabla T) + P \tag{1.2}$$

where k is the thermal conductivity, c is the specific heat and ρ is the density of tissue. The energy source, represented by P, can be assumed from light propagation theory by multiplying the fluence, ϕ, by the absorption coefficient, μ_a [114]. This equation takes into account the diffusion of heat from the source and calculates the resultant spatial and temporal temperature rise, T, of bulk solids. Initially, heat transport theory in this form was used to describe rapid elevation of temperatures beyond the vapourization threshold due to short intense pulses of light [63]. The effects of blood perfusion were ignored due to the short heating times and since high temperatures were assumed to cause immediate damage of the vasculature [63]. Thermal coagulation, however, uses longer heating periods (on the order of minutes) and, therefore, this equation was replaced by a modified form of the basic conduction formulation called the bioheat transfer equation [77]:

$$\rho c \frac{\partial T}{\partial t} = \nabla \cdot (k \nabla T) + P - w_b c_b (T - T_{art}) \tag{1.3}$$

The bioheat transfer equation differs from basic heat conduction by the inclusion of the last term which describes the convective effects of blood flow as a function of the volumetric perfusion rate, w_b, the heat capacity of blood, c_b, and a temperature difference between local tissue and arterial temperature. Various other thermal models exist which also attempt to include the effects of blood perfusion [131]. However, the bioheat equation has been the most prevalent of models used in studies related to heat transfer in perfused tissues [17, 94]. Investigators have tested the validity of this model for a variety of tissues [18, 19, 59, 67, 77]. The results of these studies show that the bioheat equation accurately predicts temperature rise in organs supplied with microvascular blood flow.

Calculations of the temperature rise in tissue is an indirect method of determining the final outcome of the thermal treatment. Ultimately, we are interested in some biological consequence due to the effects of elevated temperature. For the case of thermal therapy with lasers, the desired outcome is cell death due to thermal denaturation of proteins. Experimental investigations have been conducted to determine the relationship between temperature and tissue damage [43]. These relationships can be used with the bioheat equation to estimate the final biological effect of heat on tissue.

Damage Predictions

Henriques first proposed that damage can be predicted according to temperature using a kinetic rate model based on the Arrhenius integral [43]. He studied the thermal damage of pig skin and postulated that the relationship between damage and temperature is of the form:

$$\Omega(r,\tau) = ln\left(\frac{C(r,0)}{C(r,\tau)}\right) = \int_0^\tau A \cdot e^{-\frac{E}{RT(r,t)}}\, dt \tag{1.4}$$

where

- Ω = damage index $[dimensionless]$
- A = frequency factor $[s^{-1}]$
- E = activation energy $[J \cdot mol^{-1}]$
- R = universal gas constant $[J \cdot mol^{-1} \cdot K^{-1}]$
- τ = total heating time $[s]$

The damage index, Ω, is a measure of the volume fraction of damaged cells[1]. Explicitly, Ω is the logarithm of the ratio of the initial concentration of undamaged tissue, $(C(r,0))$, to that after damage has occurred at time, τ, $(C(r,\tau))$ [76]. Therefore, $\Omega = 1$ corresponds to the condition where 63% of the cells have been killed.

Henriques tested this model by applying constant temperatures from 44°C to 54°C to the tissue for a sufficient length of time (τ) to produce a threshold of damage. The threshold of damage was chosen as complete cellular necrosis of the basal epidermis layer. An experimental plot of the data in the form of $ln(\tau)$ versus $1/T$ was a straight line fit for a damage index of $\Omega = 1$. From this plot, the damage coefficients of A and E could then be derived experimentally. This verified the validity of equation (1.4) and demonstrated that damage is dependent upon both temperature and duration of exposure to heat. For example, his results indicated that an exposure of 100 seconds at 51°C produced the same extent of damage as an exposure of 1000 seconds at 47.8°C. Since then, the survival response of mammalian cells to hyperthermic temperature ranges (42°C to 45°C) has been well established using Arrhenius analysis [8, 118]. Higher temperatures have been investigated more recently by Borrelli *et al* [11] who used the Arrhenius equation to determine the damage coefficients for the survival of baby hamster kidney (BHK) cells between the range of 43.5°C and 57°C. The measurement of Arrhenius coefficients at progressively higher temperatures would be difficult to perform since the heating times to

[1]Not to be confused with the vector $\vec{\Omega}$ used for solid angles

achieve the threshold damage become exponentially shorter. Nevertheless, the Arrhenius integral provides a theoretical relationship between temperature and damage that has been widely used in modeling of photocoagulation [37,57,90,115].

The previous sections describe the three basic stages of mathematical models of laser thermal therapy. Numerous investigators have developed models which include some or all three stages to examine the thermal effects due to intraluminal [5,100], broad beam [48,96, 99] or interstitial [21,24,121] laser irradiation. The pupose of many of these investigations is to present a theoretical model upon which to base treatment plans for certain pathologies such as prostate cancer [5]. The models also are used to examine the effects of laser irradiation parameters such as wavelength, duration and source geometry on fluence rate, thermal and damage predictions [5,48].

Attempts have been made to validate experimentally the theoretical results of opto-thermal models [48,96,99,120,121]. Splinter *et al* [96] attempted to correlate theoretical light distribution patterns with measured lesion dimension on canine hearts *in-vivo*. However, the data did not demonstrate a clear dependency of the lesion dimension on the laser energy delivered. Jacques *et al* [48] modeled the light fluence based upon measurements of optical properties and calculated the resultant temperature rise due to short pulses (1 to 10 seconds) of the skin of a mouse *in-vivo*. They observed shrinkage and whitening which marked the onset of coagulation between 60°C and 70°C. Both Jacques and Splinter noted that the visible changes of coagulation may indicate a change in optical properties which would alter the photon deposition and thus their theoretical predictions [48, 96]. This was not observed by Sturesson *et al* [99] who achieved good correlation between temperature measurements and theoretical predictions for bovine liver *in-vitro* . However, the temperature measurements were below 48°C and therefore below the protein coagulation threshold.

The experimental evidence suggests that the tissue optical properties change significantly during heating and that this may influence thermal calculations. Studies indicate that tissue undergoes an array of morphological changes due to heat which results in changes in absorption and scattering coefficients [47,51]. For example, heat has been shown to denature proteins and other biomolecules causing cell shrinkage, birefringence changes, membrane rupture and hyalinization of collagen [76]. The change in scattering coefficient μ_s' has been partially explained by heat induced aggregation of proteins [47,51] and conformational transitions of cellular structures such as mitochondria, muscle fibers, [22,51,106] endoplastic reticulum and golgi apparatus [51]. Furthermore, the scattering coefficient may change as a consequence of decreased size of the scattering particles to sub-micron

levels [51, 106]. It is postulated that the change in absorption coefficient μ_a is due to the modification of blood content in tissue [9]. Note, however, that there is a limited understanding of the quantitative relationship between cellular ultrastructure and the resultant optical properties.

The heat induced changes in optical properties depends upon the tissue type and heating times. In broad terms, coagulation causes a 2 to 6 fold increase in scattering coefficient [88, 125] and a slight increase or decrease in absorption coefficient [88]. The overall effect is that light penetration diminishes as tissue becomes coagulated mostly attributed to the increase in scattering properties. The rate at which changes in scattering properties occur, depends upon the temperature and time of exposuture. It has been shown that these changes are rate limited in a similar way as cell death, such that the relationship between μ_s' and temperature is of the form given by the Arrhenius damage relationship (equation 1.4) [64, 79, 132].

Other significant heat induced responses include changes in blood perfusion [16, 92] and thermal properties [25]. Initially, blood flow has been found to increase due to vasodilatation due to an inflammatory response to heat [87]. If the temperature is increased above approximately 42°C the blood flow decreases until complete stasis occurs [28,87,92]. The mechanism of this stasis is a combined result of many factors including changes in the endothelial cells of the vessel wall, leukocytic and erythrocytic aggregation, and fibrin formation [28]. Note that the bulk of blood perfusion measurements have been observed at traditional hyperthermic temperature ranges of below 45°C [87]. At present, blood flow measurements in the higher coagulated temperature ranges are still in their preliminary stages [61, 66].

Partial data on thermal properties of tissue appear quasi-constant at various temperatures below 100°C [25]. However, complete information on the temperature dependent behaviour of the thermal properties of tissue has not been reported. The dynamic behaviour of tissue may be similar to the temperature dependent effects of water, which experiences a slight increase in heat capacity and conductivity and a small decrease in density [4]. Heat also dehydrates tissue reducing the content of water which may also influence the thermal properties of tissue.

In order to account for the effects of changing properties of tissue, investigators have proposed modifications to the basic linear model outlined above [9,57,84]. The modifications are such that the tissue properties are dependent on on-going calculations of temperature [9] and damage [84]. This inter-dependency results in dynamic input parameters of the bioheat equation resulting in a *nonlinear* solution. The block diagram of a

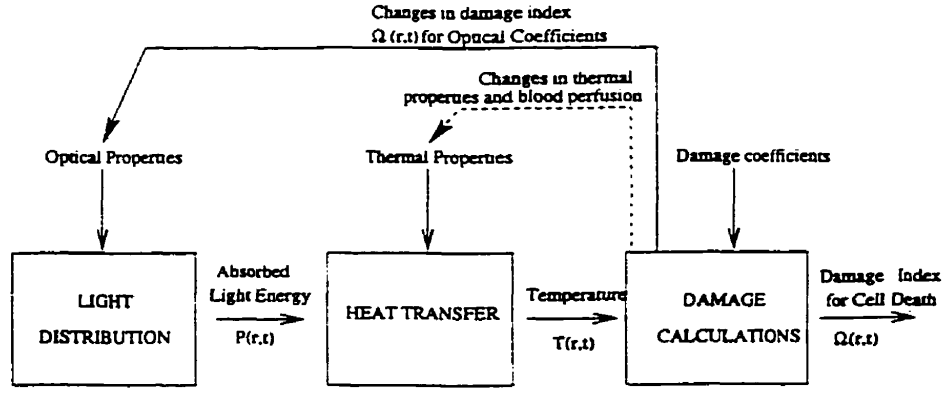

Figure 1.2: Block diagram of dynamic model to calculate thermal damage due to laser irradiation.

nonlinear model with changing properties is presented in figure 1.2. This figure is similar to the basic opto-thermal model shown in figure 1.1. However, a feedback path is also included which affects the property inputs, such as optical and thermal tissue characteristics, based on the Arrhenius damage formulation, $(\Omega(r,t))$. This then alters the light or temperature field calculations during the next time iteration of calculations. The process is repeated resulting in a dynamic time varying model.

Using this nonlinear method, the influence of changing optical properties on temperature rise has been modeled by Rastegar *et al* [84]. Their conclusions suggest that the effects of changing optical properties causes steeper temperature gradients and higher peak temperatures as a result of reduced penetration of light. The results were limited, however, to short irradiation times on the order of seconds. Kim *et al* [57] have examined the more complex case of modeling both changes in optical and blood perfusion properties with Arrhenius rate processes and concluded similar results as Rastegar *et al* for dynamic optical properties. Neither studies have confirmed the nonlinear assumptions of the Arrhenius formulation experimentally. Nor have they examined the case where the peak temperatures were maintained below the vapourization threshold. Therefore, the development and experimental verification of a nonlinear ILP model for treatments of several minutes while avoiding tissue vapourization temperature is necessary.

1.2 Phantoms

Thermal models can be experimentally tested in a media that reproduces the relevant properties and geometry of biological tissue. Using actual tissue may be impractical due

to the constraints of accessibility and storage of fresh samples. Reproducibility of results may also be poor because of the difficulty in finding identical specimens. Furthermore, *ex-vivo* tissue may require additional preparation such as homogenization [120, 128] which may change the properties of the tissue specimen themselves and do not necessarily have the same optical properties as living tissues due to, for example, the extent of oxygenated blood [117]. Nevertheless, some investigators have examined the possibility of using *ex-vivo* tissue as a phantom material for this purpose [103, 120, 128].

Another approach is to use tissue-equivalent materials or *phantoms*. Phantoms are usually homogeneous, and therefore do not normally possess the complex structures that exist throughout tissue such as vasculature and stroma. Therefore, tissue substitutes do not necessarily reflect the true response of tissue during laser therapy. However, they do provide a quantitative means of testing the parameters and assumptions made in thermal models.

The tissue simulating material should be designed to reproduce the relevant properties of tissue associated with the heating modality. The characteristics of interest associated with lasers include the optical and thermal properties. The choice of an appropriate phantom material is also dependent on the method of measurement. Therefore, the physical state of the phantom, *i.e.* liquid, solid or semi-solid (gel-like), affects the choice of measurement technique.

Many tissue-equivalent phantom materials have been proposed for use in optical applications such as spectroscopy and imaging [32–34, 58, 73, 91, 98, 113]. Unfortunately most of these phantoms are liquid, making them a poor choice for thermal dosimetry phantom studies due to convective effects of heated liquids. Others have used gels [73], polyacrylamide [60] and albumen [40] to observe the effects of laser ablation. The biophysical mechanisms of ablation, which induces vapourization with short laser pulses, and the methods of measuring these mechanisms, differ greatly from those of photothermal responses. As such, phantoms proposed for ablation may not be suitable for photocoagulation studies. For example, most of the materials have optical properties suited for the short ultraviolet range or are generally very dissimilar from tissue [40, 60, 73]. Unfortunately, however, there are very few phantoms in the literature that have been proposed for use in studies of photothermal responses.

Instead of *ex-vivo* tissue, albumen may be potentially used as a phantom. Albumen is a convenient material since it is readily available, has consistently the same properties, and is homogeneous and uniform in appearance. It also undergoes a visible whitening effect as a result of the thermal coagulation in a similar manner to tissue. This has been

examined in studies measuring its optical properties and denaturation process [64, 79]. Hence, albumen may be both a convenient and realistic material with well characterized opto-thermal properties that can be used to experimentally validate dynamic thermal models.

Dynamic experimental studies in albumen can also be compared to a phantom with static optical properties. This provides a means of illustrating the difference when heat-induced changes in optical properties are ignored. As such, phantoms with static properties provide a reference set of measurements. Polyacrylamide is a material which is resistant to change due to high temperatures [60]. This material has also been previously demonstrated to be a suitable muscle-equivalent phantom for hyperthermia with microwaves [102]. Therefore, this material may be proposed as a control medium whose optical properties do not change with temperature.

1.3 Purpose of Thesis

Lasers can be used to heat and destroy cancer cells by delivering light via fiber directly into a tumour, in a novel and promising procedure called Interstitial Laser Photocoagulation (ILP). Thermal lesion formation during ILP is a dynamic process involving many heat induced alterations of tissue such as changes in optical properties, thermal properties and blood perfusion. However, the effects of these changes on the outcome of lesion formation are not well understood. Experimental evidence shows that as tissue coagulates, the scattering coefficient significantly increases resulting in a reduced depth of light penetration. The rate of change of scattering follows an Arrhenius damage relationship which has been implemented in nonlinear opto-thermal models. The use of the Arrhenius relationship is a crucial mathematical link to describe the dynamic role between temperature rise and changes in light distribution. However, this nonlinear pathway has not been verified experimentally. As well, the effects of dynamic optical properties on fluence, temperature and damage predictions have not been examined fully for heating temperature and time ranges of ILP.

The purpose of this thesis is to investigate and validate experimentally the role of changing optical properties on fluence, temperature and damage predictions using a nonlinear model. We expect that changes in optical properties will result in a reduced light penetration leading to an increase in localized heating within the coagulated region. However, we would like to examine and confirm the temporal influence of this heat-induced response over time by using an Arrhenius damage relationship in the nonlinear opto-

thermal model. Validation of the model will be performed by developing tissue-equivalent phantoms. This will provide a means of observing photocoagulation in a well characterized and controlled medium.

1.4 Organization of Thesis

The thesis is organized into two sections: an experimental and a theoretical section. The first section, chapter 2, describes the development of phantoms for the study of photocoagulation. This chapter outlines the materials and methods used in the design and characterization of two proposed tissue-substitutes. The first phantom was designed with dynamic optical properties. Therefore, albumen (egg white) which visibly coagulates with heat, was chosen as the base constituent for a tissue-equivalent material. An additional phantom was developed whose optical properties do not change with temperature using polyacrylamide as a base phantom. An explanation of the characterization of these phantoms is included within the chapter.

Chapter 3 explains the development and predicted outcome of a nonlinear thermal model of ILP. The theoretical calculations of the model which predict light, temperature and damage profiles in tissue are discussed. This is followed by an explanation of the numerical methods that are used to compute the predicted results. Experimental validation of the model is performed using the phantoms described in chapter 2. Therefore, this chapter includes a description of the methods used to test the numerical predictions against measured results. This is followed by a brief theoretical investigation of the effects of changing optical properties in a clinical relevant case: ILP of the liver.

The final chapter (chapter 4), summarizes the results of the thesis. Furthermore, preliminary work on current areas of interest of ILP is presented. For example, dynamic effects of blood perfusion, fiber tip cooling and variable power with time are discussed. As well, the potential of measuring dynamic changes in fluence distribution as a means of monitoring the coagulation process is discussed.

Chapter 2

Optical Phantom Materials for Photocoagulation Studies

2.1 Abstract

The mechanisms of lesion formation during laser irradiation are not well known. In particular, the heat induced alteration of optical properties confounds the issue. Two tissue phantom systems were developed to investigate the effects of changing optical properties during interstitial laser photocoagulation. Albumen, which has temperature dependent optical properties, was used as a base material to simulate conditions of changing optical properties that occur in tissue. The albumen phantom was prepared using agar and an absorbing dye (Naphthol Green). The optical properties of the albumen phantom were measured using the poisoned moderator technique [123, 124]. A second phantom was developed with polyacrylamide. This base material was chosen due to its resistance to heat. Therefore, it represents a static case where no changes in optical properties occur during heating. Polyacrylamide mixtures were then constructed with optical properties that matched those of albumen in both its native and coagulated states by adding an absorbing dye, (Naphthol Green) and a scattering liquid, (Intralipid-10%).

The optical properties of the albumen phantom were successfully measured in both its native and coagulated states. The μ_a and μ_s' in the native state were 0.50 ± 0.04 cm^{-1} and 2.67 ± 0.07 cm^{-1} and in the coagulated state were 0.7 ± 0.1 cm^{-1} and 13.1 ± 0.5 cm^{-1} respectively. Polyacrylamide phantoms were constructed with the equivalent values of μ_a and μ_s' by adding Naphthol Green and Intralipid-10%. The optical properties of the phantoms are similar to those of tissue at near infrared wavelengths (NIR). As such

they may be used in future investigations which study the opto-thermal response of tissue during laser irradiation.

2.2 Introduction

The use of tissue-equivalent materials (phantoms) provides a means for investigating the propagation and absorption of light and subsequent temperature rise and denaturation in tissue. As such, they are valuable for confirming or testing mathematical models which predict the response of tissue during laser irradiation and in particular during ILP. Thus, we have developed and characterized two different opto-thermal phantoms. The phantoms were used to validate the theoretical models that examine the effects of changing optical properties discussed in chapter 3.

Egg white (albumen) has been studied and proposed as a potential material for use in studies of laser irradiation [40, 64, 79, 132]. It is a convenient material, since it is readily available, has consistently the same properties, and is homogeneous and uniform in appearance. Furthermore, it responds to heat in a similar manner to tissue in that it undergoes a visible thermal coagulation effect.

Albumen is mainly comprised of globular proteins (about 10.2%), lipids (0.05%) and water (88.1%) [79]. Exposure to heat causes an unfolding of the proteins which then precipitate out of solution and rapidly form aggregates [79]. Consequently, albumen visibly whitens during this process which is characterized by an increase in the scattering coefficient μ_s' [64, 79]. In its native state, albumen absorbs weakly and has a low scattering coefficient in the near infrared (NIR) relative to biological tissues [79]. To achieve optical properties that are more closely matched to tissue, we added an absorbing dye to increase absorption and a polysaccharide gel (agar or agarose) to increase the scattering. Naphthol Green is an effective absorber of short near infrared (NIR) wavelengths (700-850 nm). Agar also acts as a solidifying agent. This makes the phantom more structurally supportive and hence more similar to tissue. As well, it prevents the convective thermal effects of heated fluids.

The optical properties of this phantom were measured with the *poisoned moderator* or *added absorber* technique which is based upon diffusion theory [123, 124]. The procedure is applied in highly scattering tissue by adding increasing concentrations of dye of known absorption and measuring the penetration of light in these samples. The absorber can be uniformly added to the albumen solution. The poisoned moderator technique has been used previously to measure the optical properties of bovine liver, bovine muscle, pig brain,

and chicken muscle [124].

A second phantom was developed as a control whose optical and thermal properties do not change with temperature. This control phantom was used to demonstrate the difference in temperature predictions when heat-induced changes in optical properties are not accounted for. As such, phantoms with static properties provide a reference set of measurements. Polyacrylamide was used as the base material due to its high melting point [60]. This gel is commonly used in DNA sequencing and electrophoresis. The gel begins in liquid monomer form, but after the addition of a catalyst, it undergoes an exothermic polymerization reaction and solidifies, producing a pliable, yet structurally supportive rubber-like gel. This material has also been used as a good muscle-equivalent phantom for hyperthermia with microwaves [102].

As an optical phantom, polyacrylamide is suitable since it is transparent in the NIR. Hence, the water based solution of liquid acrylamide can be doped with absorbing dyes and scattering materials to obtain the desired optical properties. An ideal phantom uses a non-scattering absorbing medium and a non-absorbing scattering medium [91]. Naphthol Green was used as an NIR absorber since this organic powder is highly water soluble [95] and thus introduces minimal scattering in the polyacrylamide solution. An example of an effective scattering source in phantoms is Intralipid-10%. This is a white liquid emulsion of 10% solution of soybean oil in water. The soybean oil exists as phospholipid micelles in suspension which give Intralipid-10% its scattering properties [98]. This material has been previously studied and well characterized [34, 98]. These studies indicate that Intralipid-10% is weakly absorbing, and highly scattering which can be diluted to produce a scattering coefficient that is very similar to that of tissue in the NIR.

This chapter first introduces the basic description of light propagation in highly scattering tissue using diffusion theory. This leads to an explanation of the theoretical basis for the poisoned moderator technique. The recipe of the albumen phantom is provided followed by a description of the apparatus and techniques used for measuring the fluence rate within the native and coagulated samples of albumen. The recipe of the polyacrylamide phantoms and the method of matching the albumen optical properties in the polyacrylamide are then presented.

2.3 Theory

2.3.1 Light Propagation in Tissue

This section provides a brief introduction about the theoretical nature of light propagation in tissue or tissue-equivalent materials. This background information is the theoretical basis of the poison moderator technique for measuring optical properties in the albumen phantom. The theory is also applied to determine the required concentrations of scattering and absorbing materials for the polyacrylamide phantoms.

The propagation of light in highly scattering material is governed by its absorption and scattering characteristics. Absorption is the transfer of light photon energy into other forms of available energy. Most light that is absorbed is transferred into vibrational energy which results in an increase in temperature. This is quantified by the absorption coefficient, μ_a, which is defined as the probability that a light photon is absorbed per unit length of propagation. A medium with several constituents has an absorption coefficient equal to the sum of the individual coefficients of the constituents weighted by their concentrations.

Scattering of light in tissue describes the deviation of light from its straight path course. The deviation in direction is due to changes in refractive index at the boundary of scatterers, resulting in elastic scattering processes. This is quantified by the scattering coefficient, μ_s, which is defined as the probability of light scattered per unit length of propagation. The probability that light is scattered in a particular direction varies as a function of the angle of deviation, θ. The effect of the degree of anisotropy of this scattering process, can be quantified by taking the mean cosine of the scattering probability over all angles. This quantity is represented by the anisotropy factor, g. For example, total forward scattering means $g = 1$ and isotropic scattering means $g = 0$. The reduced linear scattering coefficient, $\mu_s' = \mu_s(1 - g)$ incorporates the effects of directionally dependent anisotropic scattering into a single term [127].

The scattering and absorption coefficients can be used to describe the intensity of light in tissue as a function of spatial position. This theory, described briefly as follows, is adapted from explanations of photon propagation in scattering media found in various texts [26, 97]. The light intensity is comprised of *collimated* and *diffuse* photon fluence or flux, which is equivalent to the net power of photons that pass through a point per area. The collimated fluence, ϕ_c, refers to the contribution of photons that are removed from its straight path course by encountering a single absorption or scattering event. In spherical

coordinates. the collimated fluence from a point source of light is proportional to

$$\phi_c(r) \propto \frac{exp(-(\mu_a + \mu_s)r)}{r^2} \tag{2.1}$$

Note that for a transparent material. such as polyacrylamide. which is doped only with absorbing material. equation (2.1) reduces to:

$$\phi(r) \propto \frac{exp(-\mu_a\ r)}{r^2} \tag{2.2}$$

This is equivalent to Beer's law of propagation of waves in a purely absorbing medium [117].

The diffuse photon flux refers to the contribution of photons that have been multiply scattered. The diffuse fluence is solved from the light diffusion approximation of equation (1.1) which is an approximation to the radiative transport theory. The underlying assumption of this approximation is that scattering dominates absorption as in the case of tissue in the NIR wavelength range. The *diffuse* photon fluence. ϕ_d, is equal to the net power of directionally independent photons that pass through a point per area such that:

$$\phi_d(r) \propto \frac{exp(-\mu_{eff} \cdot r)}{r} \tag{2.3}$$

where the μ_{eff} is called the effective attenuation coefficient. This is equal to [97]

$$\mu_{eff} = \sqrt{3\mu_a(\mu_a + \mu_s')} \tag{2.4}$$

This is a direct consequence of solving the diffusion equation for an isotropic point source radiator. In tissue. the diffuse fluence dominates over the collimated fluence since there is a much greater probability for a photon to be scattered than be absorbed. A complete derivation of equations (2.3) and (2.4) is available in a text written by Duderstadt and Hamilton [26].

2.3.2 Measurement of Fluence

Light fluence can be measured in tissue using a fiber with an isotropic sensing tip and a detector [123]. The tip accepts photons ideally from all directions which then travel down the fiber to be detected by a photo-detector. The tip is commonly constructed from a highly scattering material in the shape of a sphere or short cylinder [123]. Using this dosimetry probe. fluence measurements can be made at a radial distance. r, away from the source. The optical coefficients can be determined experimentally by moving the probe over a range of distances and applying the fluence rate relationships of equation (2.3) or

(2.2) above. For scattering media, equation (2.3) indicates that the slope of the straight line curve of $ln(\phi \cdot r)$ gives the effective attenuation coefficient. Similarly, in a purely absorbing medium, the absorption coefficient is equal to the slope of $ln(\phi \cdot r^2)$ as derived from Beer's law (equation (2.2).)

Another method of measuring the absorption coefficient is to use a spectrophotometer, which is a device that measures the absorption spectrum of a non-scattering material. It uses two collimated beams to measure the optical density (OD) of a material. The OD is defined simply as the logarithm of the reciprocal of transmittance T_r. The transmittance can be calculated from the ratio of the light intensities of a reference beam and a beam that passes through the sample of thickness, d. If the beam is assumed to be extinguished in a Beer's law fashion, the absorption coefficient is related to the OD such that

$$\begin{aligned} OD &= log_{10}(1/T_r) \\ &= -log_{10}(\frac{I(d)}{I_o}) \\ &= -log_{10}(e^{-\mu_a d}) \\ &= \mu_a d \cdot log_{10}(e) \end{aligned}$$

Upon rearranging and solving for μ_a, this gives:

$$\mu_a = \frac{OD}{d} log_{10}(e) \tag{2.5}$$

Finally, the absorption coefficient and the scattering coefficient are both wavelength dependent. Therefore, the measurement of the optical properties should be performed at the same wavelength as the irradiation wavelength intended for inducing thermal damage.

2.3.3 Poisoned Moderator Technique

The optical properties of the albumen phantom were determined by the poisoned moderator technique of neutron transport physics [123,124]. This technique involves the measurement of the attenuation of light in samples "poisoned" with increasing concentrations of absorber. The absorption coefficient is equal to the total absorption of the dye and the medium. Therefore, the effective attenuation coefficient given in equation (2.4) expands to

$$\mu_{eff}{}^2 = 3 \cdot [\mu_{ap} + \mu'_{ad}] \cdot ([\mu_{ap} + \mu'_{ad}] + \mu'_{sp}) \tag{2.6}$$

where μ'_{sp} equals the reduced scattering coefficient of the phantom and μ_{ap}, μ_{ad} are equal to the absorption coefficient of the phantom and the dye respectively. For media where

scattering events occur much more frequently than absorption events, it can be assumed that $(\mu_{ap} + \mu_{ad}) << \mu'_{sp}$. Thus, equation (2.6) simplifies to:

$$\begin{aligned} {\mu_{eff}}^2 &\simeq 3 \cdot (\mu_{ap} + \mu_{ad}) \cdot (\mu'_{sp}) \\ &\simeq 3\mu_{ap}\mu'_{sp} + 3\mu_{ad}\mu'_{sp} \end{aligned} \tag{2.7}$$

This also assumes that the scattering coefficient does not change due to the presence of the added dye. Equation (2.7) demonstrates that the scattering and absorption coefficient of the phantom (μ'_{sp} and μ_{ap}) can be determined from the slope and intercept of the plot of μ^2_{eff} versus μ_{ad}. The independent variable of this plot, μ_{ad}, can be controlled by doping a series of albumen phantoms with different quantities of dye of known absorption coefficient which can be calculated stoichiometrically according to concentration. The effective attenuation μ_{eff}, can then be obtained experimentally for each sample by measuring the fluence as a function of radial distance as previously described.

2.4 Materials and Methods

2.4.1 Albumen Phantom

Design and Construction

The albumen phantom consisted of chicken egg albumen (Crude, Grade II, Sigma, Oakville, Ontario), bacteriological agar (Agar #1, Oxoid, Basingstoke, Hampshire, England) and Naphthol Green dye (Sigma). The phantom was constructed by combining two mixtures: a stock albumen solution and an agar-dye solution.

Stock solution of albumen was prepared by dissolving powdered egg white in distilled water in the mass ratio listed in table 2.1. This was filtered through a fine mesh strainer producing a translucent, homogeneous, yellow liquid which was refrigerated when not in use. Table 2.2 lists the composition of six agar solutions which were prepared indi-

Component	Stock (% by weight)	Phantom (% by weight)
albumen powder	22.24	11.87
distilled water	77.76	41.50

Table 2.1: Composition of albumen powder and water in the albumen stock solution (first column) and within the overall albumen phantom (second column). Density = 1.013 g/mL.

vidually. Each solution contained agar, dye and water. The dye was prepared as a stock solution in advance which increased the ease of use and also ensured consistent levels of dye concentrations from sample to sample. The stock solution consisted of 0.387 g of Naphthol Green dissolved in 1 L of distilled water to give a $0.03870 \pm 0.0005\%$ by volume dye concentration. A spectrophotometer (UV160, Mandel Scientific Co. Ltd, Guelph, Ontario) was used to measure the spectral absorption of this dye which was equal to μ_a of 5.90 ± 0.05 cm^{-1} at 805 nm, the wavelength of our laser source.

The dye compositions were calculated such that the absorption coefficient increased by 0.32 cm^{-1} between successive samples. The albumen phantom contained the lowest dye concentration. The other albumen samples were "poisoned" with increasing concentrations of dye. The agar solution was prepared by combining the dye and distilled water which

Added μ_a (cm^{-1})	Naphthol Green (% by weight)	Distilled Water (% by weight)	Agar (% by weight)	Albumen Stock (% by weight)
0.00	13.3	32.0	1.4	53.4
0.32	18.6	26.7	1.4	53.4
0.64	23.9	21.3	1.4	53.4
1.96	29.2	16.0	1.4	53.4
1.28	34.5	10.7	1.4	53.4
1.60	39.8	5.4	1.4	53.4

Table 2.2: Composition of albumen phantoms. The first row is the composition of the albumen phantom. The other rows are the poisoned samples used in determining the optical properties of the phantom. Density of 1.013 g/mL.

was heated to approximately 70 °C. The agar powder was slowly added and dissolved until the boiling point (85 °C) of the mixture was reached. The solution was cooled in a warm water bath to about 45 °C. As the agar mixture cooled, the albumen stock solution was warmed in a hot water bath to approximately 40 °C. The albumen was then added to the cooled agar solution and mixed thoroughly with a spatula. The phantom material was poured into a mold and allowed to cool. Cooling the agar prevented it from coagulating the albumen on contact, whereas heating the albumen avoided uneven gelling and bubble formation within the agar solution. This process was repeated for all dye concentrations listed in table 2.2. The phantom solidified at 38 °C and reached room temperature after approximately two hours of cooling.

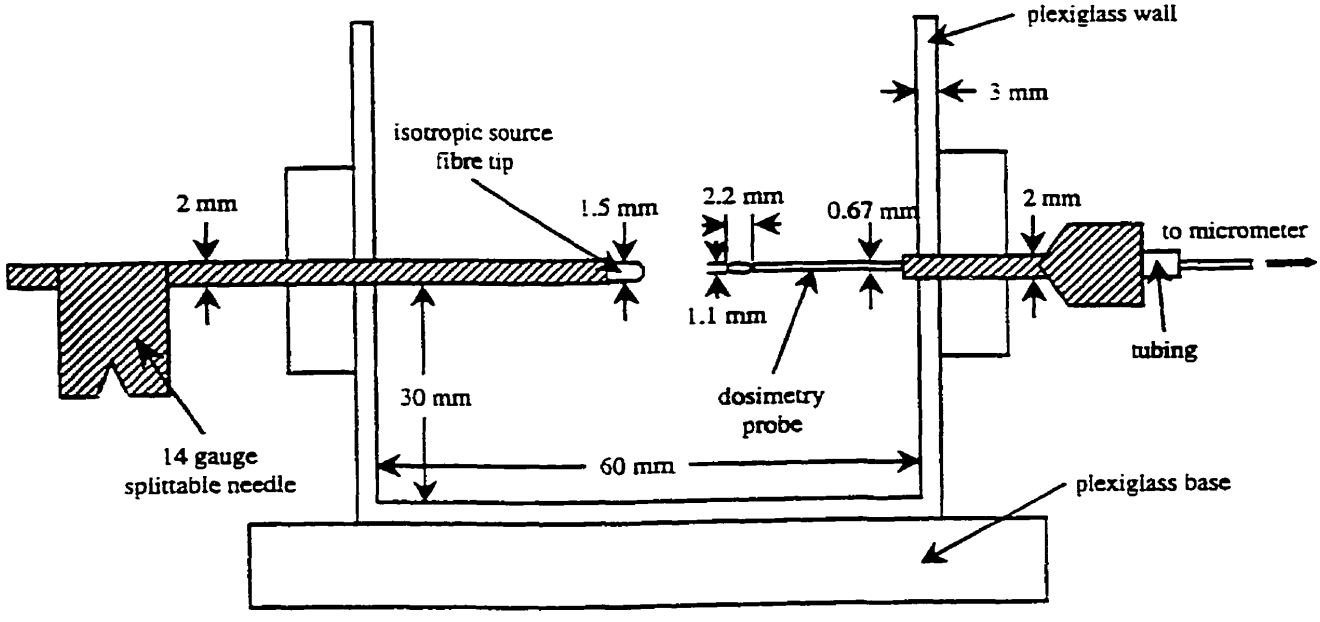

Figure 2.1: Schematic diagram of apparatus used to measured the fluence rate within phantoms.

Determining Optical Properties

The optical properties of the albumen phantom were determined using the poisoned moderator technique by measuring the fluence rate within the albumen phantom and samples. The fluence rate of the albumen samples was measured in a plexiglass box with inner dimensions of $6 \times 6 \times 6\,cm$. A diagram of this box is shown in figure 2.1. The purpose of this apparatus was to provide reliable and stable positioning of the source fiber and dosimetry probe within the sample. The source fiber was a commercially available optical fiber with a spherically diffusing tip (Pseudosphere. Rare Earth Medical. West Yarmouth. Massachusetts) which was designed to radiate isotropically. The diameter of the fiber tip was 1.5 mm. The isotropic dosimetry probe was constructed by creating a diffusing tip at the end of a $600\,\mu m$ plane cut end fiber. The method of construction is explained in appendix A.

The source fiber was held in place by a 14 gauge needle which was inserted through a hole at the centre of one side of the box. The source fiber was placed such that the diffusing tip extended beyond the sharp end of the needle. A shortened 14 gauge needle was secured through a second hole on the opposing box face. The dosimetry probe was inserted into this second needle and held in place by a small piece of plastic tubing. The tubing acted as a sleeve that centered the fiber portion within the short needle. The axes of the source and sensing probes were aligned by visual inspection. Outside the box. the dosimetry

fiber was attached to a micrometer controlled translation stage (Thorlab, Newton, New Jersey) to vary and measure the distance between the optical source and dosimetry probe. Testing of the fluence apparatus was performed by measuring the absorption coefficient of different concentrations of dye in water. This was performed to demonstrate that radial fluence measurements could be accurately made in a liquid medium of known optical properties. The absorption coefficient of the samples was confirmed independently by spectrophotometer measurements.

The albumen phantom and poisoned samples were solidified in advance in six individual plexiglass molds with the same dimension as the fluence box apparatus. The first albumen phantom was removed from its mold and placed in the box. The source needle was inserted into the sample. The isotropic fiber tip was then fed inside the needle and was exposed at the sharp tip of the needle. The fiber was coupled to a NIR 805 nm laser diode (Diomed-15, Diomed Ltd., Cambridge, UK) via an SMA 905 connector. The end of the dosimetry probe fiber was directed at a silicon photo-detector (PDA50, Thorlab). The detector output, displayed on a voltmeter, was proportional to the fluence rate [7]. On the lowest power laser setting (500 mW), the dosimetry tip was moved toward the source fiber using the translation stage over a total distance of approximately 0.5 cm to 1.5 cm. The micrometer scale, r, and the photo-detector voltages, V, were recorded every 0.5 to 1 mm. The effective attenuation coefficient was determined by plotting $ln(V \cdot r)$ versus r. The sample was removed and returned to its original mold.

The radial fluence measurement was repeated for the poisoned albumen samples. The base phantom and the poisoned samples were then heated together in a large water bath. To ensure complete coagulation of the entire phantom, a heating regime of 85 °C for 45 minutes. The fluence rate measurements were conducted again for all the albumen phantom samples in the coagulated state. Care was taken to avoid the same fiber track created in the first set of measurements which were performed in the native state. The optical properties of the albumen were determined in accordance with equation (2.7) as a function of added absorber concentration values listed in table 2.2.

Note, to ease the removal of the albumen and polyacrylamide phantoms from the apparatus, a narrow rectangular piece of tin foil was molded to the bottom of the box and draped over the sides. The sample was placed on top of the tin foil within the box and was removed by lifting the draped sides of foil. The box was sufficiently large (and the sample sufficiently attenuating) such that the light fluence was measured to be negligible at the edge of the box, eliminating the possibility of error due to light reflections from the foil.

Component	Stock (% by weight)
Acrylamide	26.00
N,N'-methylenebisacrylamide	0.20
Sodium Chloride	1.05
De-ionized water	71.70

Table 2.3: Composition of the acrylamide stock solution [102]. Density of 1.017 g/mL.

2.4.2 Polyacrylamide Phantom

A second set of control phantoms were made with polyacrylamide gel. They were used to demonstrate the thermal response with static optical properties. Control phantoms were designed to match the optical properties of the albumen in the native and coagulated states. by adding appropriate amounts of dye and scattering solution.

Design and Construction

A stock solution of liquid acrylamide was prepared according to the method developed by Surowiec *et al* for use as a tissue-equivalent material for microwave applicators [102]. The composition of this solution which consists of acrylamide, N,N'-methylenebisacrylamide, sodium chloride and water is listed in table 2.3. Polyacrylamide was formed by reacting the solution with the catalysts. TEMED and a 10% by volume solution of ammonium persulfate (APS) causing an exothermic reaction. With the addition of the catalysts. the solution was mixed vigourously for approximately one minute and poured into the mold. The solidification process began after approximately 5 minutes after the catalyst was added. The phantom was completely polymerized after a period of about two hours. Cooling of the sample required an additional 3 to 4 hours.

To match the optical properties with those of albumen. the dopants. Naphthol Green and Intralipid-10%. were added to the liquid-phase solution of polyacrylamide. The Naphthol Green was a $0.2100 \pm 0.0005\%$ by volume solution with an absorption coefficient of 32.30 ± 0.05 cm^{-1} at 805 nm which was measured in the spectrophotometer. Initial attempts at combining the polyacrylamide with the dye resulted in a visible bleaching reaction between the APS and the dye. which was manifested as a fading of the green colour of the sample during the polymerization process. To quantify the bleaching phenomenon. the absorption coefficient of purely absorbing samples were measured with the

spectrophotometer, 1 minute, 2 hours and 18 hours after reacting the polyacrylamide with the catalyst.

The scattering coefficient of Intralipid-10% was characterized in polyacrylamide samples with varying concentrations of Intralipid-10% with equal concentrations of dye of known μ_a. The effective attenuation coefficient, μ_{eff}, of the samples was measured in the same fluence box apparatus used for the poisoned moderator technique. The samples were measured while in their liquid phase before polymerization or bleaching occurred. From these curves, μ_s' was calculated from the known value of μ_a and the measured value of μ_{eff} by applying equation (2.4).

The final effective attenuation coefficients of the polyacrylamide phantoms were examined in liquid polyacrylamide samples with the addition of both Intralipid-10% and dye. They were compared with the fluence rates measured in the native and coagulated albumen phantoms.

2.5 Results

The fluence box apparatus was designed to measure radial fluence to determine the optical properties, (μ_a and μ_s' from μ_{eff}) of the phantoms. Unfortunately, test samples of known absorbing and scattering properties at 805 nm were unavailable. Therefore, testing of the apparatus could only be performed on purely absorbing materials which could then be independently confirmed with spectrophotometer results. Four dye samples of known absorption coefficients were tested in the fluence box with the source and sensing probes. The absorption coefficients measured in the fluence apparatus versus predicted values were compared with spectrophotometer results at 805 nm (see figure 2.2). The measured values corresponded well to the predicted values. The agreement suggested that fluence profile measurements of the phantom samples could proceed in the fluence box apparatus with confidence.

The fluence profiles of the albumen phantom and its poisoned samples were measured in the fluence box apparatus to determine its optical properties using the poisoned moderator technique. Figure 2.3 and figure 2.4 are the radial fluence rate plots for the native and coagulated states of the phantom respectively. The effective attenuation coefficient of the phantom in the two states was calculated from the slopes of these curves. The square of the effective attenuation as a function of added absorber is plotted in figure 2.5. The optical properties of the base albumen phantom were calculated from the slope and intercept of this plot using the equation (2.4). The optical properties of the albumen are

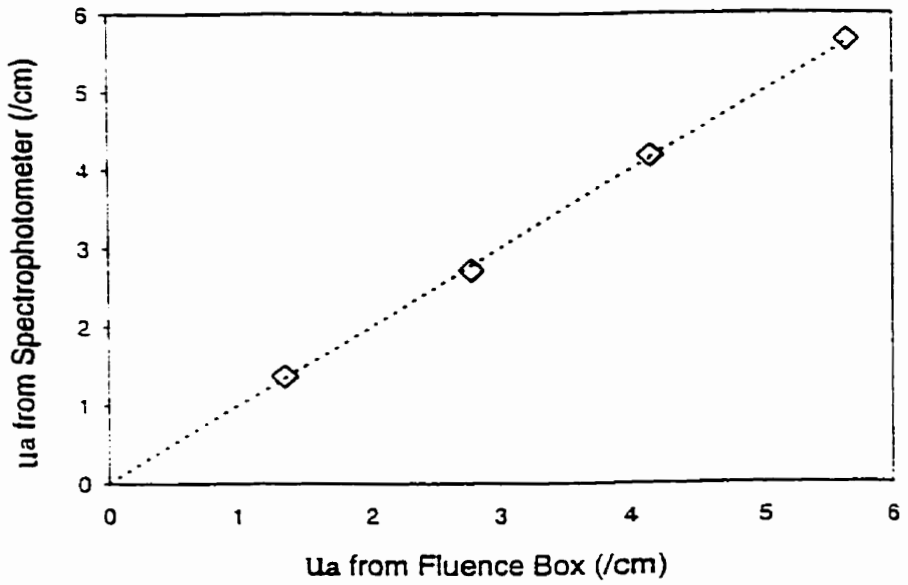

Figure 2.2: Experimentally determined absorption coefficients of dye samples at 805 nm compared with spectrophotometer results. Concentration of dye samples: 9.5, 19.1, 28.6 and 38.2 $g \cdot \mu l^{-1}$

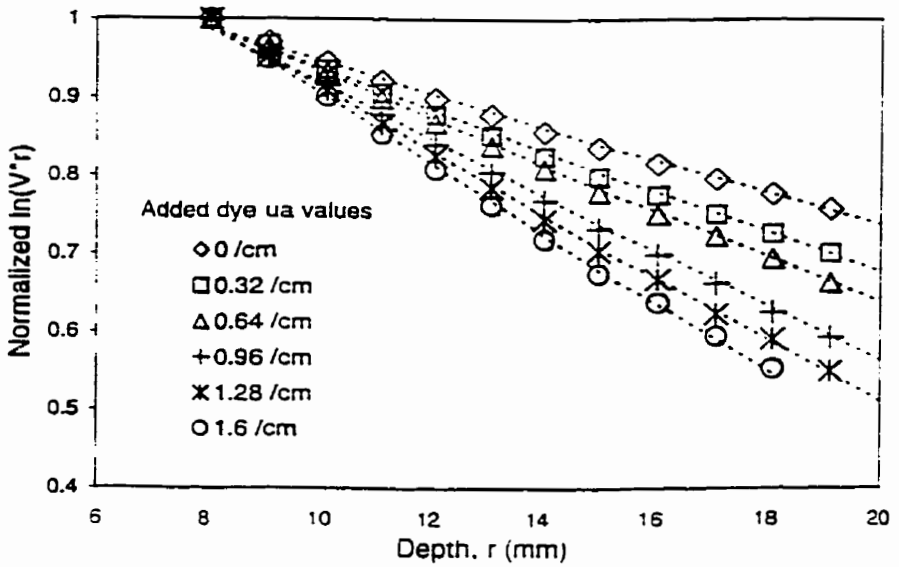

Figure 2.3: Fluence rate as a function of radial distance for the base albumen phantom and the doped samples in the native state.

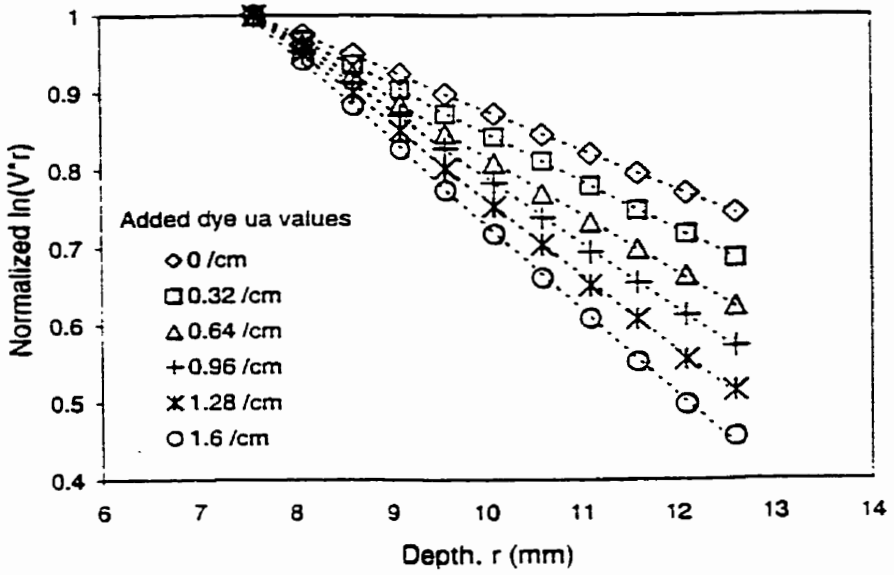

Figure 2.4: Fluence rate as a function of radial distance for the base albumen phantom and the doped samples in the coagulated state.

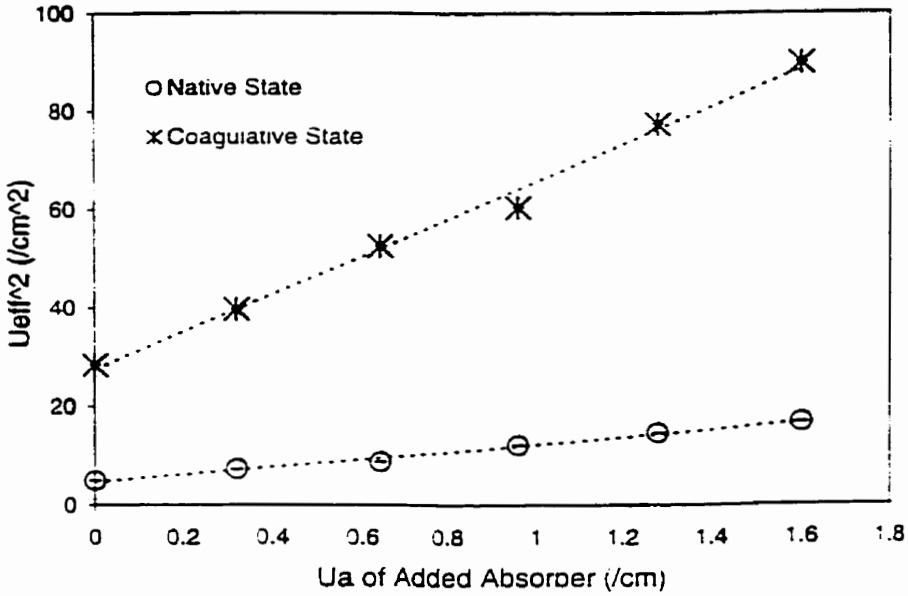

Figure 2.5: Plot of μ_{eff}^2 against added absorber μ_a used to determine the optical properties of the albumen base phantom.

State	μ_a (cm^{-1})	μ_s' (cm^{-1})	μ_{eff}(cm^{-1})
Native	0.50 ± 0.04	2.67 ± 0.07	2.2 ± 0.2
Coagulated	0.7 ± 0.1	13.1 ± 0.5	5.3 ± 0.6

Table 2.4: Optical properties of albumen in the native (room temperature) and coagulated (45 minutes at 85°C) states.

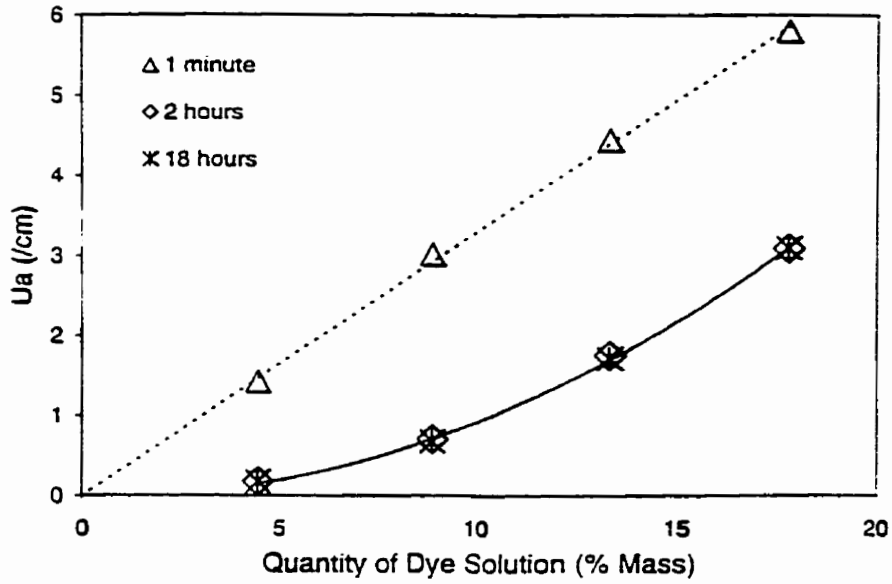

Figure 2.6: The absorption coefficient of acrylamide before and after polymerization - spectrophotometer measurements

shown in table 2.4. There was a 1.4 fold increase in μ_a and a 4.9 fold increase in μ_s' from the native to coagulated states.

Control polyacrylamide phantoms were designed to match the optical properties of the albumen in the native and coagulated states, by adding appropriate amounts of dye and scattering solution. Normally to determine the amount of dye to add to an optically clear material, one can use stoichiometric calculations. However, since APS causes bleaching of the dye, an increased amount of dye was necessary. In order to determine how much dye should be added to compensate for the effect of bleaching, the absorption coefficient was measured using a spectrophotometer at various time points for different amounts of dye. The absorption coefficient of phantoms with four different dye concentrations, measured at 1 minute, 2 hours and 18 hours after the addition of the catalysts to the liquid acrylamide is shown in figure 2.6. Figure 2.6 shows a drop in absorption due to

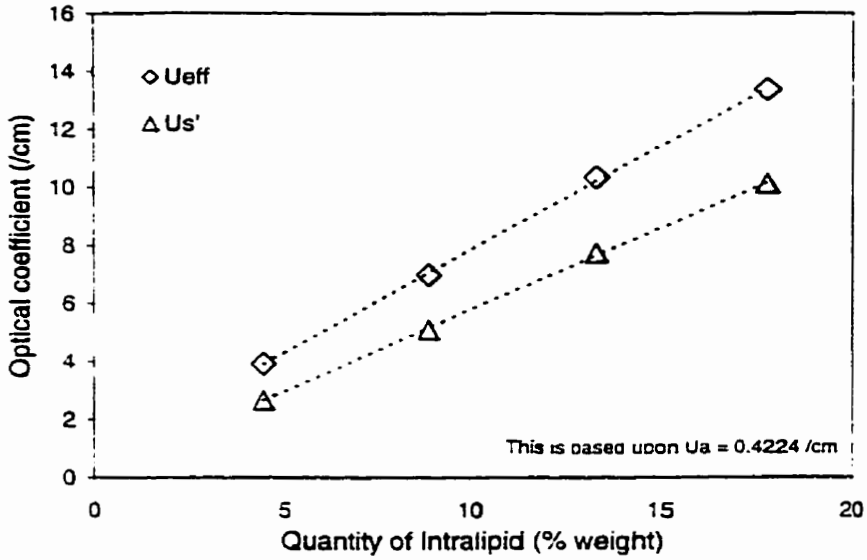

Figure 2.7: The μ_s' and μ_{eff} of polyacrylamide samples with varying concentrations of Intralipid.

the chemical bleaching process. There was no further change in absorption after 2 hours. By interpolating between the points of the final lower absorption curve. the percent mass concentrations of dye solution required to match the native and coagulated properties of the albumen phantoms. were calculated to be 7.8 % and 9.0 %. These values are recorded in table 2.5.

The scattering characteristics of the Intralipid-10% in the polyacrylamide phantom were determined using fluence box measurements by measuring the effective attenuation coefficient of six different concentrations of Intralipid-10% prior to the polymerization reaction. The scattering coefficient was calculated from μ_{eff} (equation (2.4)) and plotted against the concentration of Intralipid-10% by percent weight in figure 2.7. This plot indicates that the scattering coefficient was proportional to the concentration of scattering material. By interpolating between the points of this curve. the percent concentration of Intralipid-10% was determined to be 4.40 ± 0.04 % and 22.5 ± 0.2 % to match the native and coagulated scattering coefficients of the albumen phantom respectively. The final composition of the polyacrylamide phantoms is summarized in table 2.5. The overall final effective attenuation coefficients of the polyacrylamide phantoms. with both Intralipid-10% and dye was compared with the albumen phantom in order to confirm that the optical properties were matched. A plot of the fluence profile for the two phantoms. shown in figure 2.8. suggests that they possess equivalent optical properties resulting in the same

Component	Native State Albumen Matching (% by weight)	Coagulated State Albumen Matching (% by weight)
Naphthol Green (0.210%)	7.8	9.0
Intralipid-10%	4.4	22.5
Distilled Water	40.16	20.91
Acrylamide Stock	46.63	46.63
APS (10% by volume)	0.65	0.65
TEMED[a]	0.35	0.35

Table 2.5: Composition of the polyacrylamide phantom designed with optical properties matching albumen. [a]N,N,N',N-tetramethylethylenediamine

effective attenuation coefficient.

2.6 Discussion

A phantom was developed with dynamic optical properties for use with laser photocoagulation studies. The phantom consisted of albumen combined with an NIR absorbing dye (Naphthol Green) and agar. The optical properties of the phantom were determined at a wavelength of 805 nm using the poisoned moderator technique. This is a common wavelength for laser induced coagulation applications such as ILP. The μ_a and μ_s' in the native state of the albumen phantom were 0.50 ± 0.04 cm^{-1} and 2.67 ± 0.07 and in the coagulated state were 0.7 ± 0.1 cm^{-1} and 13.1 ± 0.5 cm^{-1} respectively. These values are within typical ranges of tissue in both the native and coagulated stated. with the exception of a low native value of μ_s'. For example measurements on human prostate at 850 nm yielded μ_a =0.6 cm^{-1} and μ_s' =6 cm^{-1} in the native state and μ_a =0.7 cm^{-1} and μ_s' =13.8 cm^{-1} in the coagulated state [88].

It is difficult to confirm our measured optical properties of the albumen phantom against data from literature for albumen alone which is limited. Pickering performed measurements at 800 nm by measuring the reflectance and transmittance of the sample using integrating spheres. His results yielded a μ_s' of 6.9 cm^{-1} for albumen which was heated at 70°C for 1000 seconds and a μ_s' of 17.1 cm^{-1} cooked at 75°C for the same heating time. There are two points to be made with regard to these results. First. Pickering measured a considerable difference in scattering coefficient for the two temperature ranges (6.9 cm^{-1} versus 17.1 cm^{-1}). Secondly, we would expect our measurements of μ_s' to be

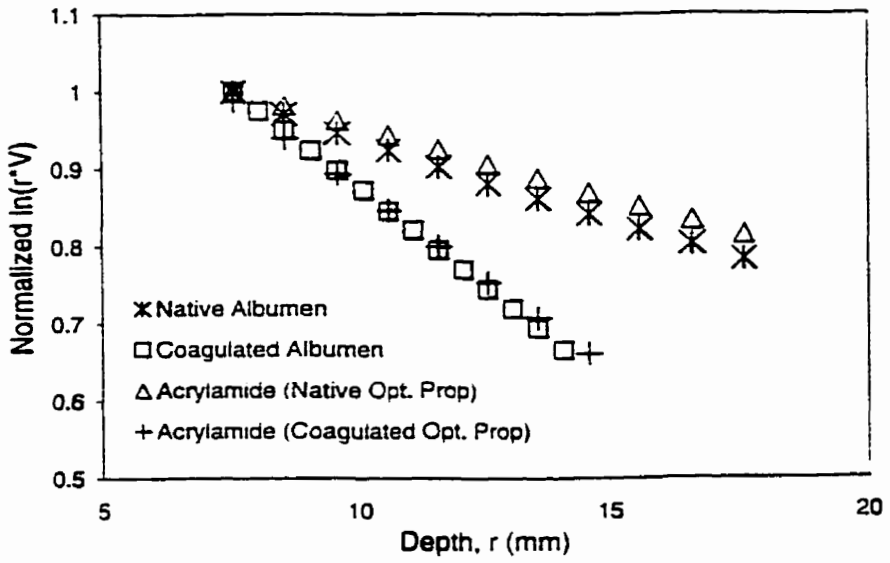

Figure 2.8: Comparison of μ_{eff} between the albumen and doped acrylamide phantoms confirming matched optical properties of the two phantoms.

slightly higher than the results measured by Pickering due to the addition of agar, (a scattering material) and the longer heating regime (85°C for 45 minutes). We cannot explain these discrepancies.

The practical advantages of the albumen phantom are numerous. It is completely non-toxic, simple to make, easily poured into molds, and very cost efficient ($\simeq$ $12.00 per liter). It can also be cleanly sliced or scraped to any shape, and produces clearly visible zones of thermal coagulation to the naked eye. Furthermore, the absorbing dye is also chemically stable in the short NIR wavelengths over several months[1].

The disadvantage of the tissue equivalent material is that it lasts for only about 1-2 weeks and must be refrigerated. As well, the agar matrix may liquefy as it is being heated[2]. This may result in the presence of unpredictable thermal effects in the phantom such as changes in thermal properties and convection. Another potential concern is the formation of bubbles in the phantom if the albumen stock is over-mixed.

Polyacrylamide phantoms were developed whose optical properties do not change with temperature. This phantom can be used as a reference medium to illustrate the difference in measurements when heat-induced changes in optical properties are not accounted

[1]Several other NIR absorbers were found to bleach with time. They include QSwitch 1, QSwitch 5, and IRA980.

[2]Crosslinking with formalin may increase the melting point.

for. The optical properties of the phantoms were matched with those of the albumen phantom by adding Naphthol Green and Intralipid-10%. A 0.2100 ± 0.0005 % solution of Naphthol Green at a concentration of 7.8 % by weight and Intralipid-10% at a concentration of 4.4 % by weight, was added to a polyacrylamide solution to mimic the native properties of the albumen phantom. For the coagulated state, 9.0 % by weight of Naphthol Green and 22.5 % by weight of Intralipid-10% was added to polyacrylamide. However, in general, the optically clear nature of polyacrylamide allows one to dope it to produce a wide, varying set of tissue like optical properties, by modifying the concentration of dye and scattering materials. We have demonstrated that the optical properties could then be experimentally determined and verified easily using fluence measurements and diffusion theory.

Like the albumen phantom, polyacrylamide also offers many advantages It is simple to make, easily poured into molds and cost efficient ($10.00 per liter). Advantages of polyacrylamide over other phantoms are that it can be stored for several months, it is homogeneous, reproducible and clean to work with.

The main weaknesses of the polyacrylamide phantom construction and measurement methods involved two aspects. First, fluence rate measurements of the phantom had to be performed while in its liquid unpolymerized form. Two different failed attempts were made to measure fluence rate after polymerization occurred. One method involved setting the optical probes in place and allowing the polyacrylamide to be molded within the apparatus. After the phantom polymerized, the dosimetry probe was then moved away from the source probe within the track formed by the fiber portion of the dosimetry probe. The other method attempted to pierce the polymerized phantom through an entry slit with the dosimetry probe. Both produced unpredictable, irreproducible results. This is a result of the invasiveness of the methods such that they affect the distribution of light within the phantom. Therefore, all instrumentation must be placed in the phantom while in its solution form.

The inability to measure fluence of the phantom in its polymerized state leads to some uncertainty in the final scattering characteristics of the polyacrylamide phantom. Changes in the orientation and/or position of the scattering particles may occur due to settling of the Intralipid-10% during the polymerization process. Other possible changes due to polymerization include the index of refraction of the polymerized state and/or changes due to a chemical reaction with the catalysts or other base materials. The influence of these errors, however, appear to be minimal. This was confirmed by measuring the temperature rise in the polyacrylamide phantom in the solidified state and comparing them

to theoretical predictions. Good agreement between predicted and experimental values suggest that any possible changes in optical properties that may occur during the polymerization process, do not interfere at least with practical measurements of temperature elevation in the phantom. The second problem of using polyacrylamide was the effect of the catalyst, APS, on the absorption characteristics of Naphthol Green. This resulted in a bleaching effect which had to be compensated for by increasing the initial concentration of dye. Furthermore, as shown in figure 2.6, the bleaching effects were dependent upon the concentration of dye added which complicates the issue. Finally, polyacrylamide in its liquid phase is a neurotoxin. Therefore, safety handling procedures must be employed prior to polymerization[1].

For opto-thermal studies, the phantoms should have thermal properties, as well as optical properties, that are similar to tissue. The thermal properties of the albumen and polyacrylamide phantoms were not measured. However, since the albumen material is completely organic and consists mostly of water, the thermal properties are likely to be similar to those of tissue. The polyacrylamide phantom, though synthetic, may also be similar to tissue since it is composed mostly of water as well. Its thermal properties can be estimated according to its water content [104]. This method has previously shown high accuracy for other artificial water based materials such as gelatin [25].

2.7 Conclusions

Two phantoms were developed and characterized that possess either dynamic optical properties (albumen phantom) or constant optical properties (polyacrylamide). The optical properties of the albumen phantom were measured in both its native and coagulated states and were matched in the polyacrylamide phantoms which are similar to tissue at NIR wavelengths. As such they may be used in future investigations which study the opto-thermal response of tissue due to laser irradiation.

[1]Once polymerized, polyacrylamide is safe to handle [102]

Chapter 3

Modeling of ILP

3.1 Abstract

The theoretical study of the effects of changing optical properties during laser irradiation provides important insight into the formation of thermal lesions during ILP. This information will be essential for the successful planning of thermal therapy treatments to achieve complete tumour destruction sparing healthy tissues without inducing vapourization and charring. A nonlinear mathematical model was developed that quantifies the effects of changing optical properties on fluence, temperature and damage predictions. This was performed by using the Arrhenius damage formulation to relate the temperature rise to fluence changes. Changes in optical properties were handled by solving the two layer analytical solution of the light diffusion approximation. Temperature rise in tissue was estimated using the bioheat equation and solved with a nonlinear algorithm for the finite difference method (FDM).

To experimentally validate the nonlinear model, temperatures were measured in an albumen phantom whose optical properties change during heating. Measurements were also performed in polyacrylamide phantoms with static optical properties, to illustrate the difference in temperature rise when dynamic optical properties are not taken into account. The experimental measurements agreed well with theoretical predictions validating the use of the Arrhenius damage formulation to describe dynamic changes in optical properties. Our theoretical and experimental results indicate that coagulation causes a sudden increase in the rate of temperature rise due to a decrease in light penetration within the coagulated region close to the light source. The significance of these findings were investigated in a clinical example: ILP of the liver. The liver studies were conducted with a constant

laser power such that the peak temperature was just below vapourization at the end of the 15 minute irradiation time. The model predicted that changes in optical properties cause larger gradients of light fluence in the coagulated region of tissue surrounding the fiber tip as a result of reduced light penetration. A sudden increase in temperature rise was observed in the liver studies at the onset of coagulation in a fashion similar to that observed in the albumen phantom. The dynamic changes in optical properties have the largest impact on peak temperature predictions close to the fiber tip. This information may be important in order to avoid using excessive powers which may induce vapourization and charring. The final damage volume was approximately the same as that predicted by the static case of coagulated optical properties. However, the laser power requirements are considerably different between the dynamic and static models. In general, the results suggest that the features of lesion formation are highly dynamic due to the coagulation process. This validates the need for theoretical investigations to account for the effects of changing optical properties in models of ILP.

3.2 Introduction

The use of an optic fiber to deliver light, percutaneously, into tissue was demonstrated in the early 1980s as a viable means of heating and destroying deep seated tumours [13]. A number of subsequent studies have been aimed at modeling and understanding the thermal response of tissue due to light during ILP [63, 114, 116, 129].

The conventional model of ILP consists of the three basic calculations of the 1) light distribution, 2) temperature rise and 3) the extent of thermal damage. Each stage of modeling requires information from the previous stage and from experimental measurements of tissue properties (Refer to figure 1.1 from chapter 1). The forward progression of calculation results in what is referred to as a *linear* model for thermal therapy since the inputs of the bioheat equation are not temperature dependent. Most, thermal models of ILP used this linear approach [5, 9, 84].

In reality, however, the elevation of tissue temperature itself causes dynamic changes in tissue which in turn affect the fluence distribution and/or the temperature field. Thermal [25, 116], optical [25, 47, 51, 79, 80], and blood perfusion [16, 29, 66, 87, 92] properties of tissue are altered when the tissue is heated. This situation can be modeled by coupling the temperature prediction with the dynamic properties which results in a nonlinear model of the bioheat equation. Currently, nonlinear models exist which account for changes in optical properties [84], changes in blood perfusion [100, 101], or a combination of both

[9,37.49.57.62.89.125].

Various methods have been used to model the change in optical properties during heating. One method assumes that tissue possesses native optical properties initially, which are then replaced by coagulated tissue properties once a certain critical temperature is reached [9,89,125]. This method is based upon the heuristic assumption that photocoagulation occurs at a critical temperature (60°C) [89.125]. The vast majority of methods, however, use the Arrhenius damage model to describe the heat-induced effects on changes in optical properties [9,37.57.84.89]. However, to the author's knowledge, this assumption has not been confirmed yet in the literature. As well, many models include both effects of changing optical properties *and* blood perfusion [9,37.49.57.62.89.125]. As such, their results would be difficult to confirm experimentally since dynamic changes in blood perfusion would require an *in-vivo* animal model. Furthermore, in general, the effects of dynamic blood perfusion are not well known in the coagulated temperature range.

Rastegar *et al* examined the influence of changing optical properties alone without considering the effects of dynamic blood flow. They conclude that the effects of changing optical properties cause larger temperature gradients and higher peak temperatures as a result of reduced penetration of light [84]. The simulation, however, used short irradiation times on the order of seconds. Furthermore, the laser power was not scaled such that the peak temperature was below vapourization in order to avoid charring while sparing normal tissues. They also did not experimentally verify their results. Therefore, the development and experimental verification of a nonlinear ILP model for treatments below the vapourization threshold, which examines and isolates the effects of dynamic optical properties, is necessary.

Hence, the purpose of this chapter is to first propose a new model which includes changes in optical properties based upon the Arrhenius damage model. Experimental work is then presented demonstrating the effects of changing optical properties using phantoms. Finally, the model results are investigated in a clinical example of ILP of the liver.

There are many different methods of calculating the deposition of light in tissue. Currently, the Monte Carlo particle simulation method is most often used to describe light propagation in photocoagulation studies [37,62,84,90]. The Monte Carlo method is based on an algorithm where photons are mathematically injected into the medium one-by-one and traced until they are either permanently ejected out of the medium or absorbed within the medium. The random sampling from appropriate probability distributions of the relevant tissue properties, which affect the propagation of each photon, results in a overall estimate of the light distribution due to all photons. The advantages of this method are

its conceptual ease of implementation, and its ability to handle complex geometries and optical inhomogeneities [75]. As a result, many investigators have used this method to describe irregular shapes and tissue boundaries of interstitial applicators [37,57,99]. The major disadvantage of the Monte Carlo method is that it can be impractical due to the large computational resources required. An alternative method is to exploit the diffusion approximation of light propagation.

The diffusion approximation is a differential equation which approximates radiative transport theory. The advantages of this method is its ease of implementation and its reduced computation time. In addition, for simple geometries, it agrees well with Monte Carlo results [90]. A limitation of diffusion theory is that the accuracy close to the boundaries [44,90] or within highly absorbing regions [35,44] is poor. However, for most tissue types in the near infrared wavelength range, the diffusion theory offers a fast and reasonably accurate method of calculating the light distribution in tissue. Analytical solutions of the diffusion approximation are available for some geometries. This is preferable because analytical solution do not encounter reduced accuracy due to discretization. Unfortunately, however, analytical solutions do not always exist. For these cases, numerical methods should be employed.

The calculated light distribution is used as an input to the Pennes bioheat transfer equation. Solutions of the bioheat equation cannot be derived analytically, therefore, numerical methods are employed that provide approximate solutions such as the Finite Element Method (FEM) or the Finite Difference Method (FDM). The finite element method discretizes the solution domain into different elements. The bioheat equation is then solved over each element, simultaneously, by satisfying the boundary condition between each element. On the other hand, the finite difference method approximates the differential equation as a set of differences between individual element and solves the differential equation over the entire domain and not over each individual element. As a result, finite differences are advantageous over finite elements in that they are easier to implement, require less memory and have shorter computation time than the finite element method. The FEM, however, is advantageous over the FDM, for complex geometries, since elements can be shaped to fit any configuration. Nonetheless, for simple geometries, the finite difference method offers a fast, efficient and accurate method of solving the bioheat transfer equation.

The solution of the bioheat equation gives the temperature as a function of time at all points in the calculation domain. The damage is then calculated using an Arrhenius relationship between temperature and a pathological end point. For example, the Arrhenius formulation has been used to calculate the rate of thermal damage leading to cell death [11]

and changes in optical properties [47, 80]. Damage models can therefore be used to make direct comparisons between predictions of laser damage and histological results of the final lesion. The damage model is also used to describe the pathological changes that occur during heating, giving rise to nonlinear thermal models. For example, damage parameters have been used to describe the heat induced effects of changes in optical properties [84] and blood perfusion [57]. However, one of the goals of this chapter, is to determine the validity of the Arrhenius damage model as a nonlinear parameter to account for the effects of dynamic optical properties.

3.3 Theory

3.3.1 Mathematical Modeling

A model of Interstitial Laser Photocoagulation was developed which predicts the temperature and damage profiles in tissue due to a point source of light. The model includes the transient effects of changing optical properties due to heat by recalculating the light distribution in tissue dynamically. The following sections describe the structure and the method of calculating the light distribution, tissue temperatures and tissue damage.

Light Distribution in Tissue

The light emitted from an interstitial fiber was represented as an isotropic point source radiating at the origin in spherical coordinates. Photon propagation from the source can be described using radiative transport theory [26, 97]. Exact analytical solutions of the radiative transport equation have been found for only a few special cases [75, 97, 129]. However, if scattering processes dominate absorption in the medium, an approximation to the radiative transport equation can be applied [26, 75, 97]. The approximation, referred to as the diffusion approximation, is expressed as:

$$-D\nabla^2\phi(r) + \mu_a\phi(r) = s(r) \text{ where} \tag{3.1}$$

ϕ = light fluence rate $[\ W \cdot cm^{-2}]$

D = diffusion constant $[\ cm\ ]$

$= [3(\mu_s' + \mu_a)]^{-1}$

The quantities μ_a and μ_s' are the same as those discussed in section 2.3. The solution to equation (3.1) depends upon the source term $s(r)$, which represents the distribution of the

first-scattered photons from the light source [110]. For an isotropic point source emitting P_o joules/second within an infinite *homogeneous* medium. the source is represented by

$$s(r) = \mu_s' \frac{P_o}{4\pi r^2} exp(-\mu_{tr}' r) \tag{3.2}$$

where μ_{tr}' is defined as the transport attenuation coefficient and is equal to $\mu_s' + \mu_a$ $[cm^{-1}]$. The analytical solution of equation (3.1) was obtained by assuming that the source acts as a Dirac δ-function [26]. This is mathematically equivalent to the situation where [26]:

$$-D\nabla^2\phi + \mu_a\phi = 0 \tag{3.3}$$

and has boundary conditions:

$$(a) \quad \lim_{r\to 0^+} -D\frac{d\phi}{dr} = \Phi_o \tag{3.4}$$

$$(b) \quad \lim_{r\to\infty} \phi(r) < \infty \tag{3.5}$$

Solving this second order linear differential equation with the boundary conditions gives

$$\phi(r) = \frac{\phi_o\ exp(-\mu_{eff} r)}{4\pi D r} \tag{3.6}$$

This is the contribution of diffuse fluence which is also referred to as the diffuse photon flux [110]. The unscattered (or primary photon flux), falls at a faster rate $(1/r^2)$. Therefore, the contribution of primary photons was minimal and assumed to be negligible.

The absorption of the light fluence by a target molecule or chromophore (such as water, melanin and hemoglobin), causes most of the optical energy to be converted into heat[1] such that the deposited light power is effectively equal to [114]:

$$P(r) = \mu_a\phi(r) \ \ [W{\cdot}cm^{-3}] \tag{3.7}$$

This is a consequence of promoting the target molecule to a vibrational-rotational excited state which then transfers energy to nearby molecules via inelastic scattering manifested as a local elevation in temperature [12].

Bioheat Equation

The local elevation in temperature causes heat transfer in tissue and can be described by the bioheat transfer equation. The bioheat transfer equation was first introduced by Pennes [77] to describe heat transfer in perfused tissue such that

$$\rho c\frac{\partial T(r,t)}{\partial t} = \nabla\cdot(k\nabla T(r,t)) + P(r,t) - w_b c_b(T(r,t) - T_{art}) \tag{3.8}$$

where

[1] a very small amount of energy may be lost through other types of light interactions such as photochemical processes.

T = temperature $[°C]$
ρ = density of tissue $[g \cdot cm^{-3}]$
c = specific heat of tissue $[J \cdot g^{-1} \cdot °C^{-1}]$
k = thermal conductivity of tissue $[W \cdot cm^{-1} \cdot °C^{-1}]$
r = radial distance $[cm]$
t = time $[s]$
T_{art} = temperature of arterial blood $[°C]$
P = deposited light power $[W \cdot cm^{-3}]$
w_b = volumetric perfusion rate $[g \cdot s^{-1} \cdot cm^{-3}]$
c_b = $[J \cdot g^{-1} \cdot °C^{-1}]$

On the right hand side. the first term is the conductivity term which describes the diffusion of heat in tissue. The second term is the deposited light energy or absorbed light power of the optical source. The last term describes the convective effects of blood flow. This is derived from the assumptions that a) arterial blood entering the capillaries instantaneously equilibrates with its surrounding in an infinitesimally small volume of tissue and that b) the venous blood leaving the volume is at the local tissue temperature and has no further effect on the surrounding tissue. As such. it was shown that blood perfusion could be modeled as a heat sink term proportional to the perfusion rate of the tissue [77]. These combined terms lead to an elevation in temperature described by the left hand side of the equation.

The spatial domain of the problem was defined in the region from the radius fiber edge. r_f. to a position sufficiently far in tissue where changes in temperature were negligible. Due to the symmetry of the problem. temperature elevation (as well as light distribution) was solved in the radial direction only.

Thermal Damage Accumulation

The rise in temperature can cause irreversible thermal damage in a manner that can be described from chemical reaction kinetics. In a reaction process. reactants are combined to form products. Similarly. one can consider coagulation as a rate process such that the native tissue are the reactants of the reaction which then undergo a change in state into products which are coagulated. In this way the rate or the velocty of the reaction can be

described by a rate constant. k which can represented as follows:

$$\xrightarrow{k} \tag{3.9}$$

$$\text{Reactants (native tissue)} \longrightarrow \text{Products (coagulated tissue)} \tag{3.10}$$

According to the Arrhenius formulation. the rate constant is temperature dependent such that:

$$k = A \cdot e^{-\frac{E}{RT(r,t)}} \tag{3.11}$$

where

A = frequency factor $[s^{-1}]$
E = activation energy $[J \cdot mol^{-1}]$
R = universal gas constant $[J \cdot mol^{-1} \cdot K^{-1}]$

The frequency factor A. and activation energy E. are derived from thermodynamic values. such as heat of activation ΔH and entropy ΔS that are related to the denaturation process of proteins and other cellular constituents [52]. However. since temperature varies with time, final damage can be quantified by an accumulated rate of damage represented by the damage index. Ω:

$$\Omega(r,\tau) = \int_0^{\tau} A \cdot e^{-\frac{E}{RT(r,t)}}\, dt \tag{3.12}$$

where

Ω = damage index $[dimensionless]$
τ = total heating time $[s]$

A more intuitive form of equation (3.12) is to consider Ω as a measure of the volume fraction of damaged cells which follows from first-order reaction kinetics. Explicitly, Ω is the logarithm of the ratio of the initial concentration of undamaged tissue to that after damage has occurred at time. τ. [76]:

$$\Omega = ln\left(\frac{C(r,0)}{C(r,\tau)}\right) = \int_0^{\tau} A \cdot e^{-\frac{E}{RT(r,\tau)}}\, dt \tag{3.13}$$

Therefore. $\Omega = 1$ corresponds to the condition where 63 % of the cells have been damaged.

The damage parameters. E and A are derived from empirical observations which relate temperature to a thermally induced effect such as cell death. Borrelli *et. al* [11]

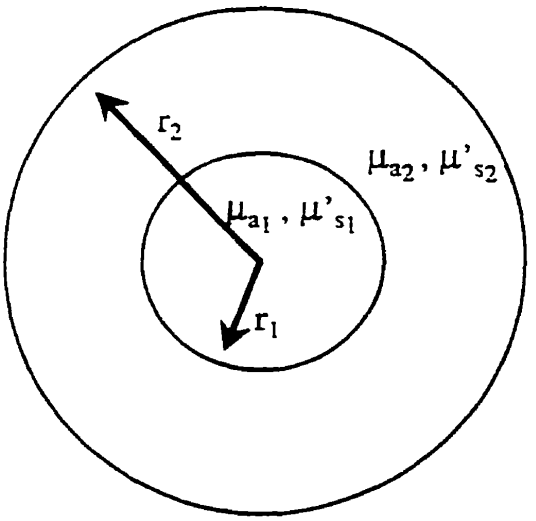

Figure 3.1: Schematic diagram of a two layer case for solving the light diffusion approximation. Regions 1 and 2 represent the inner coagulated and outer native regions respectively. The boundary between the regions is defined as r_o. The region, r_2, extends to infinity which represents an unbounded region of native tissue.

produced survival curves of baby hamster kidney (BHK) cells exposed to a temperature range of 43.5°C to 57.0°C using a colony formation assay. They calculated the Arrhenius damage parameters for cell death ($E = 5.064 \times 10^5$ $[J \cdot mol^{-1}]$, $A = 2.984 \times 10^{80}$ $[s^{-1}]$) by plotting the reciprocal of the slope of the exponential region of the survival curves ($1/D_o$) against the reciprocal of the absolute temperature ($1/T$). D_o is equivalent to the time it takes to reduce the surviving fraction of cells to 37% for a given temperature. Using these E and A parameters for cell death, the Arrhenius integral equation (3.12) was used to calculate the lethal thermal damage due to a temperature rise of $T(r, t)$.

Nonlinear Effects of Dynamic Optical Properties

Coagulation causes a change in the optical properties of tissue which changes both the absorption and reduced scattering coefficients depending upon the tissue type. During ILP, this appears as an inner layer of coagulated tissue surrounded by native uncoagulated tissue [108]. A simple approach to modeling this phenomenon was to solve the light diffusion approximation analytically for a system consisting of two layers with different optical properties. The inner layer represents the tissue which has been coagulated around the tip with coagulated optical properties (μ_{a1}, μ'_{s1}) surrounded by a second layer of native tissue (μ_{a2}, μ'_{s2}). The radius of the second layer extends to infinity to model the case of an unbounded outer region of native tissue (see figure 3.1). The diffusion equation was solved analytically, for ease of calculation and reduced computation time. A

general form of the analytical two layer solution can be found in various texts [97]. The exact coefficients of the general solution must be determined by applying the appropriate boundary conditions. For our model, we assume the boundary conditions at the interface between the two regions requires that the photon fluence rate and the photon current ($D\frac{d\phi}{dr}$) be continuous [110]. Setting the index of refraction between the two media to be equal, this is expressed mathematically as:

$$a) \quad \phi_1(r) = \phi_2(r) \qquad r = r_o \tag{3.14}$$

$$b) \quad D_1\frac{d\phi_1(r)}{dr} = D_2\frac{d\phi_2(r)}{dr} \qquad r = r_o \tag{3.15}$$

where r_o defines the spatial location of the boundary between the two layers and the subscripts, 1 and 2 are the inner and outer regions respectively. The final condition is an energy balance between the two media such that:

$$c) \quad P_o = \mu_{a1}\int_{r_f}^{r_o}\phi_1(r)dV + \mu_{a2}\int_{r_o}^{\infty}\phi_2(r)dV \tag{3.16}$$

where the first integral limit, r_f represents the radius at the fiber edge. These three conditions were used to solve the unknown coefficients for the two layer case. The details of how this is performed are provided in appendix B.

The dynamic solution of the two layer case was calculated by estimating the depth of coagulation, r_o, from the Arrhenius damage integral (equation (3.12)). The damage parameters, E, and A, were obtained from experimental values in literature that measure the rate of change of optical properties, μ_a and μ_s' due to heat for albumen and liver (refer to tables 3.2, 3.6 respectively in section 3.4). The accumulated damage index close to the source is higher than that delivered deeper into tissue. The coagulation front, r_o, was calculated according to the depth at which the damage index, $\Omega(r,t)$, exceeds the mid-point between the native and coagulated states. That is, r_o is the location at which the concentration of native cells is such that

$$\Omega_{opt}(r_o,t) = \ln\left(\frac{1}{2}\right) \tag{3.17}$$

$$= \ln\frac{C(r_o,t)}{C(r_o,0)} \tag{3.18}$$

where $C(r_o,0)$ represents the initial concentration of native cells and $C(r_o,t)$ represents the concentration of native cells remaining at the boundary front, r_o. Continued elevation of temperature with time causes the damage index to exceed the threshold at increasing depths of r_o. A new solution of the analytical two layer model was generated with the advancement of the coagulation depth. This resulted in a time varying absorbed light

power pattern. $P(r,t)$. Changes in $P(r,t)$ affected future temperature calculations which in turn was reflected in the next calculation of the damage index and ultimately the next calculation of deposited light energy.

3.3.2 Numerical Methods

Finite Difference Method

The bioheat equation was solved using the *finite difference method* (FDM). The FDM approximates differential equations by dividing the spatial and temporal domains into discretized points in space (nodes) and time (time-steps). The differential equation of interest is the bioheat equation in spherical coordinates which is a second order partial differential equation:

$$\rho c\frac{\partial T(r,t)}{\partial t} = k\left(\frac{\partial^2 T(r,t)}{\partial r^2} + 2\frac{\partial T(r,t)}{r\partial r}\right) + P(r,t) + w_b c_b\left(T(r,t) - T_{art}\right) \tag{3.19}$$

The continuous function derivatives of the bioheat equation (3.8) are substituted with discrete finite differences. The finite differences are derived from the Taylor series expansion about point, i. The unknown function, (temperature in this case) at point $i+1$ and $i-1$ are thus given by:

$$T_{i+1} = T_i + (\Delta x)T_i' - \frac{(\Delta x)^2}{2!}T_i'' + \frac{(\Delta x)^3}{3!}T_i''' - \frac{(\Delta x)^4}{4!}T_i'''' + .. \tag{3.20}$$

$$T_{i-1} = T_i - (\Delta x)T_i' + \frac{(\Delta x)^2}{2!}T_i'' - \frac{(\Delta x)^3}{3!}T_i''' + \frac{(\Delta x)^4}{4!}T_i'''' - .. \tag{3.21}$$

where Δx is the distance between two adjacent nodes. T_i' is the first derivative at point i, T_i'' is the second derivative and so on. The central difference method of finite differences calculates the value of T_i relative to its forward difference (with respect to T_{i+1}) and its backward difference (with respect to T_{i-1}). This is derived by truncating the Taylor expansion at the Δx^3 term and adding or subtracting the expressions of (3.20) and (3.21) together. With some rearranging, this conveniently yields a set of differences which approximate T_i' and T_i''

$$T_i' = \frac{T_{i+1} - T_{i-1}}{2(\Delta x)} \tag{3.22}$$

$$T_i'' = \frac{T_{i+1} - 2T_i + T_{i-1}}{(\Delta x)^2} \tag{3.23}$$

These equations are called the *central difference formulas.* Substitution of the central difference formulas into the bioheat equation in spherical coordinates for the independent variables, r and t gives:

$$\rho c \frac{T_{i,j+1} - T_{i,j-1}}{2(\Delta t)} = k\left(\frac{T_{i+1,j} - 2T_{i,j} + T_{i-1,j}}{(\Delta r)^2} + \frac{T_{i+1,j} - T_{i-1,j}}{r\Delta r}\right) + P_{i,j} - w_b c_b (T_{i,j} - T_{art}) \tag{3.24}$$

where i represents the index of the spatial node, j the index of the time-step, Δr the spatial distance between nodes and Δt the temporal difference between time-steps. Thus, $T_{i,j}$ and $P_{i,j}$ are equivalent to the approximate value of temperature and deposited light power respectively at spatial position, $i\Delta r$, and time-step, $j\Delta t$.

The explicit finite difference method was used to solve equation (3.24) [20]. This method progresses forward in time calculating the next temperature value ($T_{i,j+1}$) using the temperatures at neighbouring nodes from the previous time-step ($T_{i,j}$, $T_{i-1,j}$ and $T_{i+1,j}$). The process begins by assuming initial conditions of temperature $T_{i,0}$ for all values of i. The temperature profile for the first time-step is then solved by rearranging (3.24) as follows:

$$\begin{aligned} T_{i,1} &= T_{i+1,0}(F_o)(1 + \frac{\Delta r}{r}) + T_{i,0}\left(1 - 2F_o - \frac{w_b c_b \Delta t}{\rho c}\right) \\ &\quad + T_{i-1,0}(F_o)(1 - \frac{\Delta r}{r}) + \frac{\Delta t}{\rho c}(P_{i,0} + w_b c_b T_{art}) \end{aligned} \tag{3.25}$$

where $F_o = \frac{k}{\rho c}(\frac{\Delta t}{\Delta x}^2)$ is called the *Fourier number* [20]. The calculation is then repeated for all subsequent time-steps. The final calculated values represent the *linear* solution of the bioheat equation.

A limitation of the explicit method is that it may not converge to a solution of the actual continuous differential equation. This can occur if the second term of (3.25) is a positive number. This would result in a thermodynamically impossible event since the temperature in the next time-step would be higher than the previous time-step in the absence of a source term. Thus, this means that the second term,

$$T_{i,0}(1 - 2F_o - \frac{w_b c_b \Delta t}{\rho c}) < 0 \tag{3.26}$$

is a necessary requirement. This requirement is called the *Fourier condition* and can be met by choosing appropriate values for the time-step and nodal spacing for the Fourier number, F_o.

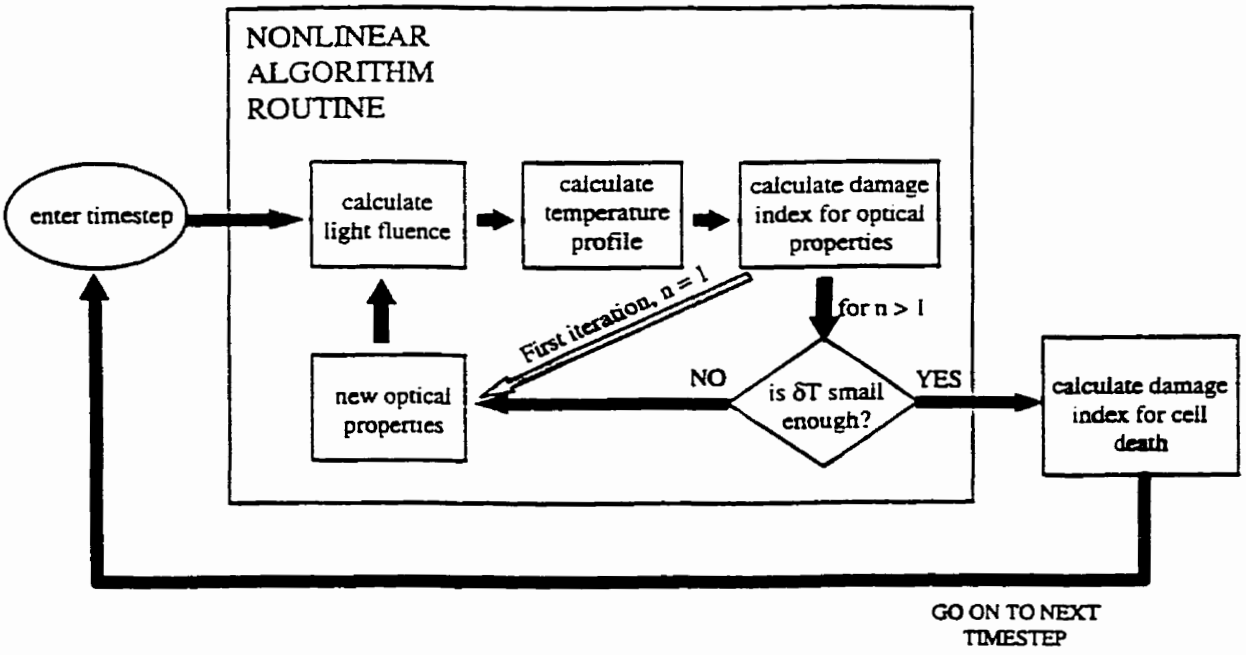

Figure 3.2: Flow chart of nonlinear algorithm used to solve the bioheat equation for dynamic optical properties. n is the number of iterations performed per node and time-step. The number of iterations were usually between 2-4 cycles.

Application of Finite Difference Method to Nonlinear Modeling

For the case of dynamic optical properties, the presence of the temperature dependent term, $P(r,t)$, requires a modified finite difference approach that solves the *nonlinear* bioheat equation [57]. A flow chart of the steps is provided in figure 3.2 which is modified from Kim *et al* [57]. This approach first estimates the temperature by assuming initial (for the first time step) or previous (for all later time-steps) values of the temperature dependent properties. This initial temperature estimate was used to calculate the changes in absorbed light pattern as described in section 3.3.2. The temperature was recalculated with the new conditions and compared with the first temperature estimate. If the difference between the two temperatures was within a tolerance of 0.1% the updated temperature was the stored result, and the program continued to the next time-step. If the difference was larger, the second temperature was assumed to be the best estimate and another temperature comparison was made with the new optical properties values based upon the new best estimate in temperature. The pattern was repeated until the temperature comparison came within tolerance yielding the temperature rise for that time-step. Temperatures were calculated for all subsequent time-steps in the same manner.

Boundary Conditions

Two spatial conditions must be imposed to uniquely solve a second order differential equation. The spatial conditions. called boundary conditions. constrain the solution at positions in space. The first boundary condition was imposed at the fiber edge ($r = r_f$) such that

$$\frac{\partial T}{\partial r}|_{r=r_f} = 0 \tag{3.27}$$

This Neumann boundary condition assumes that there is no conduction into the source. This is equivalent to stating that there is zero energy flow across the fiber tip. The second condition assumes that there is no temperature rise at a distance r sufficiently deep in tissue. This corresponds to a temperature gradient of 0 for large r or mathematically:

$$\frac{\partial T}{\partial r}|_{r\to\infty} = 0 \tag{3.28}$$

The boundary conditions are implemented numerically with finite differences by setting $T_{i+1,j} = T_{i-1,j}$. Therefore. at the fiber edge where $i = 0$. all instances of $T_{i-1,j}$ are substituted with $T_{i+1,j}$. Similarly. deep into tissue. all instances of $T_{i+1,j}$ are substituted with $T_{i-1,j}$.

Computational Resources and Testing

The code for these simulations was developed in the C programming language on a 200 MHz Pentium Pro PC with 384 megabytes of RAM. Typical simulations of 15 minute heating regimes consisted of 500 nodes of 100 μm and 33000 time-steps of 33 ms. The total run time in real time took approximately 10 minutes for linear solutions and 15 minutes for nonlinear solutions. Testing and numerical validation of the model was performed and can be found in appendix C.

3.4 Materials and Methods

3.4.1 Experimental Validation

Model Parameters

The theoretical model (section 3.3) was used to predict temperature rise in the albumen and polyacrylamide phantoms developed in chapter 2. The inputs to the model include thermal and optical properties. The optical properties of the phantom were measured as previously described in section 2.4.1 and are listed in table 2.4. However. the thermal

Phantom	Water content [% by mass]	Heat capacity c $[J \cdot g^{-1} \cdot K^{-1}]$	Conductivity k $[W \cdot K^{-1} \cdot cm^{-1}]$	Density ρ $[g \cdot cm^{-3}]$
Albumen	86.8 ± 1	3.84 ± 0.02	$5.50 \pm 0.08 \times 10^{-3}$	1.04 ± 0.01
Polyacrylamide	85.8 ± 1	3.82 ± 0.02	$5.45 \pm 0.08 \times 10^{-3}$	1.04 ± 0.01

Table 3.1: Thermal Properties of the albumen and polyacrylamide phantoms.

properties of the phantoms were not measured. Thus, the model estimated these values according to approximations of thermal properties based on the water content, W by percent mass [104]. The heat capacity, c, heat conductivity, k, and density, ρ, can be approximated by:

$$c = 4.19(0.37 + 0.63W) \quad [J \cdot g^{-1} \cdot K^{-1}] \tag{3.29}$$

$$k = 4.19(0.133 + 1.36W) \times 10^{-3} \quad [W \cdot K^{-1} \cdot cm^{-1}] \tag{3.30}$$

$$\rho = 1.3 - 0.3W \quad [g \cdot cm^{-3}] \tag{3.31}$$

Table 3.1 lists the thermal properties of the albumen and polyacrylamide phantom according to equations (3.29) through (3.31). The water content of albumen phantom was determined from its composition listed in tables 2.1 and 2.2. For the polyacrylamide phantom, the water content was determined from tables 2.3 and 2.5 which list the composition of the final phantom and the polyacrylamide stock. The thermal properties of water vary as they are being heated [4]. This variation was expected to affect the model predictions. For example, there is 2.5% decrease in density, and a 7.5% increase in conductivity over a temperature range of 20°C to 60°C, while the heat capacity generally remains constant [4]. However, heat also dehydrates tissue resulting in a drop in the percentage of water content. Therefore, the temperature dependence of thermal properties of water are in the opposite direction as dehydration. According to this observation, error ranges, based on the relative variation with temperature, were chosen heuristically to be $\rho \pm 1\%$, $k \pm 1.5\%$ and $c \pm 0.5\%$. These percentages are converted and listed alongside the thermal property values in table 3.1.

The other inputs required for the model include damage parameters and the parameters describing domain and geometry characteristics. The Arrhenius damage parameters due to coagulation of albumen are listed in table 3.2. These damage parameters were determined experimentally by heating the samples at constant temperature and observing the time at which the onset of coagulation occurred through visually inspection [132]. The other physical parameters used in the model are listed in table 3.3. The blood perfusion

Material	$E_a[J/mol]$	A $[/s]$
Albumen [132]	3.845×10^5	3.76×10^{57}

Table 3.2: Arrhenius Damage parameters used for calculating changes in optical properties. The process of coagulation in albumen was based on visual inspection.

Physical parameter	Value
Fiber radius [μm]	750
Spatial domain [cm]	5
Time domain [mins]	15
Node size dr [μm]	100
Time-step size dt [ms]	37
Cool down time [mins]	5
Ambient temperature [°C]	24

Table 3.3: Physical parameters of the program for the polyacrylamide and albumen phantom models. The program continues to calculate thermal damage for a period of time after the laser power was shut off. This is the cool down time.

term w_b was set to 0 when solving the bioheat equation in the phantoms.

Experimental Setup

The phantoms were heated in a plexiglass box with dimensions as shown in figure 3.3. A shortened 14 gauge needle was used to position the source fiber at the centre of a face of the box. The fiber was sufficiently stiff to support its weight horizontally as shown in the figure. With the box empty, a pair of thermocouples, 3.3 mm apart, were pulled taut across the width of the box. The thermocouples were thin (0.0127 mm diameter) T-type (COCO-005, Omega, Stamford, Conneticut). The fiber tip was then positioned 2 mm away from the first thermocouple. This was accomplished by placing the fiber in contact with the closest thermocouple and then retracting it by 2 mm with a micrometer translation stage. The box was filled with the phantom material and solidified, molding to the source and the thermocouples. Once cooled to room temperature, the phantom was heated at constant laser power using the Diomed-15 laser at 805 nm for up to 20 minutes. The laser power setting could be adjusted over a range of 500 mW to 3.5 W. However, due to a loss in power from fiber coupling, the actual power deposited at the fiber tip was determined experimentally to be approximately 60% of the dialed setting. This was measured by using a power meter, and comparing the output of a cut fiber to the isotropic source fiber using an

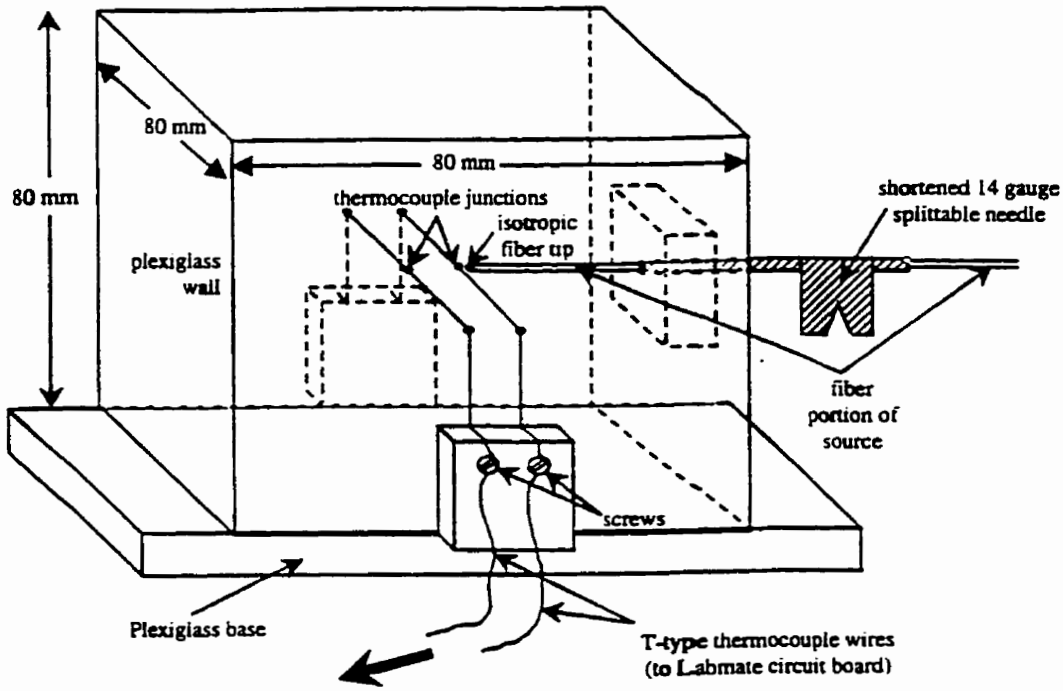

Figure 3.3: Schematic diagram of apparatus used to measured the temperature rise within phantoms.

integrating sphere. Thermocouple readings were recorded every 2 seconds with a Labmate computer system. The polyacrylamide phantom was cooled and re-heated at different laser powers. The albumen phantom was heated only once per phantom preparation. A photograph of the experimental set up is shown in figure 3.4.

3.4.2 A Theoretical Clinical Example: ILP of the Liver

The model was applied to a clinically relevant situation: laser thermal therapy of the liver. Currently ILP of the liver is most often proposed for the palliative care of liver metastasis [112]. Many patients who have metastatic spread to the liver have limited options of treatment. ILP provides a potential method of treating these tumours safely with minimal patient trauma.

Model parameters

The thermal, optical and damage properties of liver were obtained from the literature. The values of are provided in tables 3.4, 3.5, and 3.6 respectively. The other physical parameters used in the model for liver are listed in table 3.7.

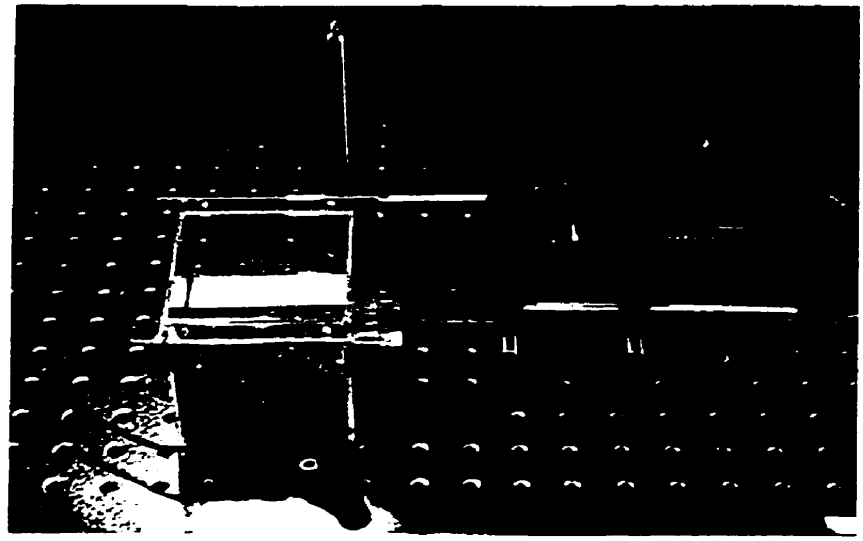

Figure 3.4: Photograph of temperature measurement apparatus: side view.

Thermal Property	Symbol and Units	Value
specific heat	$c\ [J \cdot g^{-1} \cdot {}^{\circ}C^{-1}]$	3.59
density	$\rho\ [g \cdot cm^{-3}]$	1.05
thermal conductivity	$k\ [W \cdot m^{-1} \cdot {}^{\circ}C^{-1}]$	0.00566
volumetric perfusion rate	$w_b\ [g \cdot s^{-1} \cdot cm^{-3}]$	[a]0.0185
specific heat of blood	$c\ [J \cdot kg^{-1} \cdot {}^{\circ}C^{-1}]$	3.84
temperature of blood	$T_{art}\ [{}^{\circ}C]$	37

Table 3.4: Thermal properties of liver [25]. [a]is based upon: $\rho_b = 1.060g \cdot cm^{-3}$ [1] and a blood perfusion rate of $1100mL \cdot min^{-1}Kg^{-1}$ [122].

Optical Property	Native	Coagulated
$\mu_a[cm^-1]$	0.3	0.3
$\mu_s[cm^-1]$	200	530
g	0.95	0.94
$\mu'_s[cm^-1]$	10	31.8
$\mu_{eff}[cm^-1]$	3.05	5.37

Table 3.5: Native and coagulated optical properties of liver [88].

Process	$E_a[J/mol]$	A $[/s]$
Cell Death [11]	5.064×10^5	2.984×10^{80}
Liver Whitening [49]	2.577×10^5	$7.39 \times^{37}$

Table 3.6: Arrhenius Damage parameters used for calculating cell death and changes in optical properties (liver whitening). T_{crit} represents the critical temperature at which the damage index is equal to unity after 10 minutes of heating.

Physical parameter	Value
Fiber radius [μm]	200
Spatial domain [cm]	5
Time domain [mins]	15
Node size dr [μm]	100
Time-step size dt [ms]	33
Cool down time [mins]	5
Ambient temperature [°C]	37

Table 3.7: Physical parameters of the program for the liver model. The program continues to calculate thermal damage for a period of time after the laser power was shut off . This is the cool down time.

3.5 Results

3.5.1 Albumen and Polyacrylamide Phantoms

The model was validated with experimental measurements of temperature rise at a depth of 2 and 5.3 mm away from the fiber tip in albumen and polyacrylamide phantoms. The results of the nonlinear model with changing optical properties were confirmed in the albumen phantom. whereas the polyacrylamide phantom confirmed the linear model for static optical properties.

The temperature rise of the 5.3 mm thermocouple in polyacrylamide is shown in figure 3.5. The error bars of the numerical predictions account for the error on the predicted thermal properties. the measured fiber coupling efficiency ($\pm 0.04W$[1]) and the measured thermocouple positions $r \pm 0.1mm$. The same plot is repeated for the 2 mm thermocouple in figure 3.6. The temperature measurements in polyacrylamide with coagulated optical properties of albumen. compared to the native optical properties. was higher due to a difference in the penetration of light such that more light was absorbed close to the fiber for the coagulated state than the native state. The temperature rise close to the fiber tip

[1]Based upon a standard deviation of 30 repeated measurements of power at 1W

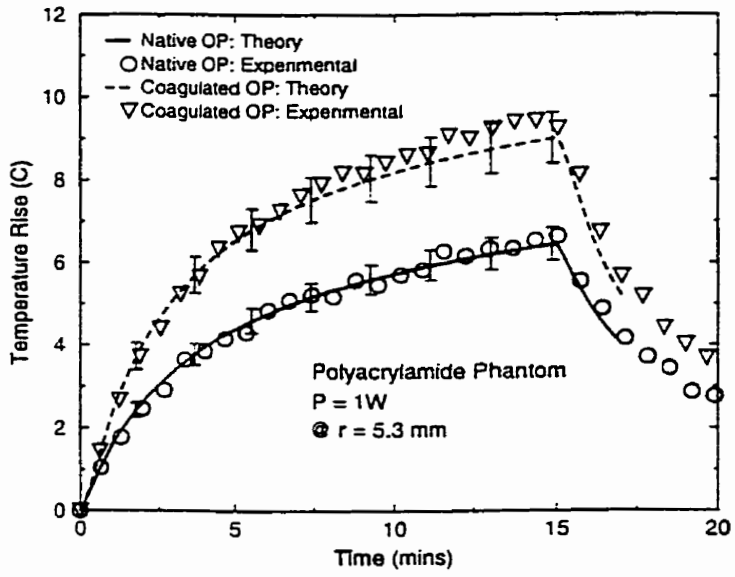

Figure 3.5: Thermocouple probe measurements at r = 5.3 mm with theoretical predictions for polyacrylamide phantom with the optical properties of native (lower curve) and coagulated (upper curve) albumen phantom. (OP: Optical properties)

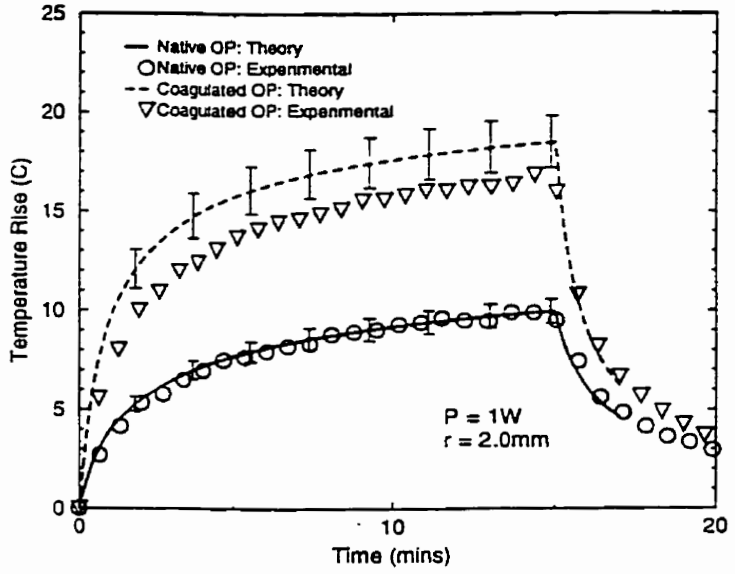

Figure 3.6: Thermocouple probe measurements at r = 2.0 mm with theoretical predictions for polyacrylamide phantom with the optical properties of native (lower curve) and coagulated (upper curve) albumen phantom. (OP: Optical properties)

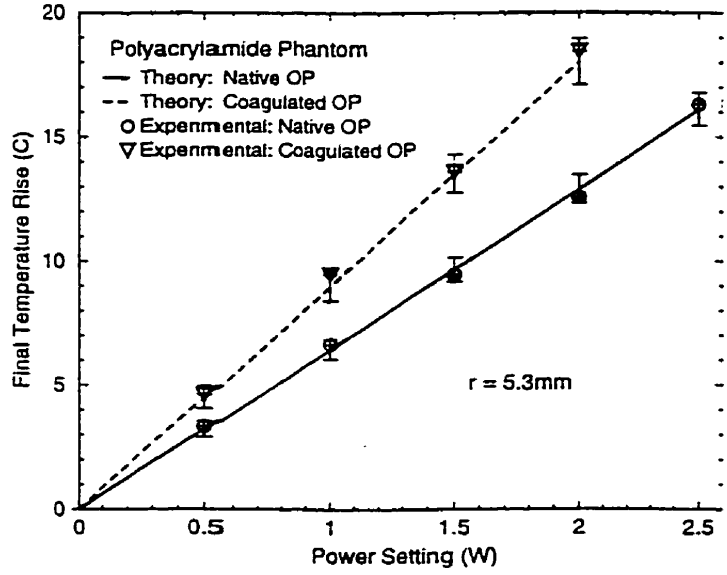

Figure 3.7: Thermocouple probe measurements of final temperature after 15 mins of heating at r = 5.3 mm with theoretical predictions for polyacrylamide phantom with the optical properties of native (lower curve) and coagulated (upper curve) albumen phantom. (OP: Optical Properties)

at the 2 mm thermocouple was greater than the 5 mm thermocouple. This was due to the fluence rate of the isotropic probe which exponentially drops in the radial direction.

A comparison of experimental results with numerical predictions showed that the general shape of the experimental results followed predicted values for both the coagulated and native states at the two thermocouple positions. Absolute values were within the error bars for all curves except for the 2 mm thermocouple measurement in polyacrylamide with coagulated optical properties where the theoretical results overestimated the experimental values by approximately 10 %. This may be due to a positioning error noting that the temperature measurement is most sensitive for this case due to the large thermal gradients (5-10 °Cper mm). Another possible source of error is the conduction effects along the thermocouple which would underestimate the temperature. and thus may partially explain the slightly lower measured values.

Heating of the same polyacrylamide sample was repeated at different powers. The final temperatures after 15 minutes of heating are plotted as a function of power in figures 3.7 and 3.8 for the two thermocouple positions. The final temperatures were proportional to power which were consistent with theoretical expectations. This linearity confirmed that the polyacrylamide phantom was a suitable choice of material to investigate the case

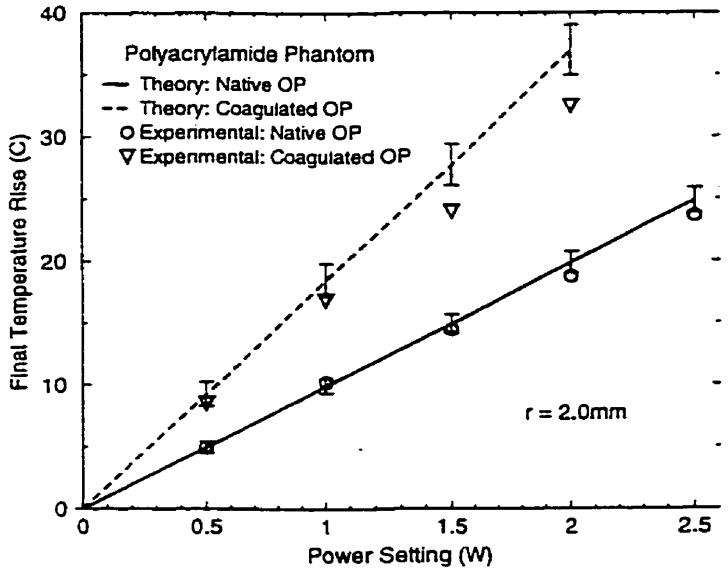

Figure 3.8: Thermocouple probe measurements of final temperature after 15 mins of heating at r = 2.0 mm with theoretical predictions for polyacrylamide phantom with the optical properties of native (lower curve) and coagulated (upper curve) albumen phantom. (OP: Optical Properties)

of static optical properties.

Figure 3.9 plots the experimental temperature rise in the albumen phantom after 19.5 minutes of heating at the two thermocouple locations. The numerical predictions are plotted also at depths of 0 mm, 2 mm and 5.3 mm away from the fiber radius. The most salient feature of the albumen phantom measurements was the sudden increase in temperature at the 2 mm thermocouple which occurred at approximately 10 minutes. According to the model, the sudden increase corresponded to the onset of coagulation which was numerically determined to occur at 9.75 minutes of heating. There was also a similar but very small temperature rise at the 5.3 mm thermocouple which occurred approximately one minute later which is faintly shown by figure 3.9. The delayed increase in temperature at the 5 mm position was a result of thermal conduction. At around 14 minutes of heating the rate of temperature decreases slightly for the 2 mm thermocouple. The slight drop in temperature of the 2 mm thermocouple at 14 minutes, however, deviated from prediction. This may be explained by the presence of high temperatures that may be causing vapourization at the fiber edge as indicated by the top curve of figure 3.9.

Figure 3.10 is a photograph of the final thermal lesion of the albumen phantom. The photograph of the lesion shows a demarcation between coagulated and native albumen.

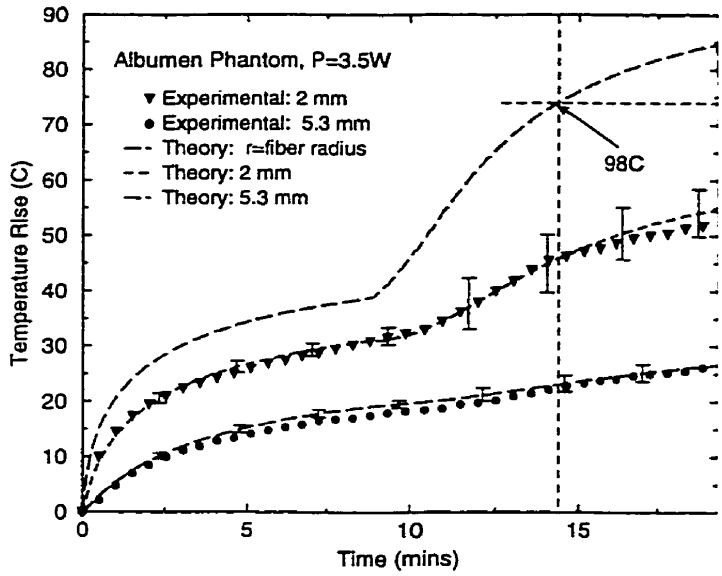

Figure 3.9: Thermocouple probe measurements at r = 2 mm and r = 5.3 mm compared with theoretical predictions at r = 2 mm, r = 5.3 mm and r = r_f for the albumen phantom after 19.5 minutes of heating.

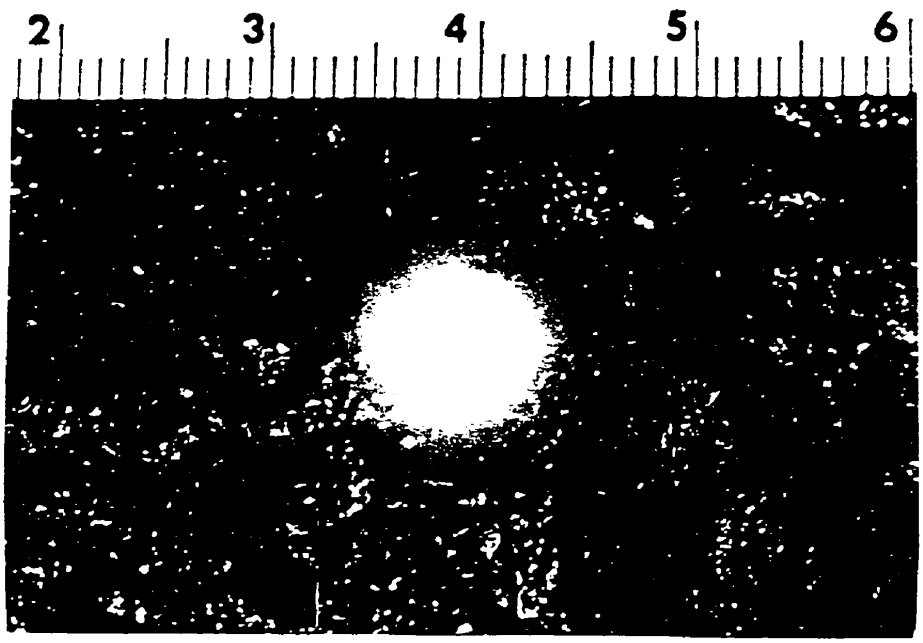

Figure 3.10: Photograph of thermal lesion formed in albumen phantom after 3.5 W at 19.5 minutes: top view. The vertical are the thermocouples positioned at 2 and 5.3 mm away from the source

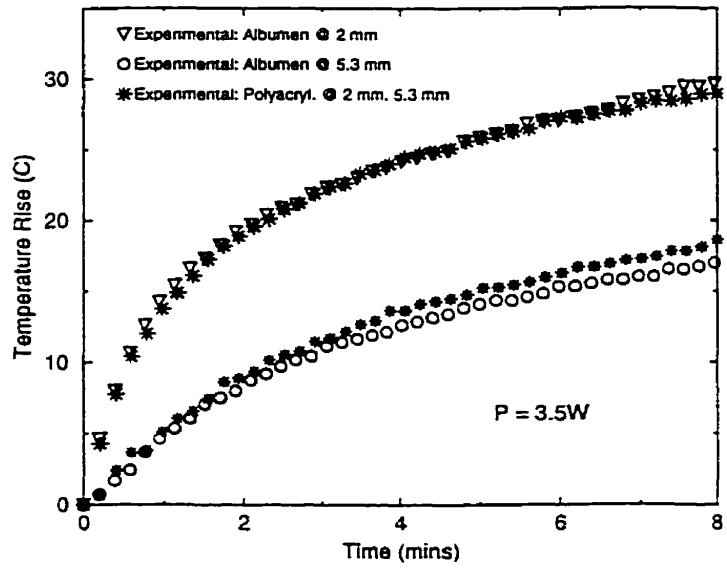

Figure 3.11: Thermocouple probe measurements at r = 2 mm, r = 5.3 mm for polyacrylamide and albumen phantoms.

However, a small transition region of approximately 2-3 mm was seen. The depth of the midpoint of the transition region is approximately 4 mm away from the fiber tip edge when one accounts for the diameter of the fiber applicator. This was 12% greater than the predicted value of 3.45 mm.

Finally figure 3.11 shows the temperature rise for the albumen phantom and for the polyacrylamide with the same optical properties of albumen in the native state. The temperatures were very similar in shape and value for both thermocouple positions. Therefore, this suggests that the optical properties of the albumen phantom were well matched in the polyacrylamide material. This graph also indicates that albumen, prior to the onset of coagulation, behaves in a linear fashion with static optical properties.

3.5.2 ILP of the Liver

The model was applied to a clinically relevant situation of laser thermal therapy in the liver. The simulations were performed by comparing the dynamic effects of changing optical properties to the static case. The therapy was modeled for the situation where the laser power was adjusted such that the peak temperature at the fiber tip was just below vapourization (97°C or 60°C above ambient) at the end of the thermal therapy. Various stages and outputs of the model are examined.

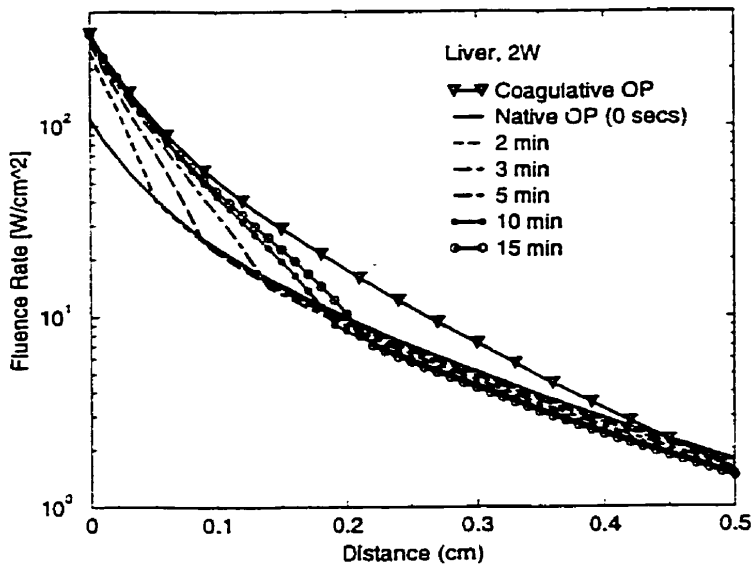

Figure 3.12: Transient changes in fluence rate of liver at 2.0 W.

Fluence Rate Profiles

Figure 3.12 plots the light fluence rate on a log scale as a function of radial distance. The values of the horizontal axis refers to the displacement away from the fiber edge r_f. The penetration of light in the static case of coagulated properties was less than that of the native properties. This was due to the fact that light is more strongly attenuated in coagulated liver than in native liver.

Figure 3.12 also shows the temporal variation of the light fluence rates due to the dynamic effects of coagulation. The dynamic fluence rate curves have slopes that bend sharply at the junction corresponding to the location of the boundary between the two layers. The coagulated regions experienced an increase in scattering and attenuation coefficient. Therefore, the penetration of light was reduced resulting in higher localized fluence close to the fiber tip. The fluence rate gradient fell sharply in the region between the fiber edge and the coagulated boundary. The fall off was more rapid than the coagulated static case as a result of the influence of the native tissue surrounding the coagulated region. This is explained by the reduced contribution of back-scattered light from the native tissues into the coagulated region. This was also demonstrated by the concavity of the fluence rate observed just left of the junction. Beyond the coagulation boundary, the fluence rate slope was similar to that of native liver properties. However, the absolute

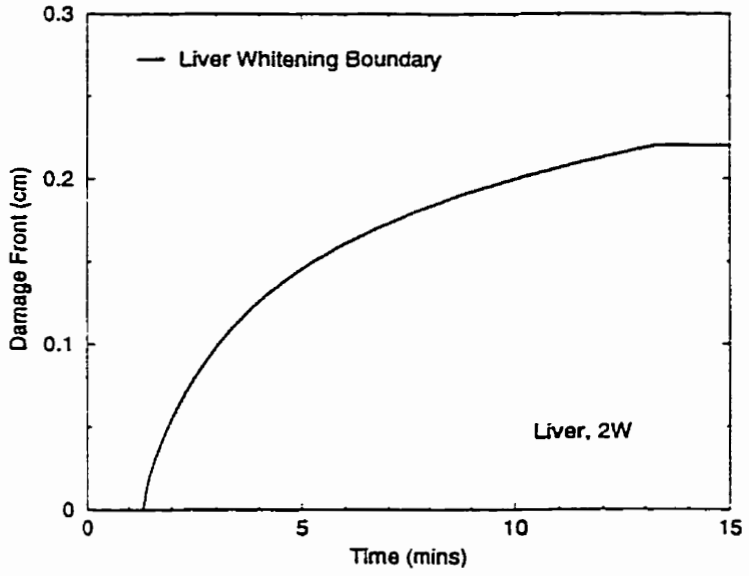

Figure 3.13: Development of coagulation front during heating at 2.0 W.

value was lower since more light photons were lost through absorption upstream, in the coagulated region. As the coagulation front moved deeper into tissue the loss increased due to the growing volume of coagulated tissue which resulted in less light "escaping" into the native tissue.

Figure 3.13 shows the change in depth of the coagulation boundary during the time of heating. Coagulation proceeded from the fiber edge but does not begin until 85 seconds of heating. Initially the velocity of the coagulation front was relatively fast (approximately 0.7 mm/minute) and then slowed after 4-5 minutes (approximately 0.25 mm/minute) as the fluence rate reached steady state. Therefore, the process of dynamic changes in optical properties process approached a final maximum volume of coagulation.

Temperature Rise

Figure 3.14 shows the peak temperature rise at the location of the fiber edge, r_f. Coagulated tissue absorbed more light close to the fiber tip, than native tissue resulting in a higher peak temperature. This was due to the increased probability of scattering in the coagulated tissue which shortened the photon path length. Therefore less laser power (1.84W) was required to heat coagulated tissue to the same peak temperature as native tissue (3.88W). The dynamic case required lower power than constant native optical prop-

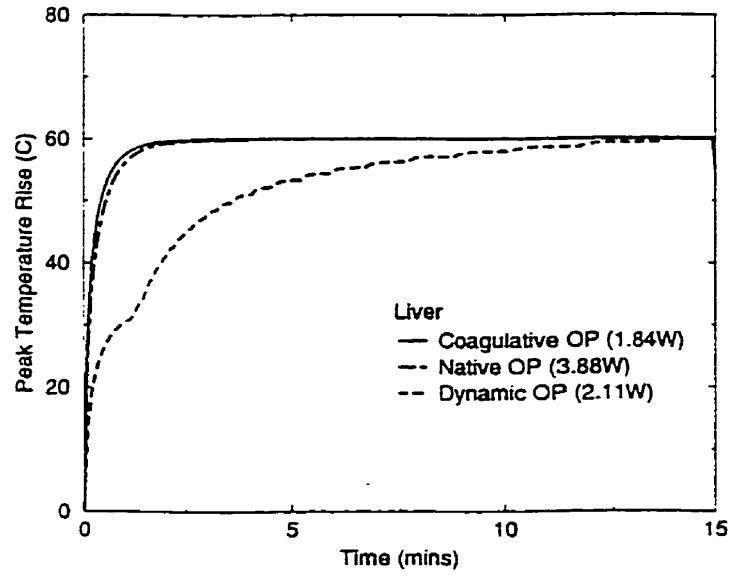

Figure 3.14: Effect of changing optical properties on temperature rise. The powers are adjusted so that the peak temperature is 60°C above ambient for all cases.

erties and a higher power than coagulated optical properties (2.11W). This was expected since the dynamic model contains regions of coagulated optical properties and native optical properties.

For the static case, the rate of temperature rise for the denatured and native optical properties did not differ greatly compared with the dynamic model. In the dynamic model, the tissue initially possessed native optical properties. However, its rate of temperature rise was slower than that of the native static case because of its lower laser power (2.11W versus 3.88W). The temperature rise decelerated and approached steady state. However, at approximately 1 minute, the onset of coagulation caused a sudden increase in the rate of temperature rise. The increase was a product of the elevation of fluence rate close to the fiber tip due to the onset of coagulation as demonstrated in figure 3.12. This effect was similarly observed experimentally in the albumen phantom (see figure 3.9).

The temperature profile at the end of the 15 minute therapy is plotted in figure 3.15. The temperature distribution of native liver, extended deeper into tissue than the coagulated and dynamic models. This correlates with the ability of light to penetrate into tissue according to the attenuation coefficient of each state. For the case of dynamic optical properties, the temperature gradient close to the fiber tip was larger than the static model cases. Whereas further away from the tip ($\sim$ 2 mm), the temperature profile of the

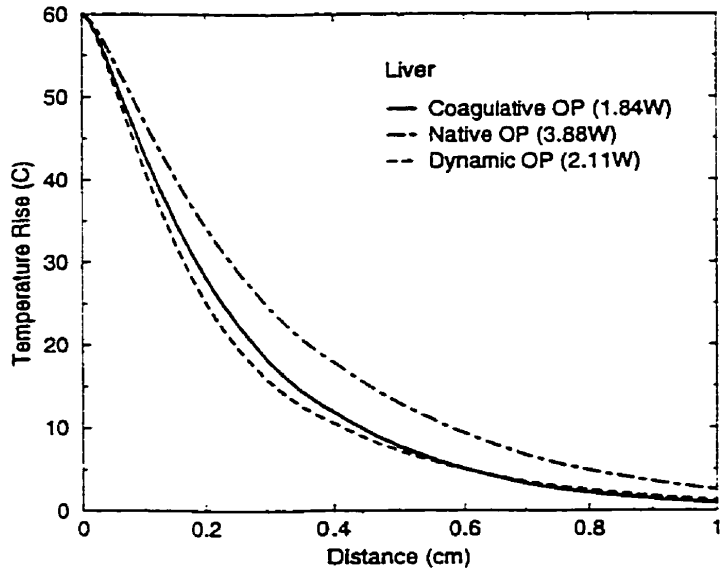

Figure 3.15: Effect of changing optical properties on temperature profile.

dynamic model was more gradual than the static cases. This was a consequence of the fluence profile (figure 3.12) which showed that the fluence rate was steep in the coagulated regions and more shallow in the native tissue.

Damage front

Figure 3.16 shows the effect of dynamic modeling on the prediction of thermal damage leading to cell death where the Arrhenius damage index, Ω, is unity. The static model for native optical properties predicted the greatest depth of cell damage of 7 mm. The static model for coagulated properties gave a lower prediction of 5.3 mm. Hence, native optical properties predicts a lesion which is 130 % greater in volume than that predicted for coagulated optical properties. The propagation of the damage front for the dynamic case started slightly later in time. After the onset of coagulation, however, the rate increased until the final depth was virtually equal to that for static coagulated optical properties.

3.6 Discussion

Heating of biological media induces changes in optical properties which then influence the light distribution within the media. This in turn may affect the temperature rise. Thermal models of ILP have been previously developed in the literature which attempt

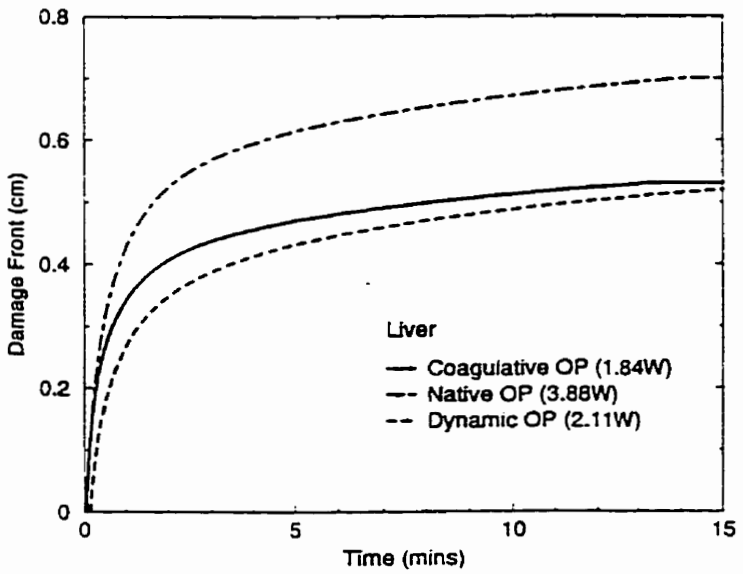

Figure 3.16: Effect of changing optical properties on damage front.

to account for the effects of changes in optical properties on temperature rise [57,84,125]. Many investigators have assumed that these dynamic effects can be quantified using an Arrhenius damage model where temperature rise is related to a rate process describing the heat induced changes in optical properties in tissue [57,84]. However, this assumption has not been experimentally verified. Therefore, it is important to test this fundamental assumption which is the crucial mathematical link between the changes in light fluence and temperature rise.

We have developed a nonlinear model which incorporates the Arrhenius damage formulation to describe dynamic changes in optical properties during heating. This was performed by using an analytical solution of the diffusion approximation. The analytical solution assumed that coagulated tissue can be represented as a two layer system where the inner layer surrounding the fiber tip possesses coagulated optical properties and the outer second layer possesses native properties. The use of the two layer solution requires few mathematical operations to define the spatial distribution of light fluence. This is less computationally exhaustive than using numerical methods which must discretize and solve the diffusion equation over the entire domain [37,57].

However, a limitation of diffusion theory is that the accuracy close to the source and to tissue boundaries [44,90] is poor. This suggests that the peak temperature prediction at the fiber edge in our simulations may be inaccurate. However, Roggan *et al* demonstrated

that diffusion theory agrees well with Monte Carlo predictions for radial distances greater than the radius of the interstitial applicator [90]. Hence, the diffusion approximation can be effectively used to predict light fluence for practical distances away from the light source. Another problem of the light diffusion approximation is that it may not be suitable for use in tissue with a relatively low scattering coefficient. This may be the case, for example, when modeling light fluence in the cerebral spinal fluid of the brain since it has a very low scattering coefficient [44]. However, for the majority of tissues, the diffusion approximation has been successfully used in various laser irradiation applications [38, 72, 81].

The two layer solution of the diffusion equation, when coupled to the bioheat equation, predicted a significantly different course of temperature rise than the static case. The dynamic model indicated that the rate of temperature rise would suddenly increase at the onset of coagulation at the fiber tip. The sudden increase is due to the reduced penetration depth of light within the newly coagulated region resulting in a rapid increase in local absorption. This temperature elevation is then conducted away to deeper regions of tissue.

The theoretical model was experimentally verified in opto-thermal phantoms consisting of albumen and polyacrylamide. To the author's knowledge, this is the first set of experimental evidence which has validated the use of the Arrhenius damage model to describe the effects of changes in optical properties during laser irradiation. Temperature measurements were obtained at distances of 2 and 5.3 mm away from the fiber tip using thin thermocouples. Positioning of the thermocouples was chosen to be as close to the fiber tip as possible where the effects of coagulation could be observed while attempting to avoid excessive self heating of the thermocouple and perturbation of the light field. Self-heating is caused by the local absorption of the light fluence by the thermocouple. Temperature measurements close to the fiber tip were sensitive to positional errors due to large thermal gradients (5-10 °Cper mm) in this region. Nonetheless, the rapid elevation in temperature that was observed by the 2 mm thermocouple agreed well with theoretical predictions. A similar but less pronounced effect at the 5.3 mm thermocouple was observed due to thermal conduction. The final diameter of thermal lesion in the albumen phantom was approximately 8 mm. This was 12% greater than the predicted value of 6.9 mm. This discrepancy may be due to the inability to clearly perceive the visual contrast between coagulated and native regions. This applies for both the experiment measurements in our albumen phantom and in the original literature measurements from which the damage parameters of albumen were derived [132].

The measurements were repeated in the polyacrylamide phantom whose optical

properties do not change with temperature. The polyacrylamide results also agreed well with predicted values. The experimental measurements indicate that the temperature rise in the polyacrylamide phantom was proportional to the laser power and hence accurately represented the linear static case. These findings were compared with the albumen results. The comparison indicated that the rate of temperature rise in the polyacrylamide phantom is the same as the albumen phantom prior to coagulation. After the onset of coagulation, the sudden increase in temperature rise which was observed in the albumen phantom was not present in the polyacrylamide phantom measurements. This suggests that the observed differences between the two phantoms can be attributed to changes in optical properties.

The theoretical significance of dynamic optical properties was investigated in a clinical application of ILP of the liver. These simulations examined the influence of coagulation on fluence, temperature and damage predictions by comparing the dynamic model to the static case. The power was adjusted such that the peak temperature was below vapourization at the end of the treatment period. We thought this was an important clinical consideration in order to avoid vapourization and charring of the fiber tip.

The fluence rate profiles in liver for the dynamic case produced large light fluence gradients within the coagulated region close to the fiber tip. This demonstrates that light penetration is reduced in the coagulated regions. The gradient, however, was less sharp in the native regions deeper into tissue. The dynamic changes in light fluence resulted in a sudden increase in temperature rise at the onset of coagulation in liver which was also seen in the albumen phantom experiments. A similar sudden temperature rise has been theoretically predicted for short irradiation times at high powers [84] for myocardium. However, this effect was not observed by several other laser irradiation studies which account for changes in optical properties using the Arrhenius damage relationship [37, 57, 90]. The reason for this may be due to their difference in geometry and applicator devices [37, 57].

The predicted final damage volume was only slightly less than that predicted for constant coagulated optical properties. Therefore, the static model with coagulated optical properties may be proposed as a method of approximating the effects of the more complex dynamic case in terms of damage. However, this may be an oversimplification in terms of predicting accurate temperature profiles and determining the necessary power levels.

It is important to include the dynamic effects of changing optical properties in thermal models for several reasons. First, the dynamic changes in optical properties have the largest impact on temperature predictions close to the fiber tip. Therefore dynamic models may be used to ensure that vapourization at the fiber applicator has been avoided

successfully. Secondly, the changes in light fluence or the sudden increase in the rate of temperature rise due to the onset of coagulation may provide additional information during the treatment. For example, they may be used as markers indicating the depth of the coagulation front as a feedback parameter during the treatment. Finally, the theoretical model improves our understanding of the significance of changing optical properties during thermal lesion formation. This information may be essential during treatment planning when customizing treatments based on tissue type which have varying degrees of changes in μ_a and μ_s' due to heat.

3.7 Conclusions

A nonlinear mathematical model was developed which uses the Arrhenius damage formulation to to account for the effects of heat induced changes in optical properties. Experimental validation was performed by measuring temperature rise in albumen and polyacrylamide phantoms and comparing them with predicted values. The model agreed well with experimental measurements of temperature in the albumen phantom demonstrating that the Arrhenius formulation can be used in opto-thermal models to accurately predict the effects of changes in optical properties. The results indicate that changes in optical properties cause an increase in the fluence gradients within the coagulated region of tissue surrounding the fiber tip. This is a consequence of reduced light penetration in this region which then results in increased absorption of light energy. The local absorption induces the temperature to rise which is manifested as a sudden increase in peak temperature rise at the onset of coagulation. The rapid elevation in temperature due to the dynamic changes in optical properties, has the largest impact on peak temperature predictions close to the fiber tip. However, this temperature rise is also seen in deeper regions of tissue as a result of thermal conduction. This information may be important in order to avoid using excessive powers which may induce vapourization and charring. The final damage volume is very similar to static predictions with coagulated optical properties. However, the laser power requirements are considerably different between the dynamic and static models. In general, the results suggest that the features of lesion formation are highly dynamic due to the coagulation effects. This validates the need for theoretical investigations to account for the effects of changing optical properties in models of ILP.

Chapter 4

Conclusion and Future work

4.1 Summary and Conclusions

The goal of this thesis is to investigate the theoretical and experimental effects of changing optical properties on fluence temperature and damage during interstitial laser photocoagulation. Investigations began with the development of two phantom designs to simulate the response of tissue to heat during thermal therapy with lasers. Albumen was chosen as a base material to demonstrate the transient effects of coagulation during heating. The optical properties of the albumen phantom in its native and coagulated states, were measured using the poison moderator technique. A second phantom, based on polyacrylamide. was produced to examine the static case where optical properties do not change. This was performed to provide a basis of comparison with the albumen phantom results. Polyacrylamide phantoms were constructed successfully with optical properties that matched those of the albumen in both its native and denatured states.

A nonlinear mathematical model was developed that quantifies the effects of changing optical properties on fluence, temperature and damage predictions. Temperature rise in tissue was estimated using the bioheat equation and solved with a nonlinear algorithm using the finite difference method (FDM). Light propagation was calculated from the analytical solution of the light diffusion approximation. Dynamic changes in optical properties due to the onset of coagulation were handled by solving the two layer analytical solution of the diffusion approximation. The depth of coagulation was determined from the Arrhenius damage integral yielding the change in optical properties as a function of depth and time. Calculations of the damage index corresponding to the process of cell death resulted in an estimate of the overall extent of the thermal damage. Experimental validation was

performed by measuring temperature rise in the albumen and polyacrylamide phantoms and comparing them with predicted values.

The work presented in this thesis contributes to two areas of laser thermal therapy. First, the phantoms were developed and characterized successfully and thus they can be used readily for future investigations of ILP. The albumen material is highly suitable for tissue studies that account for changing optical properties. In contrast, polyacrylamide maintains its optical properties during ILP and therefore it can be used to study heat transport for static conditions. The experimental work also demonstrates the applicability of the diffusion approximation for the theoretical calculation of light propagation in these phantoms as shown by the straight line experimental fit of the fluence to diffusion theory models.

The second area of contribution is the development of a nonlinear thermal model to examine the effects of changing optical properties during ILP. Recently, there have been attempts to model dynamic changes in tissue properties during thermal therapy with lasers [57, 84, 125]. Many models complicate the issue by including multiple factors that affect lesion formation simultaneously. For example, they may include effects of both dynamic changes in blood perfusion and optical properties [9, 37, 49, 57, 62, 89]. As such, the main dynamic assumptions of the nonlinear model cannot be easily validated. In this thesis, we have been able to simplify, isolate and confirm the effects of dynamic optical properties using the most basic of assumptions to describe the light source and tissue geometry. Furthermore, the experimental results were achieved in a controlled reproducible experimental environment. These experimental results agreed well with theory, which supports the use of Arrhenius damage formulation to describe dynamic changes of tissue properties. Although often employed in the past, the Arrhenius formulation to describe the nonlinear effects of changes in optical properties has only been speculative up until now.

The nonlinear model developed in this thesis also provided many insights into the formation of thermal lesion. For example, our theoretical and experimental results indicate that coagulation causes a sudden increase in the rate of temperature rise due to a decrease in light penetration within the coagulated region close to the light source. A smaller and slightly delayed rise in temperature is observed deeper into tissue which is due to the effects of thermal conduction. Prior to coagulation, however, the rate of temperature rise is the same as the static case of native optical properties. The significance of these findings were also investigated in a clinically relevant situation: ILP of the liver.

The liver simulations were conducted with a constant laser power such that the

peak temperature was just below vapourization at the end of the 15 minute irradiation time. This reflects the situation where vapourization and charring are avoided. The model predicted that changes in optical properties cause larger fluence gradients in the coagulated region of tissue surrounding the fiber tip than in the uncoagulated tissue. Again, this is a result of the elevation in scattering coefficient of denatured tissue causing the light penetration to be diminished in that region. As heating progressed, the volume and depth of coagulation increased such that the rate of propagation of the coagulation front is initially fast and then approached steady state.

A sudden increase in temperature rise was observed at the onset of coagulation in a fashion similar to that observed in the albumen phantom. This event has been given minimal theoretical attention in the literature [125]. However, we feel that this is an important observation in order to successfully ensure that vapourization at the fiber applicator has been avoided. Furthermore, the sudden change in temperature due to coagulation may provide additional information during the treatment as a feedback parameter. For example, the onset of coagulation can be used a marker flagging that coagulation has been initiated. This signal could then be used to lower the light power such that high peak temperature are avoided.

The results were compared with the case of static optical properties and showed that the dynamic case produced larger temperature gradients within the coagulated region than the static case. The dynamic model, however, predicted smaller temperature gradients than the static case for deeper native region of tissue. This resulted in a final damage volume that was approximately the same as that predicted by the static case of coagulated optical properties. This suggests that the simpler static model with coagulated optical properties may be used instead of the nonlinear model to predict final damage outcome. However, the laser power requirements are considerably different between the two models. As well, the thermal histories also significantly differ. In theory, however, if one could calibrate for the power requirements, and is unconcerned about measuring temperatures, a static model may possibly be sufficient. The more likely scenario, however, is that a dynamic nonlinear model would be desirable to provide the greatest amount of information about the dynamic nature of the coagulation process. In this light, the investigations of this thesis validates the need for theoretical investigations to account for the effects of changing optical properties in models of ILP.

4.2 Future Work and Preliminary Results

This work has focused on mathematical models to predict temperature distributions that account for the transient effects of changes in optical properties. This is an important step for developing accurate thermal models to facilitate treatment planning and feedback systems during interstitial laser photocoagulation. However, much more development of the current model is required before accurate *in vivo* thermal predictions can be performed. In general, developments of the numerical methods should include more realistic aspects of current and future applications of interstitial laser photocoagulation. The preliminary work presented in this chapter focuses on these issues.

Dynamic Changes in Blood Perfusion

Clinical and animal studies have shown that blood flow has a dramatic effect on the efficiency of heating with ILP *in-vivo* [19]. Initially, blood flow has been found to increase due to vasodilation as an inflammatory response to heat [57]. If the temperature is increased above approximately 41°C blood flow decreases until complete stasis occurs [87, 92].

Hence, the model was expanded to include the dynamic effects of blood perfusion using the Arrhenius damage integral. Blood perfusion w_b, is calculated using experimentally derived damage parameters, A_b and E_a, that describe the process of vascular collapse due to heat [16] such that

$$w_b(r,t) = w_{b_{max}}(1 - e^{-\Omega_b}) = w_{b_{max}}(1 - e^{-\int_0^t A_b \cdot e^{-\frac{E_b}{RT(r,t)}}\, dt}) \tag{4.1}$$

This relationship was heuristically formulated such that the blood perfusion, w_b is its maximum value, $w_{b_{max}}$ when Ω_b is 0 (no thermal damage) and the blood perfusion is equal to 0 when Ω_b is at its maximum value of 1 (complete thermal damage). Preliminary results were performed for the case of liver with the same tissue properties listed in tables 3.4, 3.5, and 3.6[1]. The temperature calculations are presented in figures 4.1 and 4.2. The plots suggest that the temperature predictions for dynamic blood perfusion close to the fiber tip, are in between the two extreme cases: complete hemostasis (w_b=0) and constant maximum perfusion (w_b=$w_{b_{max}}$). Deeper into tissue, however, the temperature profile of the dynamic case resembles that of constant perfusion where temperatures are low and hence where perfusion is preserved. Since the temperature in this region is close to the critical temperature at which vascular collapse occurs, the final lethal damage depth of

[1] All subsequent plots in this section have been performed with the same parameters

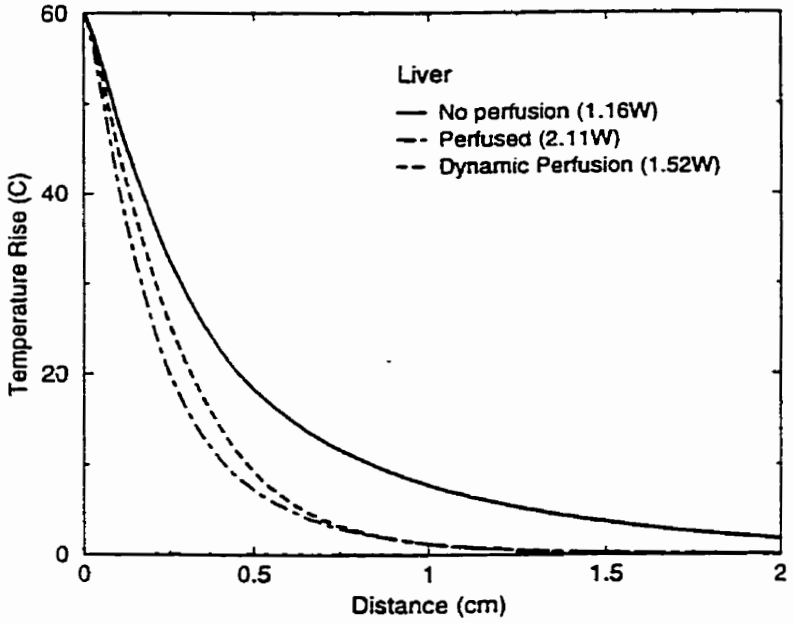

Figure 4.1: Temperature profile demonstrating effects of dynamic blood perfusion. Treatment time: 15 minutes calculated with dynamic optical properties. Temperature at the fiber tip was controlled to be just beneath the vapourization threshold (97°C).

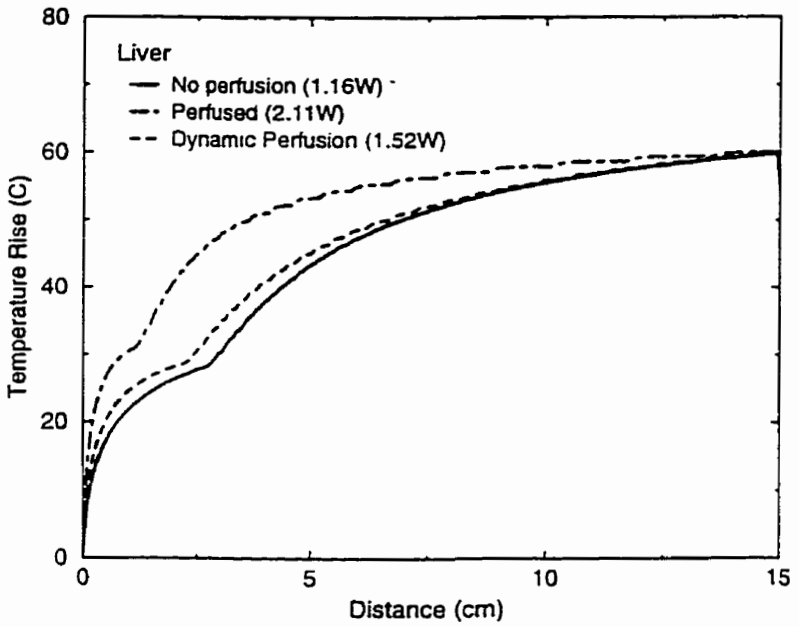

Figure 4.2: Temperature rise as a function of radial distance away from the fiber tip.

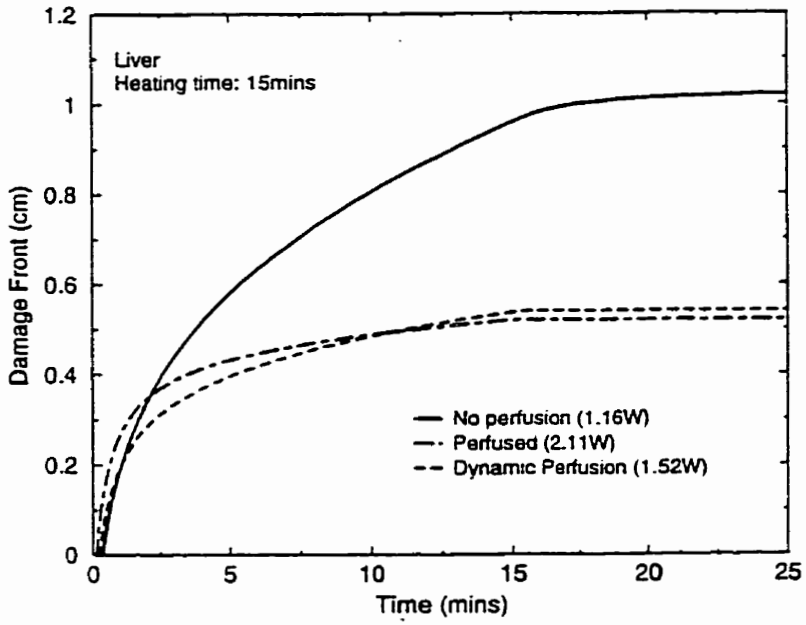

Figure 4.3: Development of the cell death damage front. The damage plot is extended to 25 minutes, since damage may continue to accumulate after the laser power is shut off.

the dynamic model is approximately the same as the static perfused case (see figure 4.3). Also note that perfusion acts as a heat sink. Therefore, the greatest amount of energy is required to heat constantly perfused tissue. The non-perfused case requires the least power and as expected the power required in dynamic model is between the two extreme cases. Therefore, this suggests that dynamic changes in perfusion also affect thermal and damage predictions.

Interstitial Applicators

The numerical model can be further modified to simulate more realistic interstitial applicators. Currently an isotropic source was modeled in spherical coordinates in the axial direction. However, most applicators radiate along some length in order to produce a larger lesion. An example is a cylindrical diffusing tip [90]. Therefore, it is recommended that the model be expanded to two or three dimensions to simulate more practical fiber delivery systems.

A recent development of fiber delivery systems is to cool the fiber tip with fluids using thin interstitial catheter jackets [90, 100]. Cooling reduces the peak temperature at the fiber tip which results in a displacement of the peak temperature at some depth

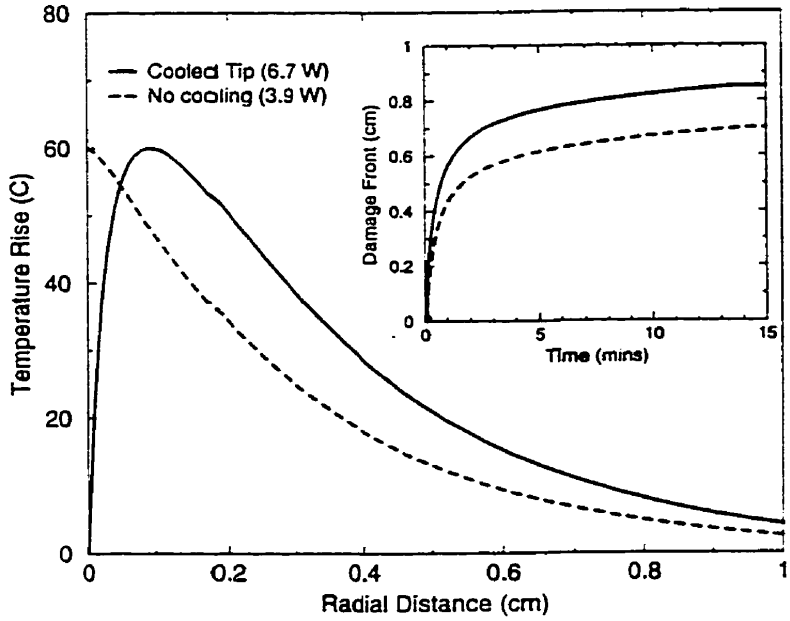

Figure 4.4: The effects of cooling on temperature profile. The resultant damage front depths are shown in the inset graph. Constant native optical properties are used.

in tissue (see figure 4.4). Cooling also requires higher laser powers to achieve the same peak temperature as the non-cooled case. This delivery system has been shown to produce deeper heating of the tissue [74, 90, 100]. The effects of dynamic optical properties on cooled fiber applicators has not been studied thus far in the literature. This cannot be performed with the model developed in this thesis since cooling would require that the analytical solution of the diffusion equation be expanded to three layers. This is because cooling would cause coagulation at some depth away from the source, resulting in three layers of differing optical properties, namely 1) an inner layer of native tissue at the cooled fiber tip surrounded by 2) a ring of denatured tissue, and 3) a third region of native tissue. Analytical solutions of light propagation for this situation may exist theoretically, however, solving the light diffusion approximation numerically may be a more practical route. A finite difference solution of the light diffusion approximation can be found in [119]. This preliminary evidence demonstrates that cooling of the fiber tip will produce larger lesions. However, the effects of cooling require more sophisticated numerical methods to describe light propagation due to the complexity of the layers of differing optical properties.

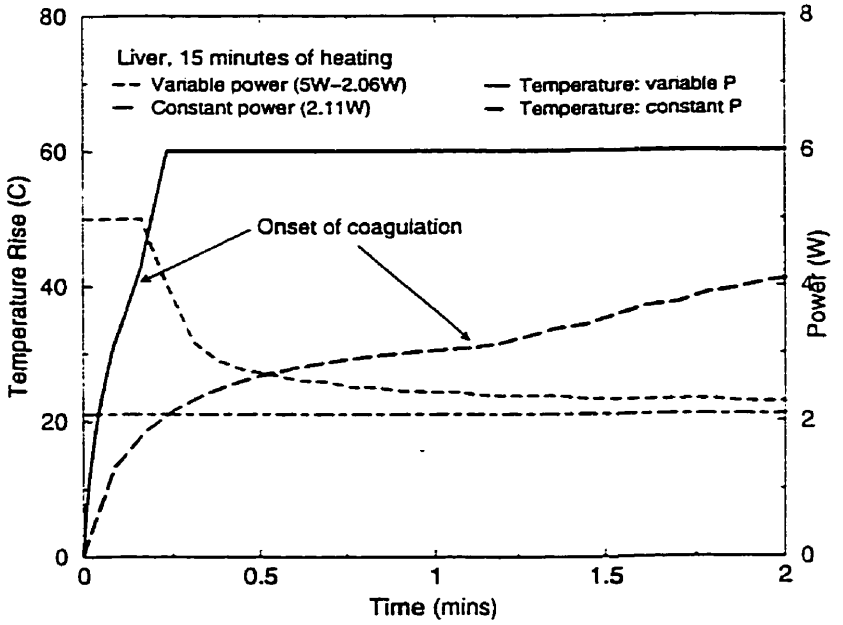

Figure 4.5: Variable power with time and resultant rise in peak temperature at the applicator radius. Total treatment time: 15 minutes calculated with dynamic optical properties.

Variable Laser Power with Time

Another trend of thermotherapy with lasers is to vary the laser power with time in order to produce the most efficient means of deposition of energy in tissue. Our preliminary efforts in this area show that the power could be varied to produce an immediate rise in peak temperature. The temperature can then be held at a maximum limit below vapourization thresholds. The power required as a function of time is determined by rearranging the bio-heat equation and solving for the energy source at each time-step. The resultant power and peak temperature rise is demonstrated in figure 4.5. Varying the power with time causes the temperature to rise at a much faster rate than when constant power is used. Consequently, coagulation occurs at an earlier point in time which may mitigate the convective effects of blood perfusion by inducing vascular collapse. Our results suggest that variable power may improve heating time since the coagulation occurs at a faster rate for variable than constant power (refer to figure 4.6. However, the ultimate difference in the size of the thermal lesion for the same peak temperature may be the same as demonstrated by the final damage front of figure 4.6. Therefore, variable power may be an effective method of reducing the therapy time, but does not increase the size of thermal lesions.

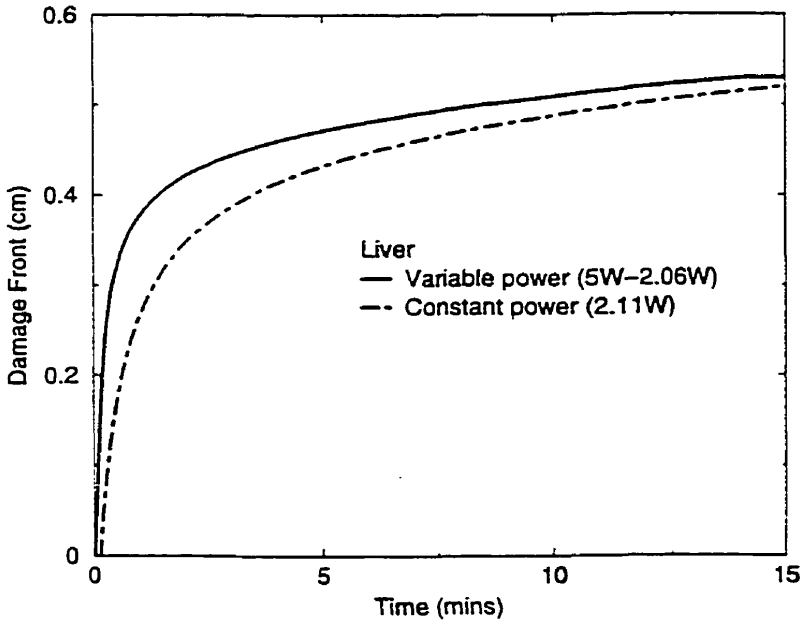

Figure 4.6: Damage front demonstrating the effects of variable power. Total treatment time: 15 minutes calculated with dynamic optical properties.

Measurement of Dynamic Changes in Fluence

Finally, the measurement of light fluence may also be a potential feedback parameter during on-line monitoring of damage. Light fluence can be detected by interstitially inserting dosimetry probes in close proximity to the fiber source. This provides measurements of the transient changes of fluence rate during the treatment time at a fixed position within the tumour. The potential use of this measurement is briefly investigated using the nonlinear model presented in this thesis. The results are as follows.

The normalized fluence rate as a function of time in liver is shown in figure 4.7. Light fluence is calculated at several points in space away from the fiber applicator radius. Initially, the fluence is constant for all depths. After 1 minute of heating, the onset of coagulation is observed as a sudden $\simeq$ 2.5 fold increase in fluence at the location of the applicator radius (r = 0 mm) at point A. This rise is attributed to the increase in scattering and attenuation coefficient that occurs when liver is denatured. The coagulated region reduces the penetration of light resulting in higher localized fluence values. Consequently, the other dosimetry probes experience a slight decrease in fluence rate since less photons are able to penetrate into deeper regions. The fluence rate decreases for each probe until the coagulation front passes beyond the depth of the individual probe (e.g. point B for the

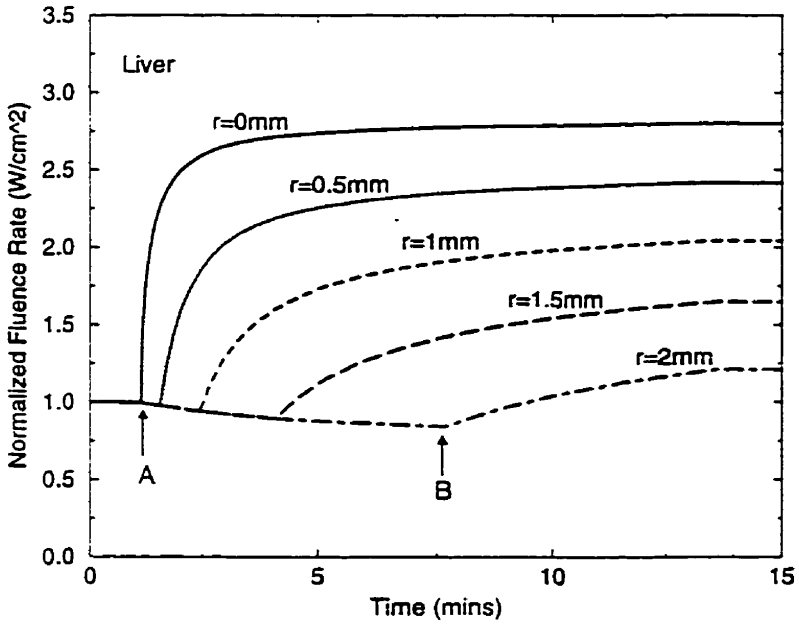

Figure 4.7: Normalized fluence at various depths in tissue during photocoagulation of liver at 2.11W

2 mm probe). Upon passing the location of the probe, the fluence rate rises in a similar fashion as described for point A, but at progressively lower rates for increasing depths.

This study suggests that changes in light distribution due to heat can be monitored by a single probe to provide two temporal pieces of information: the time of onset of coagulation at the source location (arrow A) and the time when the coagulation front passes beyond the location of the probe (e.g. arrow B for the 2 mm probe). The first piece of information signifies that the peak temperature at the fiber tip has risen beyond the coagulation threshold. This could be used as a warning signal for the avoidance of vapourization and charring. The second temporal feature, marked by a sudden rise in fluence, indicates that the coagulation front has reached the depth of the detector probe which provides a means of determining directly that coagulation and hence lethal injury has occurred at that depth. This may be an improvement over using thermocouple measurements which uses an indirect means of detecting coagulation or thermal damage.

There are some obvious problems of using dosimetry probes in this fashion. First, it is difficult to place the probes at accurate distances away from the probe. This problem, however, is true for any invasive measurement technique. Furthermore, there is a limited distance that the probe can be placed from the source and still provide useful information. One reason for the limitation being that, after a certain depth, the coagulation front will

never pass beyond the probe. Another reason is that the fluence rate may be undetectably small in deeper regions. Finally, the probes themselves perturb the light field which may cause shadows behind the probes and thus inadequate and non-uniform heating.

Some of these limitations could be circumvented with the use of smaller probes or more sensitive detection methods. However, a thorough investigation must be performed before any conclusions can be drawn. Future studies should be directed ideally toward the potential of using fluence measurements as a potential feedback parameter for the dynamic control of the heating source during ILP.

Appendix A

Dosimetry Probe Design

A.1 Construction

To measure the light fluence rate, an isotropic dosimetry probe with a scattering spherical tip was constructed. The dosimetry probe was constructed from a 600 μm plane cut end fiber with an SMA 905 connector. The polished, cut end of the fiber was embedded to a depth of $\simeq 3$ mm into a mixture of titanium dioxide particles (TiPure, C35R4, Dupont, Wilmington, Delaware) and epoxy, which cures under ultraviolet (UV) light (J91 Epoxy, Summerslab Co.). The fiber was coupled via lens to a helium cadmium laser which emits in the ultraviolet range. Using low laser power, the light propagated down the fiber and was deposited into the epoxy mixture from the cut end of the fiber. In the presence of the scattering material, the cut end radiates in a quasi-isotropic fashion [130]. Therefore, the epoxy cures in a spherically symmetric fashion around the fiber tip. After four hours of irradiation, the cured cut end was removed from the epoxy mixture. The outside of the tip was then placed under a UV lamp for an additional two hours.

A.2 Characterization

The isotropy of the dosimetry probe was measured by irradiating the tip externally with collimated laser light beam from an 805 nm laser diode (Diomed-15, Diomed Ltd., Cambridge, UK). The light entering the dosimetry probe was detected at the SMA fiber end. The fluence was measured as a function of radial angle by rotating the collimated beam around the probe in the plane parallel to the axis of the fiber.

The normalized polar plot of the detected fluence from a collimated beam as a function of angle in the plane parallel to the axis of the fiber is shown in figure A.1.

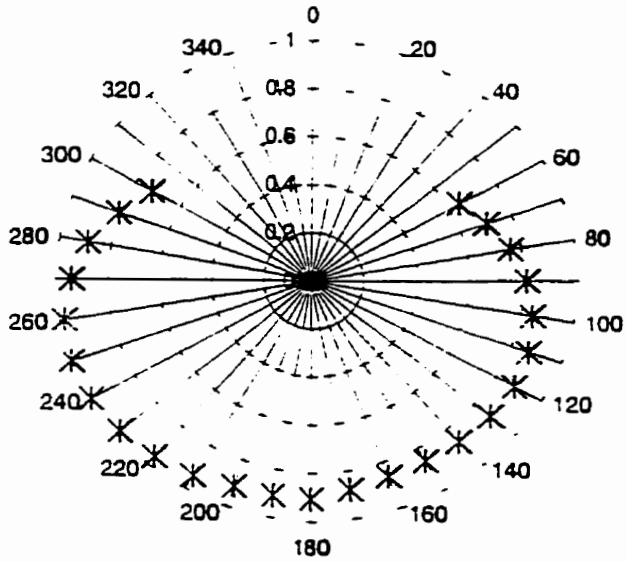

Figure A.1: Normalized detected fluence of dosimetry probe. Irradiation by an external collimated beam. The probe faces forward at 180°.

The detected fluence rate drops at acute angles of less than 90° and greater than 270°. This probe is thus less sensitive to fluence from the backward scattering direction. The effect may be a result of the presence of excess epoxy that remained due to surface tension on the sides of the cut end fiber after it was removed from the epoxy mixture. The anisotropy would result in greater sensitivity to collimated and forward scattered light than diffusely scattered oblique light. Hence, the absolute light fluence rate would be underestimated. The underestimate would be worse for regions deeper into tissue where light scattering is more isotropic and less forward scattered.

Appendix B

Diffusion Approximation Equation: Two Layer Solution

B.1 Homogeneous and Particular Solutions

The total light fluence in tissue can be described as the sum of the collimated and the diffuse photon flux. The diffuse photon flux (or fluence rate) is obtained by solving the particular, ϕ_p, and homogeneous, ϕ_h, solution of the light diffusion approximation. This gives a total fluence rate of

$$\begin{aligned} \phi_{total} &= \phi_{diffuse} + \phi_{collimated} \\ &= \phi_h + \phi_p + \phi_{collimated} \\ &= \phi_h + \phi_p + \frac{P_o}{4\pi r^2} exp(-\mu'_{tr} r) \end{aligned} \tag{B.1}$$

The collimated fluence, $\phi_{collimated}$ is due to the contribution of straight path photons that are extinguished by encountering a single absorption or scattering event, where P_o is the total power of the source in watts. The following sections solve the homogeneous and particular solution of the light diffusion approximation for a two layer system in spherical coordinates. The general format of the diffusion equation in spherical coordinates is:

$$-D \cdot \nabla^2 \phi(r) + \mu_a \cdot \phi(r) = \mu'_s \phi_o \frac{exp(-\mu'_{tr} r)}{r^2} \tag{B.2}$$

which when expanded gives:

$$-D \cdot \frac{\partial^2 (r\phi(r))}{\partial r^2} + \mu_a \cdot r\phi(r) = \mu'_s \phi_o \frac{exp(-\mu'_{tr} r)}{r^2} \tag{B.3}$$

where

$$\begin{aligned}
\phi &= \text{fluence rate } (\ W \cdot cm^{-2}) \\
\phi_o &= \frac{P_o}{4\pi} \text{ where } P_o \text{ is the total laser power } (\ W \cdot cm^{-2}) \\
\mu_a &= \text{absorption coefficient } (\ cm^{-1}) \\
\mu_s' &= \text{effective scattering coefficient } (\ cm^{-1}) \\
&= (1-g)\mu_s \\
\mu_{tr}' &= \text{transport attenuation coefficient } (\ cm^{-1}) \\
&= \mu_s' + \mu_a \\
D &= \text{diffusion constant } (\ cm^{-1}\ ) \\
&= [3(\mu_s' + \mu_a)]^{-1}
\end{aligned}$$

The right hand side represents the source term, which represents the distribution of the first-scattered photons from the light source [110]. Expanding B.3 in spherical coordinates and setting

$$Y = r\phi(r) \tag{B.4}$$

gives the simplified differential equation:

$$\begin{aligned}
-DY''(r) + \mu_a Y(r) &= f(r) \\
&= Y_o \frac{exp(-\mu_{tr}' r)}{r}
\end{aligned} \tag{B.5}$$

where $Y_o = \mu_s' \frac{P_o}{4\pi}$. This equation has a homogeneous and particular solution. The homogeneous solution is solved when the right hand side of equation (B.5) is set to zero. This gives:

$$Y_h(r) = Ay_1(r) + By_2(r) \tag{B.6}$$

$$= Aexp(-\mu_{eff} r) + Bexp(+\mu_{eff} r) \tag{B.7}$$

where $\mu_{eff} = \sqrt{\frac{\mu_a}{D}}$ and A and B are the unknown coefficients of the solution[1]. The particular solution can be solved using a one sided Green's function [27]:

$$\begin{aligned}
Y_p(r) &= \int_r^{r_o} \frac{y_1(\tau)y_2(r) - y_1(r)y_2(\tau)}{W(y_1, y_2)(\tau)} \cdot f(\tau) d\tau \\
&= \frac{Y_o}{2\mu_{eff}} \left(exp(\mu_{eff} r) \int_r^{ro} \frac{exp((-\mu_{eff} - \mu_{tr}')r)}{r} dr \right) - \\
&\quad \frac{Y_o}{2\mu_{eff}} \left(exp(-\mu_{eff} r) \int_r^{ro} \frac{exp((\mu_{eff} - \mu_{tr}')r)}{r} dr \right)
\end{aligned} \tag{B.8}$$

[1] note that for a homogeneous single layer medium. $B = 0$ since the fluence tends to zero as r approaches ∞. This gives equation (3.6) of chapter 3

where $W(y_1, y_2)$ is the Wronskian of y_1 and y_2 which is equal to:

$$W(y_1, y_2) = y_1 y_2' - y_1' y_2 = 2\mu_{eff} \tag{B.9}$$

Note that the particular solution is a linear combination of the homogeneous solution. As a result we can choose an arbitrary upper limit of integration, r_o such that the definite integral portion will be absorbed by constants A and B when solving for equation (B.7). Setting r_o to ∞ produces the exponential integral function, E_i of the first order, E_1 which is defined as

$$E_1(x) = \int_x^\infty \frac{exp(-t)}{t} dt \tag{B.10}$$

which then simplifies B.8 to

$$Y_p(r) = \frac{Y_o}{2\mu_{eff}} (exp(\mu_{eff} r) \cdot E_1(\alpha r) - exp(-\mu_{eff} r) E_1(\beta r)) \tag{B.11}$$

where

$$\alpha = \mu_{tr}' + \mu_{eff} \text{ and } \beta = \mu_{tr}' - \mu_{eff} \tag{B.12}$$

By substituting back equation (B.4), the particular solution of the fluence rate is

$$\phi_p(r) = \mu_s' \frac{\phi_o}{2\mu_{eff} r} (exp(\mu_{eff} r) \cdot E_1(\alpha r) - exp(-\mu_{eff} r) E_1(\beta r)) \tag{B.13}$$

The homogeneous and the particular solution must be used to solve for the diffusion equation with boundary conditions for the two layer system (see figure 3.1). The next section describes the boundary conditions, and the method of solving for the unknown coefficients of equation (B.7). This method has been adapted for spherical coordinates from the slab geometry case presented by Vitkin *et al* [110].

B.2 Boundary Conditions for Two Media

The diffuse fluence rate in the first medium (the layer closest to the source) can be expressed as:

$$\begin{aligned} \phi_1 &= \phi_h + \phi_p \\ &= A_1 \frac{exp(-\mu_{eff_2} r)}{r} + B_1 \frac{exp(\mu_{eff_1} r)}{r} + \qquad (B.14) \\ &\quad \frac{\mu_s' \phi_o}{2\mu_e r} (exp(\mu_e r) E_1(\alpha r) - exp(-\mu_e r) E_1(\beta r)) \qquad (B.15) \end{aligned}$$

That in medium 2 is:

$$\phi_2 = \phi_h = A_2\frac{exp(-\mu_{eff_2}r)}{r} + B_2\frac{exp(\mu_{eff_2}r)}{r} \tag{B.16}$$

$B_2 = 0$ since the fluence in medium 2 approaches zero as r approaches ∞. The particular solution is not present in medium 2 since the contribution of the source function (right hand side of equation (B.3)) is assumed to be negligible in medium 2. Therefore the unknowns are: A_1, B_1 and A_2.

The boundary conditions are such that there is I) continuous fluence rate and II) continuous photon current between the two layers at $r = r_o$. The final condition assumes III) an overall energy balance. Mathematically, these conditions are represented as:

I) $\phi_1(r_o) = \phi_2(r_o)$

II) $\phi_1'(r_o) = \frac{D_2}{D_1}\phi_1'(r_o)$

III) $P_{total} = P_1 + P_2 = P_o$

Using the properties of a one sided Green's Function, equations I) and II) are simplified using the fact that for a solution with homogeneous and particular parts, $y(r) = y_h(r) + y_p(r)$, with boundary condition at $r = r_o$ equal to [27]:

$$\begin{aligned} y(r_o) &= k_o \\ y'(r_o) &= k_1 \end{aligned} \tag{B.17}$$

is equivalent to solving

$y_p(r_o) = 0 \qquad y_p'(r_o) = 0$

$y_h(r_o) = k_o \qquad y_h(r_o) = k_1$

Hence, the particular solutions can be set to 0 in medium 1. Furthermore, k_o and k_1 are defined by the imposed fluence conditions in medium 2. Therefore, the boundary conditions I and II become:

I) $\phi_1(r_o) = \phi_2(r_o) \Rightarrow$
$A_1\frac{exp(-\mu_{eff_1}r_o)}{r_o} + B_1\frac{exp(\mu_{eff_1}r_o)}{r_o} = A_2\frac{exp(-\mu_{eff_2}r_o)}{r_o}$

II) $\phi_1'(r_o) = \phi_2'(r_o) \Rightarrow$
$A_1 exp(-\mu_{eff_1}r_o)(\frac{-\mu_{eff_1}}{r_o} - \frac{1}{r_o^2}) + B_1 exp(\mu_{eff_1}r_o)(\frac{\mu_{eff_1}}{\mu_o} - \frac{1}{r_o^2}) = \frac{D_2}{D_1}\cdot A_2 \cdot exp(-\mu_{eff_2}r_o)(\frac{\mu_{eff_2}}{r_o} + \frac{1}{r_o^2})$

The third equation is the total energy balance of both diffuse and collimated photons such that:

$$P_o = \int \mu_a \phi dV \tag{B.18}$$

$$= \int \mu_{a_1} \phi_1 dV + \int \mu_{a_2} \phi_2 dV$$

$$= \int \mu_{a_1} (\phi_{h_1} + \phi_{p_1} + \phi_{collimated_1}) dV + \tag{B.19}$$

$$\int \mu_{a_2} (\phi_{h_2} + \phi_{p_2} + \phi_{collimated_2}) dV \tag{B.20}$$

for $dV = 4\pi r^2 dr$ and where

$$\phi_{collimated_1} = \phi_o \frac{exp(\mu'_{tr_1} r)}{r^2} \qquad r < r_o \tag{B.21}$$

$$\phi_{collimated_2} = \phi_o \frac{exp(-\mu'_{tr_1} r_o)}{r_o^2} \cdot \frac{exp(-\mu'_{tr_2} r)}{r^2} \qquad r > r_o$$

Note that in medium 2, ϕ_{p_2} is assumed to be zero and secondly that $\phi_{collimated}$ has been attentuated by $\phi_o \cdot \frac{exp(-\mu'_{tr_1} r_o)}{r_o^2} = \phi_{o_2}$ as it passes through medium 1. Substituting and rearranging the homogeneous and particular solutions (equations (B.14) through (B.16)), and the collimated solutions (equations (B.21) and (B.22)) produces

$$\mu_{a_1} A_1 \int_0^{r_o} exp(-\mu_{eff_1} r) r dr + \mu_{a_1} B_1 \int_0^{r_o} exp(\mu_{eff_1} r) r dr + \mu_{a_2} A_2 \int_{r_o}^{\infty} exp(-\mu_{eff_2} r) r dr$$
$$= \frac{P_o}{4\pi} - \mu_{a_1} \int_0^{r_o} \phi_{o_1} exp(-\mu'_{tr_1} r) dr - \mu_{a_2} \int_0^{r_o} \phi_{o_2} exp(-\mu'_{tr_2} r_o) dr$$
$$-\mu_{a_1} \int_0^{r_o} \frac{\mu_{s_1} \phi_{o_1}}{2\mu_{eff_1}} r (exp(\mu_{eff_1} r) E_1(\alpha_1 r) - exp(-\mu_{eff_1} r) E_1(\beta r)) dr \tag{B.22}$$

Using the three boundary conditions, this produces a set of equations which can be solved with matrix operations such that:

$$\vec{Y} = \vec{A}\vec{X} \tag{B.23}$$

where $X = \begin{bmatrix} A_1 \\ B_1 \\ A_2 \end{bmatrix}$ and $Y = \begin{bmatrix} 0 \\ 0 \\ \gamma(r) \end{bmatrix}$

$\gamma(r)$ is obtained from the energy balance and is equal to:

$$\gamma(r) = \frac{P_o}{4\pi} + \frac{\mu_{a_1} \phi_{o_1}}{\mu'_{tr_1}} [exp(-\mu'_{tr_1} r_o) - 1] + \frac{\mu_{a_2} \phi_{o_2}}{\mu'_{tr_2}} [exp(-\mu'_{tr_2} r_o) - 1] \tag{B.24}$$

$$-\mu_{a_1} \int_0^{r_o} \frac{\mu_{s_1} \phi_{o_1}}{2\mu_{eff_1}} r (exp(\mu_{eff_1} r) E_1(\alpha_1 r) - exp(-\mu_{eff_1} r) E_1(\beta r)) dr \tag{B.25}$$

The matrix A is equal to:

$$\begin{bmatrix} \frac{exp(-\mu_{eff_1} r_o)}{r_o} & \frac{exp(\mu_{eff_1} r_o)}{r_o} & \frac{-exp(-\mu_{eff_2} r_o)}{r_o} \\ exp(-\mu_{eff_1} r_o)(\frac{-\mu_{eff_1}}{r_o} - \frac{1}{r_o^2}) & exp(\mu_{eff_1} r_o)(\frac{\mu_{eff_1}}{r_o} - \frac{1}{r_o^2}) & \frac{D_2}{D_1} exp(-\mu_{eff_2} r_o)(\frac{\mu_{eff_2}}{r_o} + \frac{1}{r_o^2}) \\ \mu_{a_1}[\frac{exp(-\mu_{eff_1} r_o)}{-\mu_{eff_1}}(r_o - \frac{1}{-\mu_{eff_1}}) + \frac{1}{-\mu_{eff_1}^2}] & \mu_{a_1}[\frac{exp(\mu_{eff_1} r_o)}{\mu_{eff_1}}(r_o - \frac{1}{\mu_{eff_1}}) + \frac{1}{\mu_{eff_1}^2}] & \mu_{eff_2}[\frac{exp(-\mu_{eff_2} r_o)}{-\mu_{eff_2}}(\frac{1}{-\mu_{eff_2}} - r_o) \end{bmatrix}$$

The constant coefficients, A_1, B_1 and A_2, were thus solved using Kramer's Rule. The determined coefficients were then substituted back into the original equation for fluence (equations (B.14) through (B.16)) to give the net fluence which is comprised of both collimated and diffuse contributions. For example, in medium 1 the fluence is equal to:

I) diffuse: $A_1 \frac{exp(-\mu_{eff_1} r)}{r} + B_1 \frac{exp(\mu_{eff_1} r)}{r} + \frac{\mu_{a_1} \phi_o}{2\mu_{eff_1} r}[exp(\mu_{eff_1} r) E_1(\alpha r) - exp(-\mu_{eff_1} r) E_1(\beta r)]$

II) collimated: $\phi_{o_2} \frac{exp(-\mu'_{tr_1} r)}{r^2}$

where $\phi_{o_1} = \frac{P_o}{4\pi} \cdot \frac{exp(-\mu'_{tr_1} r)}{r^2}$

And similarly in medium 2:

I) diffuse: $A_2 \frac{exp(-\mu_{eff_2} r)}{r}$

II) collimated: $\phi_{o_2} \frac{exp(-\mu'_{tr_2} r)}{r^2}$

where $\phi_{o_2} = \frac{P_o}{4\pi} \cdot \frac{exp(-\mu'_{tr_1} r_o)}{r_o^2}$

An analysis of the contribution of the diffuse particular term (equation (B.24)) was performed using numerical methods. The analysis showed that the contribution was negligible compared with the homogeneous contribution for typical values of μ_a and μ'_s (equation (B.25)). Therefore, it was ignored in the calculation of fluence for the two layer solution. The final matrix operation was thus significantly simplified to:

$$\vec{Y} = \vec{A}\vec{X} \tag{B.26}$$

where $X = \begin{bmatrix} A_1 \\ B_1 \\ A_2 \end{bmatrix}$ and $Y = \begin{bmatrix} 0 \\ 0 \\ \Gamma(r) \end{bmatrix}$

and where $\Gamma(r)$ is now equal to:

$$\Gamma(r) = \frac{P_o}{4\pi} + \frac{\mu_{a_1}\phi_{o_1}}{\mu'_{tr_1}}[exp(-\mu'_{tr_1}r_o) - 1] + \frac{\mu_{a_2}\phi_{o_2}}{\mu'_{tr_2}}[exp(-\mu'_{tr_2}r_o) - 1] \quad \text{(B.27)}$$

Appendix C

Testing of Model

Comparison with Analytical Solution

The numerical model was compared against the steady state analytical solution of the bioheat equation for an isotropic light source in an infinite homogeneous medium [129]. The steady state solution has the form:

$$T(r) = \frac{P_o}{4\pi k r}\left[1 - exp\left(\frac{-r}{L_{opt}}\right)\right] \tag{C.1}$$

where P_o is the total power , k is the thermal conductivity and

$$L_{opt} \simeq \frac{1}{\sqrt{3\mu_a(\mu_a + \mu_s')}}[1 + 0.4\mu_a/\mu_{tr}'] \text{ [129]} \tag{C.2}$$

Note that this analytical solution does not include the convective blood flow term. The analytical solution was compared with the numerical results by running the simulation with long time domains ($10\,ksec$, $50\,ksec$ and $100\,ksec$). Figure C.1 is a plot of the numerical calculation of temperature profile against the analytical result as a function of radial distance. The plot shows that for longer times, the numerical solution converges to the analytical solution.

Energy Balance

The validity of the model is dependent upon correctly calculating temperature at each timestep. However, time dependent analytical solutions to the bioheat equation do not exist. Consequently an energy balance was performed to confirm the calculation of heat transfer in tissue for all t. Note that an energy balance is required for, but does not guarantee, the correctness of $T(r,t)$.

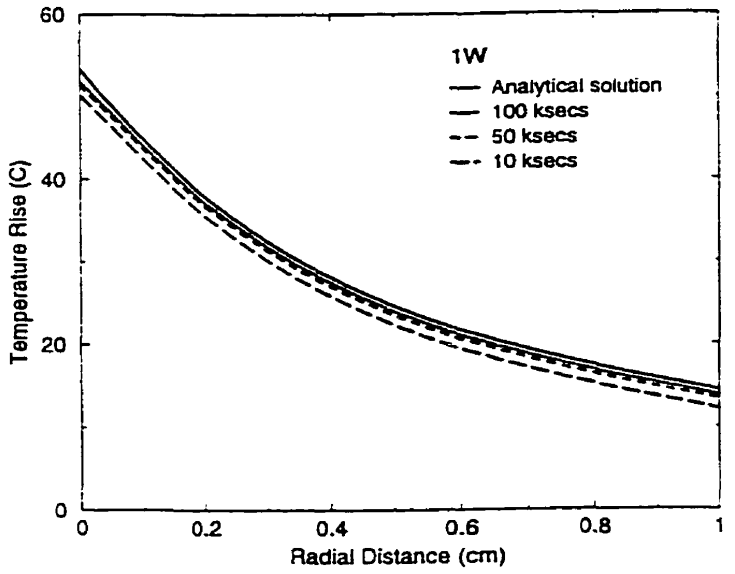

Figure C.1: Validation of numerical results with analytical solution. The analytical solution is the steady state solution of temperature profile for the an isotropic point source in a homogeneous, diffusing medium [129]

The energy transfer in tissue was calculated according to the resultant temperature rise:

$$E_{transferred}(\tau) = \int_0^{\tau} 4\pi r^2 \int_{r_f}^{L} [\rho c T(r,t) + w_b c_b (T(r,t) - T_{art})] dt\, dr \tag{C.3}$$

where L approaches ∞. This was compared with the light energy deposited into the system for dynamic optical properties

$$E_{deposited}(\tau) = \int_0^{\tau} 4\pi r^2 \int_{r_f}^{L} P(r,t) dt\, dr \tag{C.4}$$

The two curves are plotted in figure C.2. After 15 minutes of heating, The difference between the deposited and transferred energies is 0.3% relative to the deposited energy.

Convergence with Spatial Step size

In general, the smaller the difference in distance between the nodes in the solution domain, the more accurate the results. The largest variation in temperature due to changes in step size occurred at r_f, the location of maximum temperature rise. Figure C.3 is a plot of the peak temperature rise after 15 minutes of heating at r_f as a function of spatial step size, Δr. The simulation was computed for the case of static coagulative, static native and

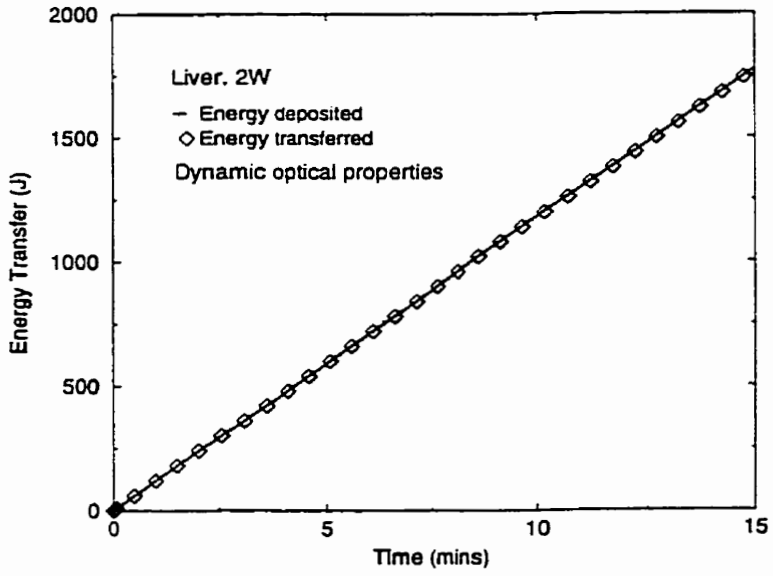

Figure C.2: Energy balance between energy deposited into tissue and energy transfer due to thermal conduction and convection. The difference between deposited and transfer energies is 0.3 % after 15 mins of heating at 2W.

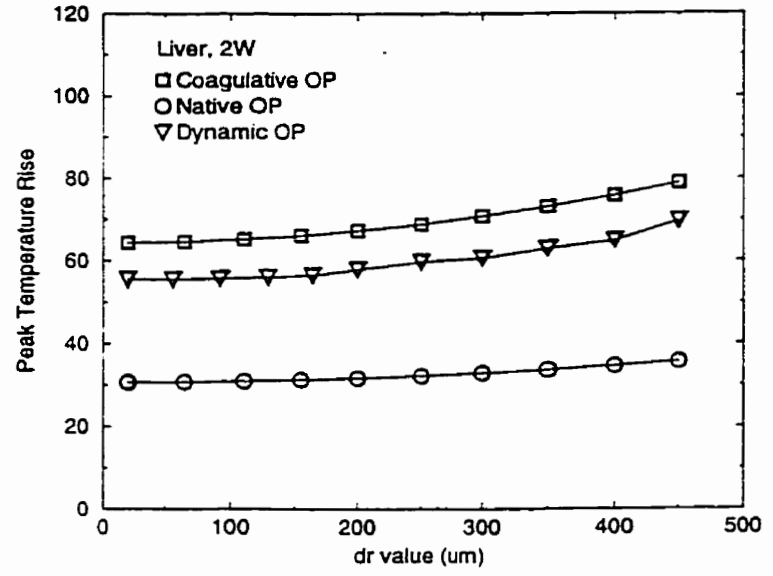

Figure C.3: Effects of node size, dr, on final and peak temperature predictions after 15 mins of heating in liver fo static and dynamic optical properties.

dynamic optical properties. To reduce computation time, the corresponding value of Δt was maximized to the limit imposed by the Fourier condition of equation 3.26. The results show that the solution converged for smaller values of Δr. However, smaller step sizes require more computation time. Therefore, a practical value of $\Delta r = 100 \mu m$ was chosen.

References

[1] ICRP Publication 23. Report of the task group on reference man. Technical report. International Commission on Radiological Protection, Oxford, 1975.

[2] Z. Amin, W.R. Lees, and S.G. Bown. Interstitial laser photocoagulation for the treatment of prostatic cancer. *British Journal of Surgery*, 66:1044–1047, 1993.

[3] Z. Amin, W. Thurrell, G.M. Spencer, S.A. Harries, W.E. Grant, S.G. Bown, and W.R. Lees. Computed tomography-pathologic assessment of laser-induced necrosis in rat liver. *Investigative Radiology*, 28(12):1148–1154, 1993.

[4] D. Ans and E. Lax. *Taschenbuch für Chemiker und Physiker.* Makroskopische physikalisch-chemische eigenschaften. Springer-Verlag, Berlin, 1967.

[5] B. Anvari, S. Rastegar, and M. Motamedi. Modeling of intraluminal heating of biological tissue: Implications for treatment of benign prostatic hyperplasia. *IEEE Transactions on Biomedical Engineering*, 41(9):854–863, 1994.

[6] P.W. Ascher. Interstitial thermotherapy of brain tumors with Nd:YAG laser under real time MRI control. In *Laser-surgery, advanced characterization therapeutics and system II*, volume 1200, pages 242–245. SPIE, 1990.

[7] Thorlab Technical authors. PDA50-amplified silicon detector. Technical report. Thorlab.

[8] K.D. Bauer and K.J. Henle. Arrhenius analysis of heat survival curves from normal and thermotolerant CHO cells. *Radiation Research*, 78:251–263, 1979.

[9] C.M. Beacco, S.R. Mordon, and J.M. Brunetaud. Development and experimental *in vivo* validation of mathematical modeling of laser coagulation. *Lasers in Surgery and Medicine*, 14:362–373, 1994.

[10] B.E. Billard. K. Hynynen. and R.B. Roemer. Effects of physical parameters on high temperature ultrasound hyperthermia. *Ultrasound in Medicine and Biology*, 16:409–420, 1990.

[11] M.J. Borrelli, L.L. Thompson. C.A. Cain, and W.C. Dewey. Time-temperature analysis of cell killing of BHK cells heated at temperatures in the range of 43.5 ℃ to 57.0 ℃. *International Journal of Radiation, Oncology, Biology and Physics*, 19:389–399, 1990.

[12] J. Boulnois. Photophysical processes in recent medical laser developments: a review. *Lasers in Medical Science*, 1:47–66, 1986.

[13] S.G. Bown. Phototherapy of tumours. *World Journal of Surgery*, 7:700–709, 1983.

[14] S.G. Bown. New techniques in laser therapy. *British Medical Journal*, 316:754–757, 1998.

[15] C. Bremer, T. Allkemper, J. Menzel, U. Sulkowski, E. Rummeny, and P. Reimer. Preliminary clinical experience with laser-induced interstitial thermotherapy in patients with hepatocellular carcinoma. *Journal of Magnetic Resonance Imaging*, 8(1):235–239, 98.

[16] S.L. Brown, J.W. Hunt, and R.P. Hill. A comparison of the rate of clearance of xenon and pertechnetate ion in murine tumors and normal leg muscles. *Nuclear Medicine and Biology*, 15(4):381–390. 1988.

[17] C.K. Charny. Mathematical models of bioheat transfer. *Advances in Heat Transfer*. 22:19–155, 1992.

[18] J. Crezee and J.J.W. Lagendijk. Experimental verification of bioheat transfer theories: Measurement of temperature profiles around large artificial vessels in perfused tissue. *Physics in Medicine and Biology*, 35:905–923, 1990.

[19] J. Crezee. J. Mooibroek. C.K. Box. and J.J.W Lagendijk. Interstitial heating: Experiments in artificially perfused bovine tongues. *Physics in Medicine and Biology*, 36(6):823–833. 1991.

[20] D.R. Croft and D.G. Lilley. *Heat Transfer Calculations using Finite Difference Equations*. Applied Science Publishers Ltd.. Essex. 1 edition. 1977.

[21] M. Davis, J. Dowden, and A. Steger. A mathematical model for interstitial laser treatment of tumours using four fibers. *Lasers in Medical Science*, 4(1):41, 1989.

[22] G.J. Derbyshire. Thermally induced optical property changes in myocardium at 1.06 μm. *Lasers in Surgery and Medicine*, 10:28–34, 1990.

[23] T.F. Deutsch. Medical applications of laser. *Physics Today*, pages 56–63, 1988.

[24] J.M. Dowden, M. Davis, P. Kapadia, and K. Matthewson. Heat flow in laser treatment by local hyperthermia. *Lasers in Medical Science*, 2(3):211, 1987.

[25] F.A. Duck. *Physical Properties of Tissue, Complete Reference Book*. Academic Press. London, England, 1990.

[26] J.J. Duderstadt and L.J. Hamilton. *Nuclear Reactor Analysis*. Wiley, New York. 1976.

[27] C.H. Edwards and D.E. Penney. *Elementary Differential Equations with Boundary Value Problems*. Prentice Hall, Englewood Clifs, New Jersey, 2 edition, 1989.

[28] B Emami, G Nussbaum, N Hahn, A Piro, A Dritschilo, and F Quimby. Histopathological study on the effects of hyperthermia on microvasculature. *International Journal of Radiation, Oncology, Biology and Physics*, 7:343–348, 1981.

[29] M.A. Fahim and F. el-Sabban. Hyperthermia induces ultrastructural changes in mouse plial microvessels. *Anatomical Record*, 242(1):77–82, 1995.

[30] J. Fehy, R. Gutmann, A. Leunig, L. Jager, M. Reiser, R.E. Saxton, D.J. Castro, and E. Kastenbauer. MRI-guided laser interstitial thermal therapy (LITT) of head and neck tumors: progress with a new method. *Journal of Clinical Laser Medicine and Surgery*, 14(6):361–366, 1996.

[31] S.B. Field and J.W. Hand. *An introduction to the practical aspects of clinical hyperthermia*, chapter 1, pages 1–9. Taylor and Francis, Bristol, PA, 1990.

[32] M. Firbank and D.T. Delpy. A design for a stable and reproducible phantom for use in near-infrared imaging and spectroscopy. *Physics in Medicine and Biology*, 38:847–853, 1993.

[33] M. Firbank, M. Oda, and D.T. Delpy. An improved design for a stable and reproducible phantom material for use in near-infrared spectroscopy and imaging. *Physics in Medicine and Biology*, 40:955–961, 1995.

[34] S.T. Flock, S.L. Jacques, B.C. Wilson, W.M. Star, and M.J.C. van Gemert. Optical properties of intralipid: a phantom medium for light propagation studies. *Lasers in Surgery and Medicine*. 12:510–519, 1992.

[35] S.T. Flock, M.S. Patterson, B.C. Wilson, and D.R. Wyman. Monte carlo modeling of light propagation in highly scattering tissues–I: Model predictions and comparison with diffusion theory. *IEEE Transactions on Biomedical Engineering*, 36(12):1162–1168, 1989.

[36] A. Gangi, J.L. Dietemann, B. Gasser, R. Mortazavi, P. Brunner, M.Y. Mourou, J.C. Dosch, J. Durckel, J. Marescaux, and C. Roy. Interstitial laser photocoagulation of osteoid osteomas with use of CT guidance. *Radiology*, 203(3):843–848, 1997.

[37] T. Glenn, S. Rastegar, and S.L. Jacques. Finite element analysis of temperature controlled coagulation in laser irradiated tissue. *IEEE Transactions on Biomedical Engineering*, 43(1):79–87, 1996.

[38] L.I. Grossweiner. Light dosimetry model for photodynamic therapy treatment planning. *Lasers in Surgery and Medicine*, 11:165–173, 1991.

[39] H. Mumtaz H, M.A. Hall-Craggs, A. Wotherspoon, M. Paley, G. Buonaccorsi, Z. Amin, I. Wilkinson, M.W. Kissin, T.I. Davidson, I. Taylor, and S.G. Bown. Laser therapy for breast cancer: Mr imaging and histopathologic correlation. *Radiology*, 200(3):651–658, 1996.

[40] T. Halldorsson, J. Langerholc, L. Senatori, and H. Funk. Thermal action of laser irradiation in biological material monitored by egg-white coagulation. *Applied Optics*. 20(5):822–825, 1981.

[41] S.A. Harries, Z. Amin, M.E.F. Smith, W.R. Lees, J. Cooke, M.G. Cook, J.H. Schurr, M.W. Kissin, and S.G. Bown. Interstitial laser photocoagulation as a treatment for breast cancer. *British Journal of Surgery*, 81:1617–1619, 1994.

[42] J. Heisterkamp, R. van Hillegersberg, E. Sinofsky, and J.N. Ijzermans. Heat-resistant cylindrical diffuser for interstitial laser coagulation: x comparison with the bare-tip fiber in a porcine liver model. *Lasers in Surgery and Medicine*. 20(3):304–309, 1997.

[43] F.C. Henriques. Studies of thermal injury v. the predictability and the significance of thermally induced rate processes leading to irreversible epidermal injury. *Archives of Pathology*, 43:489–502, 1947.

[44] A.H. Hielscher, R.E. Alcouffe, and R.L. Barbour. Comparison of finite-difference transport and diffusion calculations for photon migration in homogeneous and heterogeneous tissues. *Physics in Medicine and Biology*, 43:1285–1302, 1998.

[45] A.H. Hielscher, S.L. Jacques, L. Wang, and F.K. Tittel. The influence of boundary conditions on the accuracy of diffusion theory in time-resolved reflectance spectroscopy of biological tissues. *Physics in Medicine and Biology*, 40(11):1957–1975, 1995.

[46] K. Ivarsson, J. Olsrud, C. Sturesson, P.H. Moller, B.R. Persson, and K.G. Tranberg. Feedback interstitial diode laser (805 nm) thermotherapy system: *ex-vivo* evaluation and mathematical modeling with one and four-fibers. *Lasers in Surgery and Medicine*, 22(2):86–96, 1998.

[47] S.L. Jacques, C. Newman, and X.Y. He. Thermal coagulation of tissues: Liver studies indicate a distribution of rate parameters, not a single rate parameter, describes the coagulation process. In *Advances in Biological Heat and Mass Transfer*, volume HTD-Vol.189/BED-Vol.18, pages 71–73. ASME, 1991.

[48] S.L. Jacques and S.A. Prahl. Modeling optical and thermal distributions in tissue during laser irradiation. *Lasers in Surgery and Medicine*, 6:494–503, 1987.

[49] S.L. Jacques, S. Rastegar, S. Thomsen, and M. Motamedi. The role of dynamic changes in blood perfusion and optical properties in laser coagulation of tissue. *IEEE Journal of Selected Topics in Quantum Electronics*, 2(4):922–933, 1996.

[50] L. Jager, G.U. Muller-Lisse, R. Gutmann, J. Feyh, M. Thoma, and M. Reiser. Initial results with MRI-controlled laser-induced interstitial thermotherapy of head and neck tumors. *Radiologe*, 36(3):236–244, 1996.

[51] S. Jaywant, B. Wilson, M. Patterson, L. Lilge, T. Flotte, T.J. Woolsey, and C. McCulloch. Temperature dependent changes in the optical absorption and scattering spectra of tissues: Correlation with ultrastructure. In *Laser-Tissue Interaction IV*, volume 1882, pages 218–228. SPIE, 1993.

[52] F.H. Johnson, H. Eyrina, and B.J. Stover. *The Theory of Rate Processes in Biology and Medicine*. Wiley, New York, 1974.

[53] F.A. Jolesz. Interventional and intraoperative MRI: a general overview of the field. *Journal of Magnetic Resonance Imaging*, 8(1):3–7, 1998.

[54] J.N. Kabalin. Laser prostatectomy is a safer, better operation than electrovaporization of the prostate (review). *Urology*, 49(2):160–165, 1997.

[55] T. Kahn, T. Harth, J.C. Kiwit, H.J. Schwarzmaier, C. Wald, and U. Modder. In vivo MRI thermometry using a phase-sensitive sequence: preliminary experience during MRI-guided laser-induced interstitial thermotherapy of brain tumors. *Journal of Magnetic Resonance Imaging*, 8(1):160–164, 1998.

[56] J.L. Karagiannes, Z. Zhang, B. Grossweiner, and L.I. Grossweiner. Applications of the 1-D diffusion approximation to the optics of tissues and tissue phantoms. *Applied Optics*, 28(12):2311–2317, 1989.

[57] B.M. Kim, S.L. Jacques, S. Rastegar, S. Thomsen, and M. Motamedi. Nonlinear finite-element analysis of the role of dynamic changes in blood perfusion and optical properties in laser coagulation of tissue. *IEEE Journal of Selected Topics in Quantum Electronics*, 2(4):922–933, 1996.

[58] M. Kohl, M. Essenpreis, and M. Cope. The influence of glucose concentration upon the transport of light in tissue-simulating phantoms. *Physics in Medicine and Biology*, 40(7):1267–87, 1995.

[59] M.C. Kolios, M.D. Sherar, and J.W. Hunt. Blood flow cooling and ultrasonic lesion formation. *Medical Physics*, 23(7):1287–1298, 1996.

[60] G.L LeCarpentier, M. Motamedi, L.P McMath, S. Rastegar, and A.J. Welch. Continuous wave laser ablation of tissue: analysis of thermal and mechanical events. *IEEE Transactions on Biomedical Engineering*, 40(2):188–200, 1993.

[61] D Liu, K Svanberg, I Wang, S Andersson-Engels, and S Svanberg. Laser doppler perfusion imaging: New technique for determination of perfusion and reperfusion of splanchnic organs and tumor tissue. *Lasers in Surgery and Medicine*, 20:473–479, 1997.

[62] R. London, M.E. Glinsky, G.B. Zimmerman, and D.C. Eder. Coupled light transport-heat diffusion model for laser dosimetry with dynamic optical properties. In *Laser-tissue interaction VI*, volume 2391, pages 434–442. SPIE, 1995.

[63] A.L. McKenzie. Physics of thermal processes in laser-tissue interaction. *Physics in Medicine and Biology*, 35(9):1175–1209, 1990.

[64] R. Meijerink, M. Essepreis, J.W. Pickering C. H. Massen, T.N. Mills, and M.J.C van Gemert. Rate process parameters of egg white measured by light scattering. In G. Müller and A. Roggan, editors, *Laser-Induced Interstitial Thermotherapy*, chapter Part II: Optical and Thermal Properties of Biological Tissue, pages 66–84. SPIE Press, Bellingham, Washington, 1 edition, 1995.

[65] T. Menovsky, J.F. Beek, M.J. van Gemert, F.X. Roux, and S.G. Bown. Interstitial laser thermotherapy in neurosurgery: a review. *Acta Neurochirurgica*, 138(9):1019–1026, 1996.

[66] S. Mordon, T. Desmettre, J.M. Devoiselle, and S. Soulie. Thermal damage assessment of blood vessels in a hamster skin flap model by fluorescence measurement of a liposome-dye system. *Lasers in Surgery and Medicine*, 20:131–141, 1997.

[67] E.G. Moros, A.W. Dutton, R.B. Roemer, M. Burton, and K. Hynynen. Experimental evaluation of two simple thermal models using hyperthermia *in vivo*. *International Journal of Hyperthermia*, 9:581–598, 1993.

[68] P.R. Morrison, F.A. Jolesz, D. Charous, R.V. Mulkern, S.G. Hushek, R. Margolis, and M.P. Fried. MRI of laser-induced interstitial thermal injury in an in vivo animal liver model with histologic correlation. *Journal of Magnetic Resonance Imaging*, 8(1):57–63, 1998.

[69] R. Muschter, S. Hessel, P. Jahnen, H. Yalavac, and A. Hofstetter. Evaluation of different laser wavelengths and application systems for LITT. In G. Müller and A. Roggan, editors, *Laser-Induced Interstitial Thermotherapy*, chapter Part IV: Design and Properties of Interstitial Laser Applicators, pages 212–223. SPIE Press, Bellingham, Washington, 1 edition, 1995.

[70] R. Muschter and A. Hofstetter. Laser thermocoagulation of adenoma of the prostate using an interstitial approach. *Annales d Urologie*, 31(1):27–37, 1997.

[71] Y. Ni, Y. Miao C. Petre, J. Yu, E. Cresens, P. Adriaens, H. Bosmans, W. Semmler, A.L. Baert, and G. Marchal. Magnetic resonance imaging-histomorphologic correlation studies on paramagnetic metalloporphyrins in rat models of necrosis. *Investigative Radiology*, 32(12):770–779, 1997.

[72] Whitehurst C. Pantelides ML. Moore JV. Brooman PJ. Blacklock NJ. In vivo laser light distribution in human prostatic carcinoma. *Journal of Urology*, 151(5):1411–1415, 1994.

[73] A.A. Oraevsky, S.L. Jacques, R.O. Esanaliev, and F.K. Tittel. Pulsed laser ablation of soft tissues, gels, and aqueous solutions at temperatures below 100 °C. *Lasers in Surgery and Medicine*, 18(3):231–40, 1996.

[74] K. Orth, D. Russ, J. Duerr, R. Hibst, R. Steiner, and H.G. Beger. Thermo-controlled device for inducing deep coagulation in the liver with the Nd:YAG laser. *Lasers in Surgery and Medicine*, 20(2):149–156, 1997.

[75] M.S. Patterson, B.C. Wilson, and D.R. Wyman. The propagation of optical radiation in tissue I. models of radiation transport and their application. *Lasers in Medical Science*, 6:155–168, 1991.

[76] J.A. Pearce and S.L. Thomsen. Rate process analysis of thermal damage. In A.J. Welch and M.J.C. van Gemert, editors, *Optical-Thermal Response of Laser Irradiated Tissue*, chapter 17, pages 561–608. Plenum Press, New York, N.Y., 1995.

[77] H.H. Pennes. Analysis of tissue and arterial blood temperatures in the resting forearm. *Journal of Applied Physiology*, 1:93–122, 1948.

[78] C. Philipp, E. Rohde, and H. Berlien. Treatment of congenital vascular disorders (cvd) with laserinduced thermotherapy. In G. Müller and A. Roggan, editors, *Laser-Induced Interstitial Thermotherapy*, chapter Part IV: Clinical Results, pages 443–458. SPIE Press, Bellingham, Washington, 1 edition, 1995.

[79] J.W. Pickering. Optical property changes as a result of protein denature in albumen and yolk. *Journal of Photochemistry, Photobiology and B: Biology*, 16:101–111, 1992.

[80] J.W. Pickering, P. Posthumus, and J.C. van Gemert. Continuous measurement of the heat-induced changes in the optical properties (at 1064 nm) of rat liver. *Lasers in Surgery and Medicine*, 15:200–205, 1994.

[81] B.W. Pogue, M.S. Patterson, H. Jian, and K.D. Paulsen. Initial assessment of a simple system for frequency domain diffuse optical tomography. *Physics in Medicine and Biology*, 40(10):1709–1729, 1995.

[82] M. Prudhomme, J. Tang, S. Rouy, G. Delacretaz, R.P. Salathe, and G. Godlewski. Diode laser and interstitial hyperthermia against ht29 colonic cancer. Effect of power settings on necrosis size. In *Laser-Tissue Interaction II*, volume 1646, pages 283–286. SPIE, Vol. 2327 1994.

[83] T. Purdie, M. Iizuka, M. Sherar, A. Fenster, and T.Y. Lee. The application of dynamic contrast enhanced computed tomography to interstitial laser photocoagulation. Technical report, CCPM - COMP/OCMP, London, Ontario, 1998.

[84] S. Rastegar, B.M. Kim, and S.L. Jacques. Role of temperature dependence of optical properties in laser irradiation of biological tissue. In *Laser-Tissue Interaction III Vol.1646*, pages 228–231. SPIE, 1992.

[85] T.S. Ravikumar. Interstitial therapies for liver tumors (review). *Surgical Oncology Clinics of North America*, 5(2):365–377, 1996.

[86] P. Reimer, C. Bremer, C. Horch, C. Morgenroth, T. Allkemper, and G. Schuierer. Mr-monitored LITT as a palliative concept in patients with high grade gliomas: preliminary clinical experience. *Journal of Magnetic Resonance Imaging*, 8(1):240–244, 1998.

[87] H.S. Reinhold and B. Endrich. Tumour microcirculation as a target for hyperthermia. *International Journal of Hyperthermia*, 2(2):111–137, 1986.

[88] A. Roggan, K. Dörschel, O. Minet, D. Wolff, and G. Müller. The optical properties of biological tissue in the near infrared wavelength range - review and measurements. In G. Müller and A. Roggan, editors, *Laser-Induced Interstitial Thermotherapy*, chapter Part II: Optical and Thermal Properties of Biological Tissue, pages 10–44. SPIE Press, Bellingham, Washington, 1 edition, 1995.

[89] A. Roggan and G. Müller. 2D computer simulations for real-time irradiation planning of laser-induced interstitial thermotherapy (LITT). In *Medical Applications of Lasers II*, volume 2327, pages 242–252. SPIE, 1994.

[90] A. Roggan and G. Müller. Dosimetry and computer based irradiation planning for laser-induced interstitial thermotherapy (LITT). In G. Müller and A. Roggan, editors. *Laser-Induced Interstitial Thermotherapy*, pages 114–156, Bellingham, Washington, 1995. SPIE Press.

[91] D.D. Royston. R.S. Poston. and S.A. Prahl. Optical properties of scattering and absorbing materials used in the development of optical phantoms at 1064 nm. *Journal of Biomedical Optics*. 1(1):110–116, 1996.

[92] M. Salcman, E. Moriyama. H.J. Elsner, H. Rossman, R.A. Gettleman, G. Neuberth. and G. Corradino. Cerebral blood flow and the thermal properties of the brain: A preliminary analysis. *Journal of Neurosurgery*, 70:592–598, 1989.

[93] C.P. Schulze, T. Kahn, T. Harth, H.J. Schwurzmaier, and R. Schober. Correlation of neuropathologic findings and phase-based MRI temperature maps in experimental laser-induced interstitial thermotherapy. *Journal of Magnetic Resonance Imaging*, 8(1):115–120, 1998.

[94] A. Shitzer. *Heat transfer in medicine and biology: analysis and application*. Plenum Press, New York. 1985.

[95] Sigma. Technical sheets on naphthol green. Technical report, Sigma, 1998.

[96] R Splinter, L Littmann, J Tuntelder, CH Chuang, M Thompson, R Svenson, and GP Tatsis. Predicting CW Nd:YAG photocoagulation lesion size in myocardium from Monte Carlo light simulations. In *Advances in Biological Heat and Mass Transfer*, volume HTD-Vol.189/BED-Vol.18, pages 75–78. ASME, 1991.

[97] W.M. Star. Difussion theory of light transport. In A.J. Welch and M.J.C. van Gemert, editors. *Optical-Thermal Response of Laser Irradiated Tissue*. chapter 6. pages 131–205. Plenum Press. New York. N.Y., 1995.

[98] H.J. Staveren. C.J.M. Moes. J. van Marie. S.A. Prahl, and M.J.C. van Gemert. Light scattering in intralipid-10% in the wavelength range of 400-1100nm. *Applied Optics*. 30(31):4507–4514, 1991.

[99] C. Sturesson and S. Andersson-Engels. A mathematical model for predicting the temperature distribution in laser-induced hyperthermia. Experimental evaluation and applications. *Physics in Medicine and Biology*, 40:2037–2052, 1995.

[100] C. Sturesson and S. Andersson-Engels. Theoretical analysis of transurethral laser-induced thermo-therapy for treatment of benign prostatic hyperplasia. Evaluation of a water-cooled applicator. *Physics in Medicine and Biology*, 41:445–463, 1996.

[101] C. Sturesson and S. Andersson-Engels. Tissue temperature control using a water-cooled applicator: Implications for transurethral laser-induced thermotherapy of benign prostatic hyperplasia. *Medical Physics*, 24(3):461–470, 1997.

[102] A. Surowiec, P.N. Shrivastava, M. Astrahan, and Z. Petrovich. Utilization of a multilayer polyacrylamide phantom for evaluation of hyperthermia applicators. *International Journal of Hyperthermia*, 8(6):795–807, 1992.

[103] T. Suzuki, K. Kurokawa, H. Higashi, K.Suzuki, and H. Yamanaka. Transurethral balloon laser enhanced thermotherapy in the canine prostate. *Lasers in Surgery and Medicine*, 21:321–328, 1997.

[104] A.N. Takata, L. Zaneveld, and W. Richter. Laser-induced thermal damage in skin. Technical Report SAM-TR-77-38, USAF School Aerospace Med., 1977.

[105] S. Thomsen. Identification of lethal thermal injury at the time of photothermal treatment. In G. Müller and A. Roggan, editors, *Laser-Induced Interstitial Thermotherapy*, chapter Part IV: Clinical Results, pages 459–467. SPIE Press, Bellingham, Washington, 1 edition, 1995.

[106] S. Thomsen, Jacques S.L., and Flock S. Microscopic correlates of macroscopic optical property changes during thermal coagulation of myocardium. *SPIE Laser-Tissue Interaction*, 1202:2–10, 1990.

[107] K.M. Tobin and S.M. Waldow. Effects of interstitial heating on the rif-1 tumor using an Nd:YAG laser with multiple fibers. *Lasers in Surgery and Medicine*, 19(2):216–23, 1996.

[108] R.A. Tracz, D.R. Wyman, P.B. Little, R.A. Towner, W.A. Stewart, S.W. Schatz, P.W. Pennock, and B.C. Wilson. Magnetic resonance imaging of interstitial laser photocoagulation in brain. *Lasers in Surgery and Medicine*, 12:165–173, 1992.

[109] R. van Hillegersberg, M. de Witte, W. Kort, and O. Terpstra. Water-jet-cooled Nd:YAG laser coagulation of experimental liver metastases: Correlation between ultrasonography and histology. *Lasers in Surgery and Medicine*, 13:332–343, 1993.

[110] I.A. Vitkin, B.C. Wilson, and R.R. Anderson. Analysis of layered scattering materials by pulsed photothermal radiometry: Application to photon propagation in tissue. *Optical Society of America*, 34(16):2973–2982, 1995.

[111] T.J. Vogl, M.G. Mack, P. Muller, C. Philipp, M. Juergens, KD. Knobber, A. Roggan, P. Wust, V. Jahnke, and R. Felix. Mr-guided laser-induced thermotherapy in tumors of the head and neck region: initial clinical results. *Fortschritte auf dem Gebiete der Rontgenstrahlen und der Neuen Bildgebenden Verfahren*, 163(6):505–514, 1995.

[112] T.J. Vogl, M.G. Mack, R. Straub, A. Roggan, and R. Felix. Magnetic resonance imaging–guided abdominal interventional radiology: laser-induced thermotherapy of liver metastases. *Endoscopy*, 29(6):577–583, 1997.

[113] G. Wagnieres, S. Cheng, M. Zellweger, N. Utke, D. Braichotte, J. Ballinni, and H. vanden Bergh. An optical phantom with tissue-like properties in the visible for use in PDT and fluorescence spectroscopy. *Physics in Medicine and Biology*, 42:1415–1426, 1997.

[114] A.J. Welch. The thermal response of laser irradiated tissue. *IEEE Journal of Quantum Electronics*, QE-20(12):1471–1481, 1984.

[115] A.J. Welch and G. Polhamus. Measurement and prediction of thermal damage in the retina of the rhesus monkey. *IEEE Transactions on Biomedical Engineering*, BME-31:633–644, 1984.

[116] A.J. Welch and M.J.C. van Gemert, editors. *Optical-thermal Response of Laser-irradiated Tissue*. Plenum Press, New York, 1995.

[117] A.J. Welch, M.J.C. van Gemert, W.M. Star, and B.C. Wilson. Definitions and overview of tissue optics. In A.J. Welch and M.J.C. van Gemert, editors. *Optical-thermal Response of Laser-irradiated Tissue*, chapter 1, pages 15–46. Plenum Press, New York, N.Y., 1 edition, 1995.

[118] A. Westra and W.C. Dewey. Variation in sensitivity to heat shock during the cell-cycle of Chinese hamster cells *in vitro*. *International Journal of Radiation Biology*, 19:467–477, 1971.

[119] W.M. Whelan. Dynamic modeling of ILP in soft tissues. Master's thesis, McMaster University, Hamilton, Ontario, 1996.

[120] W.M. Whelan, D.R. Wyman, and B.C. Wilson. Investigations of large vessel cooling during interstitial laser heating. *Medical Physics*, 22(1):105–115, 1995.

[121] P. Whiting, J. Dowden, and P. Kapadia. Mathematical analysis of the results of experiments on rat livers by local laser hyperthermia. *Laser in Medical Science*, 4(1):55–64, 1989.

[122] L.R. Williams and R.W. Leggett. Reference values for resting blood flow to organs of man. *Clinical Physics and Physiological Measurements*, 10:187–217, 1989.

[123] B.C. Wilson. Measurement of tissue optical properties: Methods and theories. In A.J. Welch and M.J.C. van Gemert, editors, *Optical-thermal Response of Laser-irradiated Tissue*, chapter 8, pages 233–271. Plenum Press, New York, N.Y., 1 edition, 1995.

[124] B.C. Wilson, M.S. Patterson, and D.M. Burns. Effect of photosensitizer concentration in tissue on the penetration depth of photoactivating light. *Lasers in Medical Science*, 1:235–244, 1986.

[125] D.R. Wyman W.M. Whelan. Modelling lesion formation in liver during interstitial laser photocoagulation. Technical Report Session 5, CCPM - COMP/OCMP, 1997.

[126] D.R. Wyman. Selecting source locations in multifiber interstitial laser photocoagulation. *Lasers in Surgery and Medicine*, 13(6):656–63, 1993.

[127] D.R. Wyman, M.S. Patterson, and B.C. Wilson. Similarity relations for the interaction parameters in radiation transport and their applications. *Applied Optics*, 28:5243–5249, 1989.

[128] D.R Wyman, C.L. Swift, R.A. Siwek, and B.C. Wilson. A control method for a nonlinear multivariable system: application to interstitial laser hyperthermia. *IEEE Transactions on Biomedical Engineering*, 38(9):891–898, 1991.

[129] D.R. Wyman and W.M. Whelan. Basic optothermal diffusion theory for interstitial laser photocoagulation. *Medical Physics*, 21(11):1651–1656, 1994.

[130] D.R. Wyman, W.M. Whelan, and B.C. Wilson. Interstitial laser photocoagulation: Nd:YAG 1064 nm optical fiber source compared to point heat source. *Lasers in Surgery and Medicine*, 12:659–664, 1992.

[131] L.X. Xu, M.M. Chen, K.R. Holmes, and H. Arken. The theoretical evaluation of the Pennes, the Chenholmes and the Weinbaum-Jiji bioheat transfer models in the pig renal cortex. In *Advances in Biological Heat and Mass Transfer*, pages 15–21. ASME, 1991. HTD-Vol. 189/BED-Vol. 18.

[132] Y. Yang, A.J. Welch, and H.G. Rylander III. Rate process parameters of albumen. *Lasers in Surgery and Medicine*, 11:188–190, 1991.